Experimental studies on intermolecular, hydrodynamic and capillary interactions at the nanoscale

Memoria de tesis para optar al grado de
Doctor en Ciencias Físicas
presentada por

Mariana Köber

en el
Departamento de Física de la Materia Condensada
de la Facultad de Ciencias
de la Universidad Autónoma de Madrid,

dirigida por la Dra. Mónica Luna y el Prof. Fernando Briones
en el Instituto de Microelectrónica de Madrid.

INSTITUTO DE MICROELECTRÓNICA DE MADRID
(CENTRO NACIONAL DE MICROELECTRÓNICA)

Junio 2012

Resumen

Las interacciones intermoleculares, hidrodinámicas y capilares en la nanoescala están de actualidad debido a su importancia en las aplicaciones biológicas y biomédicas. Esta tesis, de carácter experimental, pero estrechamente vinculada a las interpretaciones teóricas de los fenómenos físicos que intervienen en estas interacciones, se ha desarrollado principalmente en torno a dos objetivos: estudiar el papel de las interacciones capilares y la histéresis de adhesión en la Microscopía de Fuerzas Atómicas operado en aire, y desarrollar una nueva técnica experimental capaz de detectar interacciones moleculares entre nanopartículas magnéticas funcionalizadas y biomoléculas en medios biológicos.

Uno de los resultados más relevantes de esta tesis es que la adhesión capilar entre dos superficies hidrófilas depende fuertemente de la geometría en la nanoescala. Particularmente sorprendente fue el descubrimiento de que la adhesión capilar incluso puede disminuir con la humedad. Se han realizado trabajos para estudiar el efecto de la histéresis de adhesión en el modo dinámico de la Micsroscopía de Fuerzas Atómicas, con el fin de investigar la relación entre la potencia disipada obtenida experimentalmente y propiedades fisicoquímicas de la muestra.

Por otro lado, en vista de una futura aplicación en el campo de biosensores de reconocimiento molecular basados en nanopartículas, se ha implementado un montaje experimental para detectar la birrefringencia magnética transitoria en una suspensión de nanopartículas magnéticas mediante la aplicación de un campo magnético pulsado. Esta técnica magneto-óptica permite utilizar nanopartículas como sondas para detectar

el reconocimiento molecular *in situ* en tejidos o células. Se demuestra que los diámetros hidrodinámicos de pequeños agregados anisótropos se pueden determinar *in situ* en geles de agarosa – un sistema modelo compatible con la separación por electroforesis. Además, la técnica se ha aplicado para detectar el reconocimiento molecular de Concanavalina A por nanopartículas superparamagnéticas funcionalizadas con glucosa.

Abstract

Intermolecular, hydrodynamic and capillary interactions at the nanoscale are current hot topics because of their importance in biological and biomedical applications. This thesis, mainly experimental in nature but closely linked to theoretical interpretations of physical phenomena involved in those interactions, has been developed primarily around two objectives: study the role of capillary interactions and adhesion hysteresis in ambient Atomic Force Microscopy (operated in air), and develop a new experimental technique capable of detecting intermolecular interactions between functionalized magnetic nanoparticles and biomolecules in biological media.

One of the most relevant results of this thesis is that capillary adhesion between two hydrophilic surfaces depends strongly on the geometry at the nanoscale. Particularly surprising was the finding that capillary adhesion may even decrease with humidity. Works have been performed to study the effect of adhesion hysteresis in dynamic Atomic Force Microscopy, in order to investigate the relation of the experimentally obtained dissipated power and physicochemical sample properties.

On the other hand, in view of a future application in the field of nanoparticle based molecular recognition biosensors, we have implemented an experimental setup to detect Transient Magnetic Birefringence in a suspension of magnetic nanoparticles by applying a pulsed magnetic field. This magneto-optical technique allows the use of nanoparticles as *in situ* probes to detect molecular recognition in tissues or cells. It is shown that hydrodynamic diameters of small anisotropic particle aggregates can

be determined *in situ* in agarose gels – a model system compatible with the separation by electrophoresis. Furthermore, the technique has been applied to detect the molecular recognition of Concanavalin A by glucose functionalized superparamagnetic nanoparticles.

Declaration

This dissertation is the result of my own work, except where explicit reference is made to the work of others, and has not been submitted for another qualification to this or any other university.

Mariana Köber

Acknowledgements

The completion of this work has been made possible thanks to the support of many, and at this point I want to express my appreciation.

My supervisors, Mónica Luna and Fernando Briones, have given me substantial support in the realization of this undertaking. Mónica introduced me into the world of AFM and helped me develop skills for the variety of tasks scientific work involves. She was there for me in everyday problems and advised me on explaining and condensing results. Fernando always astounded me with his broadly diversified and profound knowledge, but also with his practical skills and the ease he would come up with a solution in the instrumental setup within just a few hours. With both I also shared many interesting discussions on life beyond science, and their way of getting to work created a very enjoyable atmosphere. ¡Gracias!

I want to extend my thanks to my tutor at the Universidad Autónoma de Madrid, Julio Gómez, for his support during my graduate studies, as well as for the interesting discussions about AFM.

Thanks also go to Juan José Sáenz for sharing his profound knowledge in physics in his fun and unconventional way. His capacity to capture the important points for transmitting the central idea is just admirable. Thanks, too, to Enrique Sahagún for giving ideas and explications to the experimental findings, and for performing simulations to explain the experimental results. Their previous investigations to elucidate the role dissipation plays in AFM inspired part of this work, and their point of view, as theoreticians, enriched the work significantly. I really enjoyed our gatherings!

The collaboration with the group of Jesús de la Fuente was particularly close during the elaboration of this thesis. I am greatly indebted to Jesús, María Moros and Valeria Grazú for sharing their invaluable knowledge on chemistry in general, and nanoparticle synthesis, characterization and applications in particular. This work would not have been possilbe without their contribution by synthesizing state-of-the-art nanoparticles, discussing results and giving ideas for further work. They always lend me an ear, and our gatherings were lots of fun. It was great working with you!

I am very grateful to Soledad Penadés who participated in the development of the biosensor and supplied us with state-of-the-art core-shell nanoparticles functionalized with DNA. Although we finally couldn't match transducer and nanoparticles, we learnt a lot from the collaboration with Soledad, Isabel García and Juan Gallo. Thanks, too, for having us at CIC biomaGUNE – it was an impressive experience to dip into the world of *in vivo* biomedical applications!

I am also indebted to Miquel Salmerón who accepted me as visitor in his group, giving me the opportunity to work at the Molecular Foundry and the synchrotron of the Berekeley labs, which was an invaluable experience. In particular I am grateful to Ferenc Borondics, Peng Jiang and Soeren Porsgaard for integrating me into their investigations and for introducing me into the work at the beamline. It was fun working with you! I also remember discussions with Paul Ashby about dissipation in AFM. Thanks also go to all lab members and visitors, and in particular to Sabine, Bas, Ingeborg, Ute and Julien with whom I really enjoyed lunch time and some shared evening. Not to forget the people I met out of the lab: Alejandra, Gigi, Nicole... Thanks for sharing this great time with me, I won't forget it!

Thanks go to Laura Franco Fraguas who hosted my stay in Montevideo and showed me how to purify the *Erythrina cristagalli* lectin by affinity chromatography. It was a neat experience, and Laura did a great job in instructing me in her biochemistry lab. I am also grateful to Silvana and Majo for their help, as well as to all the other lab members (Gabi, Paula,...) for integrating me right away.

I really enjoyed the collaboration with Arisbel Cerpa, Paloma Ballesteros and Sebastián Cerdán on using carbon nanotubes as anisotropic probes for MRI. It was a very interesting project to work on.

I furthermore thank Puerto Morales and Angeles Villanueva for fruitful discussions on magnetic nanoparticles and their use in *in-vivo* biomedical applications. Maybe we still get to test our method in cells...

Thanks also go to Suzi Jarvis and Tim Brosnan for their collaboration in the experiments we performed to determine tip-sample contacts in dynamic AFM. Furthermore, I thank the Nanotec crew, in particular Luis Colchero, who always found some time to advise us on all kinds of issues that came up during AFM operation.

Of course, thanks go to all the people who made everyday life at the IMM fun. Han pasado ya más de cinco años y hemos compartido algunos momentos para recordar – comidas, cenas, fiestas... Es imposible nombrar a todos aquí, y menos ser justo en el orden. Especialmente recuerdo los ratos con Sonia, Martina y Cristina, Marcos, Javi Martínez, Patricia, Merce, Horacio, Christian, Javi Martín, Chon, Ivan PG, Ivan Fernández, Jorge, Raquel Alvaro, Elena, ZP, Juan Bautista, Begoña, Jaime, Riu, Olga, Pablo, Diego, Luis Enrique, Rui, Fran, Diana, Priscila, Elías, Marco, Miguel, Carmen, ... Gracias también a administración, especialmente a Mercedes y Manuel, por resolver todos los asuntos burocráticos con

agilidad. También me acuerdo de los buenos ratos que pasé con la gente que conocí en la UAM: David Martínez, Ana, Jose, Elvi...

My most profound thanks go to my family and friends who have been a great support through all stages. Speziell meinen Eltern, Edelgard und Lothar, danke ich dafür, dass sie mich in all meinen Lebensphasen begleitet, unterstützt und ermutigt haben. Danke für Euer Vertrauen und das Verständnis für meine Entscheidungen. Ihr habt mir alle Türen geöffnet. Auch meinen Freunden aus Deutschland möchte ich danken. Es ist einfach super zu wissen, dass ihr da seid, auch wenn wir uns nicht oft sehen können: Katrin & Robbie, Judith & Guillaume, Bianca & Wolfgang, Britta & Ansgar, Jenny & Mario, Jenny Fischer und Bianca... Gracias también a mis amigos en España por los buenos momentos que me han hecho pasar: Beu & Susana, Laura & Eduardo, Mari & Alicia, Bartolo, María, Marisa, Eugenio & María, Dani, Juan Carlos & Ana, Iván, Sonia & Roberto, Martina & Carlos... Por supuesto, no me olvido de mi segunda familia, en particular de Paca & Antonio, que me ha acogido con tanto cariño. ¡Muchas gracias!

Finalmente, Abraham... Gracias por estar siempre a mi lado. Por escucharme, por darme tu opinión que tanto valoro y por animarme en los momentos difíciles. A tu lado paso los momentos más felices, cuando nos contamos tonerías y no tan tonterías. Gracias por hacer la vida tan fácil y tan rica. ¡Eres genial!

Contents

Chapter 1

Motivation

"Curiosity is always the first step when solving a problem."
— Galileo Galilei, 1564–1642

The investigations performed in the course of this thesis belong to the field of nanotechnology, and in part to the field of nanobiotechnology, where nanotechnology is used to create devices to study biological systems. Capillary, hydrodynamic and intermolecular interactions at the nanoscale have been studied, whereby two different instrumental techniques have been employed: Atomic Force Microscopy (AFM) and Transient Magnetic Birefringence (TMB). For clarity, this manuscript is divided into two parts:

In the investigations presented in Part I, a commercial Atomic Force Microscope (Nanotec Electronica, Cervantes FullMode AFM System, http://www.nanotec.es/) has been used to study adhesive interactions occurring in AFM under operation in air. Capillary adhesion between bodies of nanometric dimensions is investigated in detail. Furthermore, adhesion hysteresis in dynamic AFM operation is studied, and its effect on

the dissipation channel, which is expected to offer additional information on physicochemical sample properties, is discussed.

Part II is focused on the implementation and application of a barely explored technique called Transient Magnetic Birefringence. The technique, applied to magnetic nanoparticles (MNPs) suspended in physiological media, has been studied as to its usefulness to detect intermolecular interactions in biological media.

In the following, the motivation and specific objectives of this work are presented.

1.1 Adhesion hysteresis and capillary interactions in dynamic AFM in air

Today, Atomic Force Microscopy (AFM) is being widely used in research and industry of diverse fields. In AFM, a sharp tip of nanometric apex (*nanoprobe*) is brought close to the sample surface (as illustrated in Figure 1.1), and interaction forces between tip and sample are controlled and/or monitored. We could say that the nanoprobe "senses" the sample surface.

Most commonly, AFM is used to obtain information about the surface topography at the nanometric scale. However, Atomic Force Microscopy can do much more than just obtaining topography maps: further material properties can be obtained simultaneously, molecular recognition sites can be determined and binding forces quantified, but also applications not related to material characterization have been developed, like nanolithography through local oxidation[1] and dip pen lithography.[2]

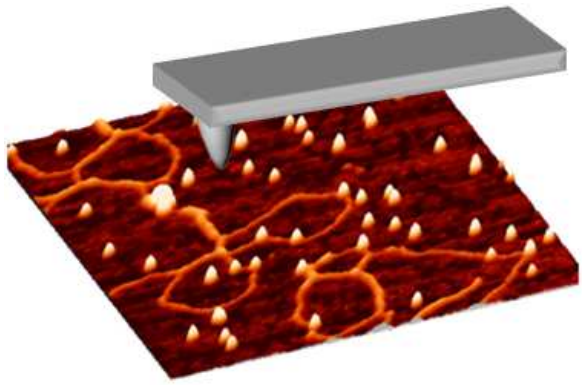

Figure 1.1 Principle of Atomic Force Microscopy (AFM) operation. A nanoprobe (a sharp tip of nanometric apex) "senses" the sample surface. Shown is a sample of cleaved mica onto which DNA and colloidal Au nanoparticles have been deposited. The sample has been prepared by the group of Prof. S. Penadés (CIC biomaGUNE, Spain).

For material characterization, the AFM presents two main advantages over other microscopy techniques like electron microscopy, making it ideal for studying biological specimen: first, it detects the interaction forces between any two materials, irrespective of the materials' electronic structure. Thus, in particular insulators can be imaged, in contrast to other microscope techniques which are "blind" to insulating materials. Secondly, the AFM can be operated not only in vacuum, but also in air and liquids, which is of particular interest when biological specimen like proteins, deoxyribonucleic acid (DNA) and cells are to be probed. For example, the interaction of nanoparticles with DNA can be examined operating an Atomic Force Microscope in air (Figure 1.2).[3]

In the most simple AFM operation mode, the sample topography is obtained by dragging the tip over the sample surface. However, especially biological and soft samples such as delicate biomolecules, polymers and cells require a less invasive operation mode which hardly perturbs the

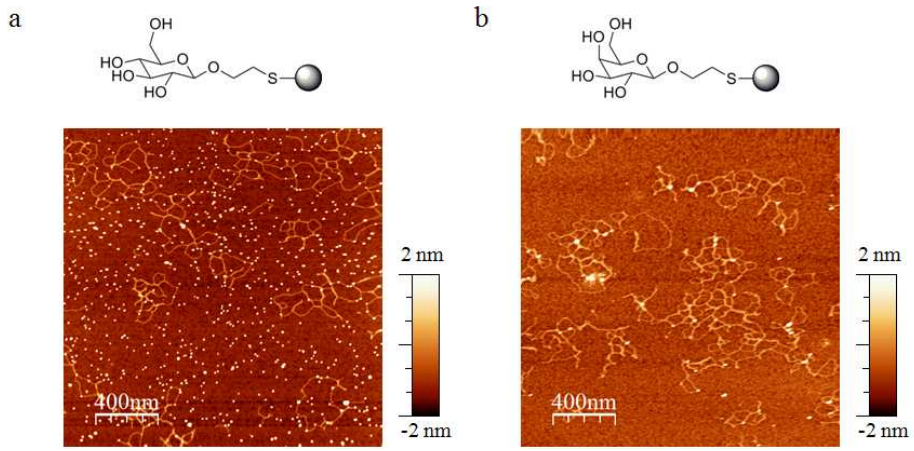

Figure 1.2 Interaction of nanoparticles with DNA, probed with the Atomic Force Microscope in air. Colloidal Au nanoparticles functionalized with different carbohydrates were mixed with DNA, and the mixture was deposited on cleaved mica. The topography images show that the interaction of nanoparticles and DNA depends on the particle functionalization: (a) Au nanoparticles functionalized with β-glucose hardly interact with the DNA (nanoparticles are evenly distributed on the mica surface). (b) On the contrary, nanoparticles functionalized with β-galactose strongly interact with the DNA (practically all nanoparticles are attached to the DNA). The samples have been prepared by the group of Prof. S. Penadés (CIC biomaGUNE, Spain).

sample. In dynamic AFM, the cantilever is brought to oscillate close to the sample surface, and the sample surface can be imaged while the tip hardly perturbs the sample. Lateral forces on the sample are almost eliminated and normal forces minimized, so that dynamic AFM is adequate to image biological and soft samples.

During dynamic AFM operation, the tip apex comes very close to the surface and may even be in intermittent contact. Once in contact, commonly a connective neck forms, for example a liquid neck[4–6] (Figure 1.3) or an atomic scale connective neck due to rearrangements of the atoms at the contact point[7]. As a consequence, the tip adheres to the

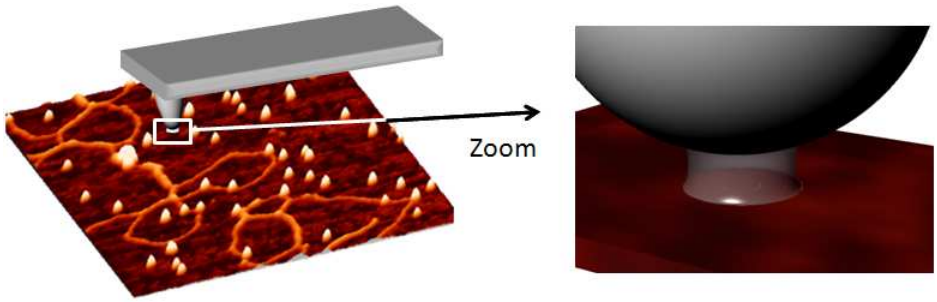

Figure 1.3 Under operation in air, a liquid meniscus forms between tip and sample when they come close (unless tip and sample are hydrophobic). Today's understanding of how adhesion depends on humidity at the nanoscale is still incomplete, due to the large number of parameters involved in the process (nanoasperity shape, contact radius, contact angles, relative humidity, etc.).

sample surface. Upon tip retraction, the neck elongates, until it eventually breaks. The difference between the work needed to separate both surfaces and that originally gained on bringing them together is called adhesion hysteresis. The adhesion hysteresis associated to these contacts involves energy dissipation.

In dynamic AFM, the energy that is dissipated in each tip-sample interaction cycle is not obtained directly, but rather the dissipated power, which presents a time-average over several oscillation cycles. However, it is still not fully understood how the dissipated power relates to physicochemical sample properties. For example, when scanning an epithelial cell at ambient humidity, topography and dissipated power can be obtained simultaneously (Figure 1.4). Interestingly, high and low dissipative areas are not correlated to prominent topographic features. The dissipation channel rather presents a complementary channel, offering further information on sample properties. But which information on material properties can we get from the dissipated power? How does

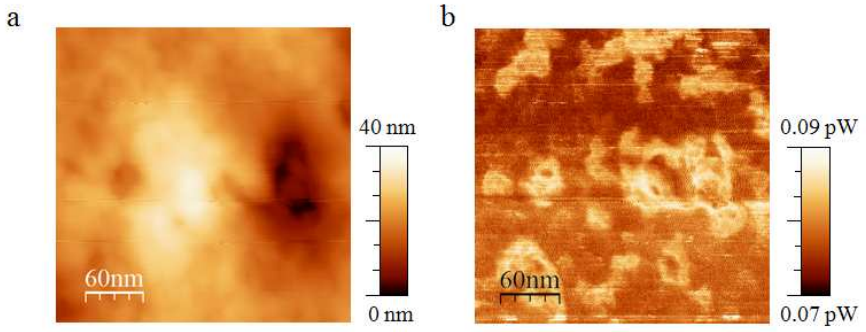

Figure 1.4 Detail of an epithelial cell measured at ambient humidity. Shown are topography (a) and dissipated power (b). High and low dissipative areas are not correlated to prominent topographic features. How does the dissipated power relate to material properties?

this qualitative information in the dissipation channel (material contrast) relate to some quantitative information (e.g. hydrophilicity)?

Hysteresis and viscoelasticity have been shown to yield the dominant contributions to the experimentally obtained dissipation.[8] However, the knowledge on the dissipative processes that take place during AFM operation is still incomplete. For example, hysteresis can be due to the formation and rupture of nanometer sized liquid necks, and in this case, numerical simulations performed by the group of Prof. J. J. Sáenz (Universidad Autónoma de Madrid) have shown that dissipation maps can be related to sample hydrophilicity.[6] The results suggest, however, that a simple relation is only valid in one of the two operating regimes. Motivated by these interesting results, our objective was to study the effect of adhesion hysteresis (as a generalization of liquid neck formation) in dynamic AFM experimentally, and analyze how the experimentally obtained dissipated power has to be interpreted.

Experimental investigations on the effects of capillary adhesion in dynamic AFM operated in air are not trivial, since many parameters are involved in the adhesion process, to which the complexity of the cantilever dynamics is added. To approach this problem, we studied the capillary adhesion between nanometric hydrophilic bodies that are not oscillating, to avoid the additional difficulty the cantilever dynamics introduces in the interpretation of the results. Although an extensive study of the capillary forces acting at micro- and nanoasperity contacts has been performed over the last years,[6,9–22] today's understanding of how adhesion depends on humidity at the nanoscale is still incomplete, due to the large number of parameters involved in the process, such as the nanoasperity shape, the contact radius, contact angles, relative humidity, etc. Our objective was to elucidate how capillary adhesion of nanometric hydrophilic bodies depends on relative humidity. In particular, attention was paid to the role size and shape of the nanometric objects play. Experimental studies were complemented with simulations performed by the group of Prof. J. J. Sáenz (Universidad Autónoma de Madrid).

1.2 Interactions of nanoparticles in physiological media

Colloidal nanoparticles (NPs) are promising tools in a variety of biomedical applications, for example as probes for disease prognosis, as contrast agents for *in vivo* diagnosis and as drug carriers for therapy. Magnetic nanoparticles (MNPs), in particular, can be manipulated by a magnetic field, which allows to use them for magnetic resonance imaging (MRI) contrast enhancement, drug targeting, hyperthermia, and as sensor probes in a biosensor (Figure 1.5).[23,24] Consequently, MNPs can potentially be used in several *in vivo* and *in vitro* applications.

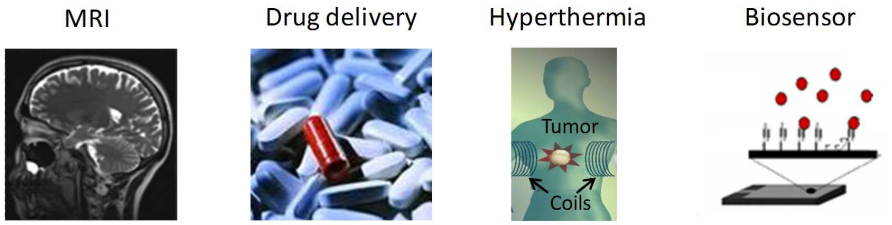

Figure 1.5 Biomedical applications of magnetic nanoparticles include magnetic resonance imaging (MRI) contrast enhancement, drug delivery, hyperthermia, and biosensors. In consequence, magnetic nanoparticles are to be used *in vivo* and *in vitro*.

A biosensor is a device for the detection of an *analyte* (a biomolecule that is to be detected, e.g. DNA or proteins for diagnosing and prognosing diseases). It consists of a biological recognition system (*bioreceptor*) and a *transducer* which converts a particular effect that the interaction of the analyte with the bioreceptor produces into a measurable signal. A variety of biosensing mechanisms have been developed in the last years and decades.[25] Nanotechnology has given new impulses,[26] due to the utilization of nanometer sized structures and nanoparticles.

The original proposal for this thesis was to use suspended monodisperse MNPs - functionalized adequately to recognize the analyte - as bioreceptor, and to study a transduction mechanism that combines a magnetic particle manipulation with an optical detection of the resulting NP movement. Detection schemes that are intrinsically selective to particle clusters with respect to single particles have been shown to be very sensitive.[27] Here, the idea was to provoke the formation of NP dimers (clusters of two particles) through molecular recognition, and use magnetically induced birefringence as signature for the presence of these dimers. The detection scheme is illustrated in Figure 1.6. A specific and controlled particle dimerization in the presence of the analyte is achieved

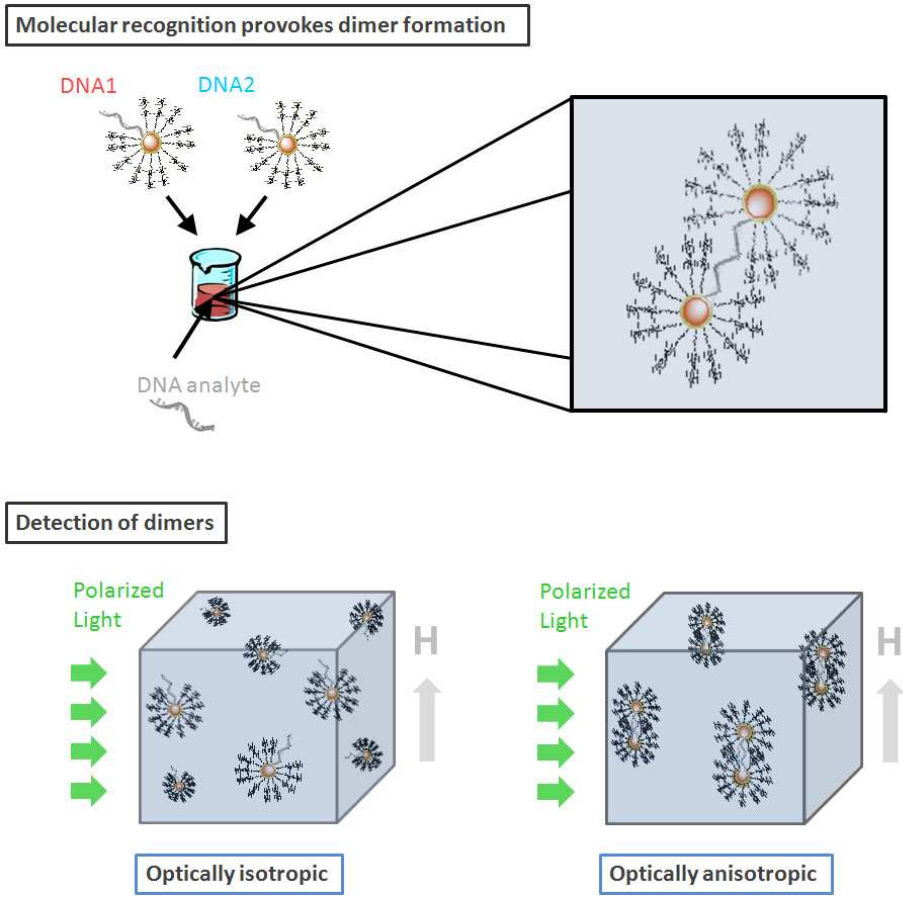

Figure 1.6 Scheme for detecting molecular recognition: Functionalized spherical magnetic nanoparticles serve as probes. Particles are functionalized in a way that molecular recognition leads to dimer formation, e.g. using two sets of nanoparticles, with particles of each set having a DNA strand attached which is complementary to the DNA that is to be detected (*analyte*). If the complementary DNA is added, DNA strands will hybridize, which leads to the formation of particle dimers. The application of a magnetic field will align the particle dimers with the field (if the magnetic dipolar interaction is strong enough), and the suspension becomes optically anisotropic. If no dimers are present the suspension will remain isotropic even with the applied magnetic field. Optical anisotropy is then a signature of molecular recognition.

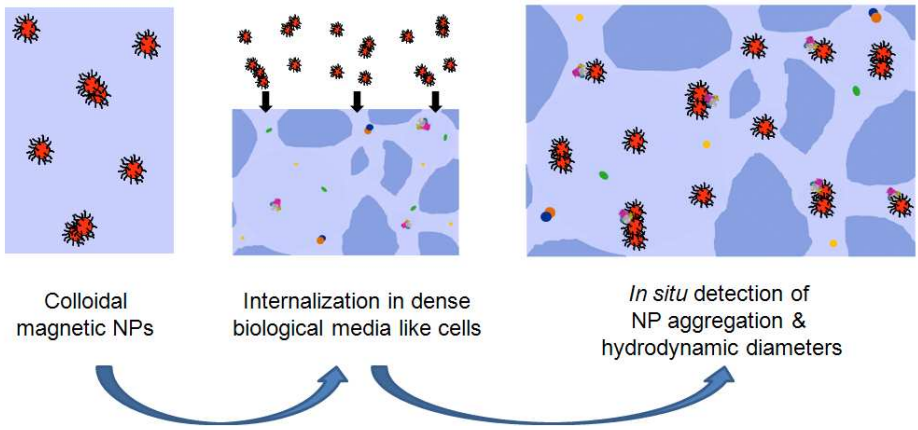

Figure 1.7 Schematic illustrating the principle of applying TMB *in situ*

by adequately functionalizing the NPs (NP synthesis and functionalization were performed by collaborating groups). The application of a magnetic field will align particle dimers with the magnetic field, and the net orientation of the particle dimers in space will render the solution optically anisotropic (and, thus, birefringent). On the other hand, if no molecular recognition takes place, NPs remain monomers, and the solution containing only monomeric MNPs will remain optically isotropic when the magnetic field is applied. Consequently, magnetically induced birefringence is a signature of molecular recognition.

With this proposed detection technique, the NPs are probes that can be sent out to the sites of interest, for example cells and tissue, where the rapid and non-invasive detection can be realized *in situ* (Figure 1.7), in contrast to other biosensors where larger particles are used (for example magnetic beads) or NPs are fixed to a surface, so that an *in situ* detection in cells or tissue is not possible. The applicability of this technique to the *in situ* detection would allow to study NP-matrix interactions that play an important role when NPs are used in *in vivo* applications.

Contrary to our initial assumptions, in the course of this thesis we have found that NP suspensions - although synthesized according to state of the art standards - were not completely monomeric, but rather presented a small fraction of small aggregates (primarily dimers and trimers). In consequence, birefringence was present in all NP suspensions, even in the absence of molecular recognition.

On the other hand, for those particles that contribute to the birefringence signal, the hydrodynamic diameters can be determined. The hydrodynamic particle diameter, in turn, is also an indicator of particle aggregation and the adsorption or binding of biomolecules, since it comprises the whole particle cluster moving through the solvent, including the inorganic core(s), the surfactant molecules, any attached biomolecules and the solvent layer attached to the particle (cluster) when it moves in the solvent. Therefore, molecular recognition can be detected through a hydrodynamic diameter increase.

When short magnetic field pulses are applied, the particle orientation changes alternately between an alignment in the magnetic field direction and an arbitrary orientation due to Brownian motion. Consequently, when particles are optically anisotropic, a magnetically induced birefringence appears and decays, which gives the technique the name Transient Magnetic Birefringence (TMB). From the birefringence decay that occurs when the magnetic field falls to zero, the hydrodynamic diameter can be determined.[28–30] Although first TMB studies on MNPs were already conducted in the 1970's,[28–31] only few research groups have studied the technique since, despite the growing interest MNPs and their applications have experienced in the last years (Figure 1.8).

The objective of this thesis was to implement an experimental setup to detect molecular recognition by means of the birefringence that is induced magnetically in a suspension of adequately functionalized MNPs.

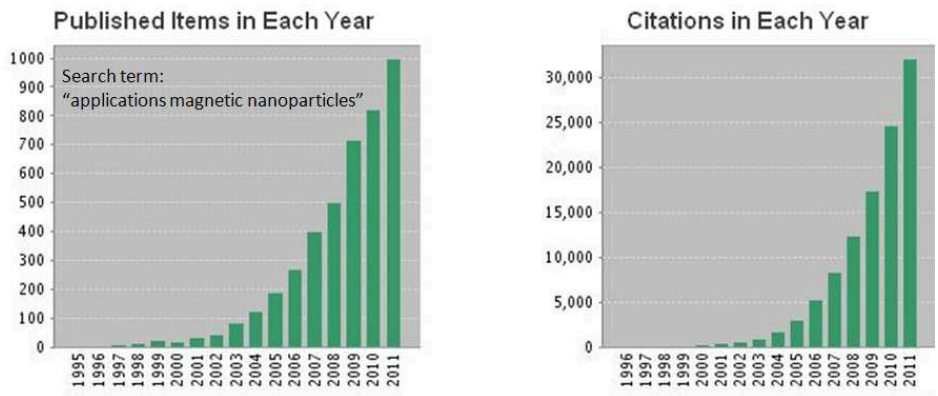

Figure 1.8 Citation report of articles published on the topic "applications of magnetic nanoparticles" and the citations they received, according to the Web of Knowledge.

As exposed above, TMB resulted to be the most adequate measurement setup.

In experimental TMB studies, even very recent ones, the authors have claimed that birefringence is due to monomers of spherical magnetite and maghemite NPs.[32–35] However, hydrodynamic diameters determined with TMB have always been greater than twice the magnetic core diameter.[30,32–35] Theoretical studies suggested that birefringence in these suspensions is due to small elongated aggregates.[36,37] A central concern of this work is to prove experimentally that birefringence is actually not caused by monomers of spherical magnetite NPs, but rather by dimers and small anisotropic aggregates.

So far, TMB has never been applied to NPs included in dense, highly light scattering media, but only to NP suspensions. However, biofunctionalized MNPs are to be used in biomedical applications and ought to be characterized and possibly monitored in their biological environment. In cell-incubating conditions, for example, nanoparticles

may aggregate and serum proteins adsorb on the particles, altering the nanoparticles' performance and their interaction with cell membranes.[38] Thus, characterization tools must be at hand that allow for determining the interactions of the nanoparticles with the biological medium like living cells and tissue *in situ*. In this thesis, the applicability of TMB to dense and highly light scattering media has been explored. To this end, proof of concept measurements were performed on NPs included in a porous agarose gel – a model system that scatters light in a similar way as a more complex biological medium but in which NP-matrix interactions are weak, and which allowed a combination with a particle seperation by electrophoresis.

In the last decade, first proof of principle studies have been performed that demonstrate that TMB can be used to monitor molecular recognition.[32–35] However, some basic investigations of the technique are still lacking. For example, it has been shown that the binding dynamics can be determined by means of TMB;[34] but it has not been studied whether or how the continuous measurement during incubation affects the binding. In this thesis, continuative studies are to be performed to explore the potential of TMB by means of a model carbohydrate-lectin interaction, using glucose functionalized NPs (synthesized by the group of J. M. de la Fuente, Instituto de Nanociencia de Aragón) and the lectin Concanavalin A (ConA) (purified in the group of Laura Franco-Fraguas, Universidad de la República de Uruguay).

1.3 Structure of this thesis manuscript

For clarity, this manuscript has been divided into two parts: the first part deals with the studies on capillary interactions and adhesion hysteresis of AFM nanoprobes in air, and the second part with the interaction of nanoparticles with their biological medium studied by TMB.

In the first chapter of Part I (Chapter 2), the interaction forces and aspects of AFM operation that are most relevant for this work are discussed. In Chapter 3, our studies on capillary adhesion at the nanoscale are presented. The effect of adhesion hysteresis in dynamic AFM is discussed in Chapter 4.

Part II starts with an introduction to colloidal NPs and the underlying physics of TMB to understand and optimize instrument design (Chapter 5). Subsequently, the implementation of the experimental setup is presented (Chapter 6). In Chapter 7, the application of TMB to dense media is demonstrated, and the contribution of particle monomers to the birefringence signal is analyzed. In Chapter 8, the application of TMB to study molecular recognition is demonstrated on the basis of a model lectin-carbohydrate recognition, namely the recognition of Concanavalin A (ConA) by glucose functionalized NPs.

Finally, summary conclusions and perspectives are presented.

Part I

Adhesive interactions at the nanoscale probed by Atomic Force Microscopy in air

Chapter 2

Interaction Forces at the Nanoscale and Atomic Force Microscopy

"The universe is full of magical things
patiently waiting for our wits to grow sharper."
— Eden Phillpotts, 1862–1960

Atomic Force Microscopy (AFM) plays a central role in this thesis: AFM spectroscopy experiments have been performed to study capillary adhesion (Chapter 3) and adhesion hysteresis (Chapter 4), and the imaging mode of AFM has been used to characterize NPs and their aggregates (Chapter 7). In this chapter, the interaction forces and aspects of AFM operation that are relevant in this thesis are presented.

2.1 Interaction forces at the nanoscale

At the nanoscale, electromagnetic forces, relatively strong and of infinite range, govern the interaction forces. The other three of the four distinct forces that govern nature in today's understanding - the gravitational, weak, and strong forces (in ascendent order of strength), each governed by their proper interaction bosons - are either too weak or too short-ranged to play an important role at the nanoscale: The gravitational force only becomes significant for heavier objects since it is very weak, and strong and weak nuclear forces only act in extremely short ranges (10^{-6} and 10^{-8} nm, respectively, since they decay extremely fast with distance). Intra- and intermolecular forces such as van der Waals forces, ionic, covalent and π-bonding and hydrogen bonds are all electromagnetic forces. In this way electromagnetic forces determine the properties of liquids, solids and gases, as well as the behaviour of particles in solution or the organization of biological structures.[10]

In the context of AFM experiments, where distances are typically in the nanometer range, forces are generally considered to be long-range when their range is > 1 nm, and short-range when their range is < 1 nm. In AFM attractive and repulsive forces arise, which has been shown to affect the dynamics of the system (see Section 2.3, page 38). Attractive long-range van der Waals forces[10,39,40] and repulsive short-range forces due to overlapping electron orbitals form the basic interaction forces in ambient AFM (operated in air). Other forces can appear, such as long-range electrostatic[41–43] and magnetic forces[44–46], or short-range chemical[47,48] and adhesion forces[6,8,47]. Moreover, the interaction can be dissipative. Table 2.1 lists the interaction forces that are most commonly encountered in AFM. Naturally, depending on the particular application, other forces

Interaction force	Range	Conditions
Electrostatic	up to 100 nm	charged materials
Magnetic	up to 100 nm	magnetic materials
Capillary	few nm	hydrophilic materials
van der Waals	few nm	always
Chemical	fraction of nm	material dependent
Contact	fraction of nm	always

Table 2.1 Interaction forces commonly encountered in Atomic Force Microscopy

may appear. In the following, the interaction forces that play a prominent role in the AFM experiments performed in this thesis are introduced.

van der Waals forces

van der Waals (vdW) forces arise between macroscopic objects mainly due to the dispersion interaction of the atoms (present in the two interacting bodies) across the interjacent medium. For a sphere of radius R interacting with a flat surface (which is the standard geometry assumed in force microscopy), the van der Waals force F_{vdW} scales with the inverse square of the objects' distance z, and is proportional to the Hamaker constant A,[10]

$$F_{\mathrm{vdW}} = -\frac{AR}{6z^2}. \tag{2.1}$$

The Hamaker constant depends on the number of atoms per unit volume and has values of ~ 1 eV for solids (10^{-19}–10^{-20} J). The most

relevant case for this thesis is that of mica ($KAl_2(AlSi_3O_{10})(F,OH)_2$) interacting across vacuum against SiO_2, for which the Hamaker constant is $9.35 * 10^{-20}$ J.[39] Then, for a sphere of 10 nm radius the van der Waals force at a distance of 1 nm is in the order of -0.16 nN. For a cone or pyramid interacting with a flat surface (another important geometry in force microscopy) the van der Waals forces depend logarithmically on distance, $F_{\mathrm{vdW}} \propto \ln(z)$.[49]

van der Waals forces are always present and play a predominant role in ambient AFM (operated in air), where they are effective up to few nanometers. Since van der Waals forces depend on the material properties and geometry of the interacting bodies and on the intervening medium,[50,51] the magnitude (and even the sign) of vdW forces can be controlled by choosing an adequate configuration. In air, vdW forces are always attractive. When the objects are submerged in water, van der Waals forces can be reduced significantly [52] since vdW forces exerted by the water molecules cancel out the vdW forces between the two objects.

van der Waals forces play a fundamental role in adhesion, surface tension, physisorption, wetting and properties of gases and liquids, among others.

Contact forces

When two bodies are approached to a few ångström, a short-range repulsive force will appear due to the overlap of the electronic orbitals of the bodies' atoms. We then say that the bodies are in contact. This repulsive force is always present when two bodies are in contact and is of very short range as only the most proximate atoms are involved. The distance at which the maximum interpenetration of the atoms is reached (then the two bodies are said to be in contact) is called the intermolecular

distance a_0, and can be approximated by 0.165 nm, according to [10]. When $z < a_0$ (and, eventually, adopts negative values), indentation occurs.

Several models have been developed to describe the contact interaction: The Hertz model[53], which already dates back to 1881, considers only the elastic deformation of an elastic sphere and a rigid substrate; no attractive forces are included. In the Hertz model the contact area is related to the sphere radius, the load and the elastic modulus. After unloading, the sphere detaches from the substrate without adhesion and the elastic deformation recovers completely. The Hertz model has been further developed to more realistic models which include some attractive interaction.[54] The most known of these models are the Johnson-Kendall-Roberts (JKR) model[55] which accounts for adhesion through a surface energy term, and the Derjaguin-Muller-Toporov (DMT) model[56] that contains an attractive long-range force. Highly adhesive systems (soft materials and large contact area) are well described with the JKR model, while systems with low adhesion (hard materials with a Young's modulus of 1–100 GPa, small contact area) are well described with the DMT model.

The DMT force can be written as[57]

$$F_{\mathrm{DMT}} = \frac{4}{3} E^* \sqrt{R} (a_0 - z)^{\frac{3}{2}} \qquad \text{for } z \leq a_0, \tag{2.2}$$

where E^* is the effective Young's modulus defined by $E^{*-1} = (1 - \nu_1^2) E_1^{-1} + (1 - \nu_2^2) E_2^{-1}$, E_1 and E_2 being the Young's modulus and ν_1 and ν_2 the Poisson's ratio of the two interacting bodies.

In contact, the van der Waals force between a sphere of radius R and a flat body can be approached by $F_{\mathrm{vdW}} = -AR/6a_0^2$. Taking into account

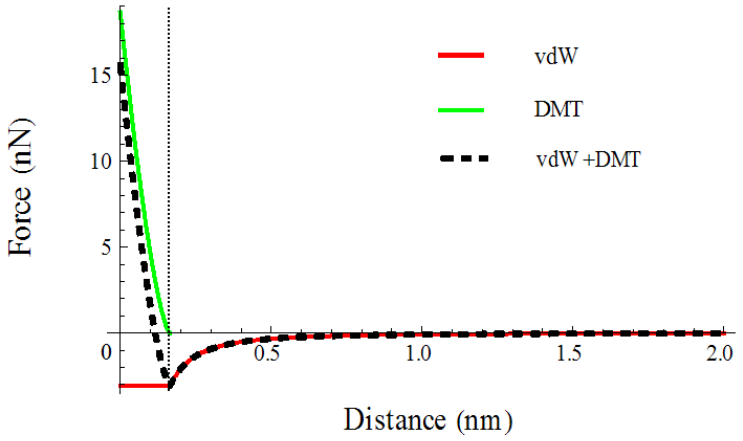

Figure 2.1 van der Waals and DMT forces. Attractive van der Waals force (red), repulsive DMT contact force (green) and resulting total force (black, dashed) between a sphere with a radius of 10 nm and a flat body, calculated for a Hamaker constant and effective Young's modulus of SiO_2 ($5 * 10^{-20}$ J and 66 GPa, respectively), and an intermolecular distance of 0.165 nm, according to [10].

both vdW and DMT forces, we can derive the basic force vs distance profile, given by

$$F_{\text{vdW+DMT}} = \begin{cases} -\frac{AR}{6z^2} & \text{for } z > a_0 \\ \frac{4}{3}E^*\sqrt{R}(a_0 - z)^{\frac{3}{2}} - \frac{AR}{6a_0^2} & \text{for } z \leq a_0 \end{cases} \tag{2.3}$$

Figure 2.1 shows the attractive van der Waals force, the repulsive DMT contact force and the resulting total force between a SiO_2 sphere with a radius of 10 nm and a flat body of SiO_2.

2.2 Adhesive interactions

When two bodies get into contact, adhesive forces may occur that hold the two bodies together. For example, adhesion may be due to the formation of chemical bonds, a liquid meniscus or non-elastic deformations. Thus, chemical and mechanical surface properties determine the adhesive interactions. The maximum force needed to seperate the two bodies is called adhesion force.

2.2.1 Capillary adhesion

In air, under the presence of certain humidity, the surfaces of many materials are covered (at least partly) with a water layer (for an extensive review see [58]). Moreover, the approach (and possible contact) of two bodies favors capillary condensation. Under these conditions, a liquid meniscus forms when two objects get into close proximity. The liquid bridge causes an attractive force between the interacting bodies which results from the van der Waals forces among the water molecules and the atoms of the interacting bodies.[59–61] The capillary force is the extra force needed to break the liquid meniscus. It depends on the surface properties, humidity, temperature and the geometry of the interacting bodies. Under moderate humidity conditions the capillary force may be longer ranged than the van der Waals force.[62]

Assuming thermodynamic equilibrium and a liquid that is well described with its macroscopic properties, an analytical expression of the capillary force is found for a sphere of radius R and a plane (as schematically illustrated in Figure 2.2).[10,57] In this approximation, the sphere radius is assumed to be much larger than the meniscus. The capillary force F_{cap} at a distance D can be approximated by,

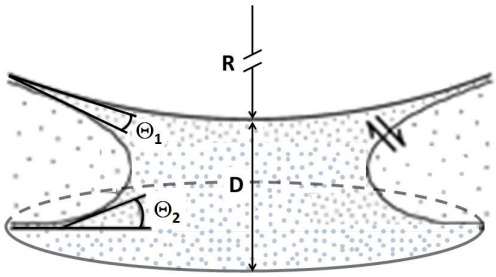

Figure 2.2 Schematic of the liquid meniscus forming between a sphere of radius R and a plane. Θ_1 and Θ_2 are the contact angles of sphere and plane, respectively, and D is the distance between sphere and plane.

$$F_{\text{cap}} \approx 2\pi R\gamma_{\text{LV}} \left(\cos\Theta_1 + \cos\Theta_2\right) \left[1 - \frac{D}{D_{\text{c}}}\right], \tag{2.4}$$

where D_{c} is the critical distance at which the liquid meniscus breaks,

$$D_{\text{c}} \approx \left(\cos\Theta_1 + \cos\Theta_2\right) \frac{\gamma_{\text{LV}} V_{\text{m}}}{R_{\text{g}} T \log\left(\frac{1}{H}\right)}. \tag{2.5}$$

Θ_1 and Θ_2 are the contact angles of sphere and plane, respectively, γ_{LV} is the surface tension of water at the liquid-vapor interface, V_{m} is the molar volume of water, R_{g} the ideal gas constant, T the temperature, and H the relative humidity.

As expected, equation (2.4) confirms that the capillary force is zero for hydrophobic materials ($\Theta_1 = \Theta_2 = 90^{\text{o}}$) (no meniscus forms). Otherwise, the capillary force is proportional to the radius of the sphere, and the capillary adhesion force ($D = 0$) is independent of the relative humidity.

On the other hand, the critical distance at which the meniscus breaks, depends on the relative humidity - it increases with humidity.

When the objects are nanoasperities, the meniscus will be approximately of the same size as the nanoasperity, and the above given approximation does not hold. To overcome this shortcoming, Sahagún et al. have developed a model for capillary condensation which is based on energetical considerations.[6] An extensive description of the model is given in [57]. The model, which has to be resolved numerically, has been extended to different geometries of the nanoasperities, to determine how size and geometry of nanometric objects influence capillary forces. This question is discussed in detail in Chapter 3.

2.2.2 Dissipation due to adhesion hysteresis

When two bodies are brought into contact, a rearrangement of the atoms at the contact point occurs, leading to inelastic deformations at the nanoscale (see Figure 2.3).[7] This contact interaction is dissipative. At the nanoscale, the atomic rearrangements will affect the surface energy of the two bodies in contact. Thus, the surface energy may be significantly different when the bodies are approached (before rearrangements have taken place) or separated (after rearrangements), giving rise to an adhesion hysteresis.

Other processes different from atomic rearrangements can contribute to the adhesion hysteresis, for example the formation of a capillary neck.[4–6] Due to the liquid neck, the bodies adhere to each other. Upon separation, the neck elongates until it eventually breaks. More work is needed to separate both surfaces than the work that was originally gained by bringing them together. Consequently, this adhesive process is also hysteretic.

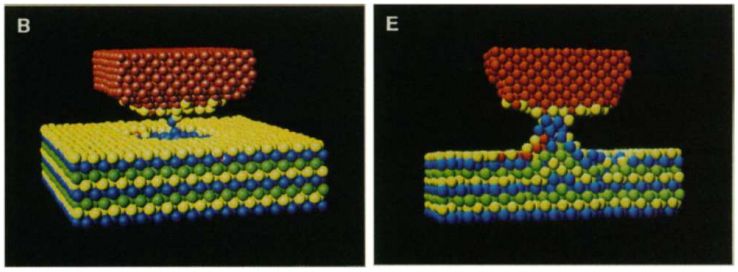

Figure 2.3 Atomic configuration when two bodies are separated after contact, determined by Molecular Dynamics simulations for a Ni sphere (Ni atoms are colored red) and a flat Au surface (Au layers are colored yellow, blue and green). Independently of whether indentation follows contact, a connective neck forms: When no indentation occurs, the neck is atomically thin (left), while an extensive connective neck forms when indentation follows contact (right), and Ni atoms as well as Au atoms from the first, second and third topmost layers are incorporated into the neck. From [7]. Reprinted with permission from the American Association for the Advancement of Science (AAAS).

Relating the dissipated power, measurable with the Atomic Force Microscope, to the processes that occur at the nano-contact poses a major challenge. The role adhesion hysteresis plays in dynamic AFM will be discussed in Chapter 4.

2.3 Introduction to Atomic Force Microscopy

Atomic Force Microscopy (AFM) has been developed as one of the scanning probe microscopy techniques in 1986 by Binnig, Quate and Gerber,[63] after the invention of Scanning Tunneling Microscopy (STM) in 1981 (for which Binnig and Rohrer obtained the Nobel prize in 1986). Since its invention, the Atomic Force Microscope has evolved as a versatile tool for characterizing material surfaces at the nanometric (and even atomic) scale.

Nowadays, Atomic Force Microscopy can do much more than just obtaining topography maps: further material properties can be obtained with high lateral resolution of only few nanometres, molecular recognition sites can be determined and binding forces quantified, but also applications not related to material characterization have been developed, like nanolithography through local oxidation[1] and dip pen lithography,[2] to name a few. The studies performed in this thesis are concerned with the use of Atomic Force Microscopy for material surface characterization, on which the following discussion will be focussed.

In AFM, the forces acting between two objects are measured, wherat at least one of the objects, the AFM tip, can be as small as few atoms at the apex (for example using a carbon nanotube). As discussed earlier, the employed materials and measurement conditions determine which interaction forces between tip and sample dominate. Usually, the forces to consider are: van der Waals forces, mechanical contact forces, capillary forces (when operating in air), forces related to chemical bonding, electrostatic forces, magnetic forces, etc. AFM is also referred to as Scanning Force Microscopy (SFM) to emphasize that probed forces are not necessarily of atomic range, but may be of longer range (for example of electrostatic or magnetic nature).

How the AFM works - basic principles

The basic components of the AFM are the microcantilever fixed at one end (this end is called the base) with a tip protruding at the other end (see Figure 2.4) and the sample. The tip, typically of nanometric apex, senses the sample, and the tip-sample interaction forces F_{ts} (and their gradients) modify the cantilever position or movement. Cantilever movement (and therewith the interaction force (gradient)) can be detected in several ways,

but the most common way is by a laser beam reflecting off the cantilever's back onto a position-sensitive four quadrant photodiode. The sample is positioned on a piezoelectric tube which allows for moving the sample in 3D space very precisely. A scheme of the basic AFM components is shown in Figure 2.4. The user controls the microscope on a PC by using a specific software which communicates with the electronic control unit that analyzes the cantilever movement (the signal received from the photodiode) and controls both piezo scanner and cantilever excitation accordingly.

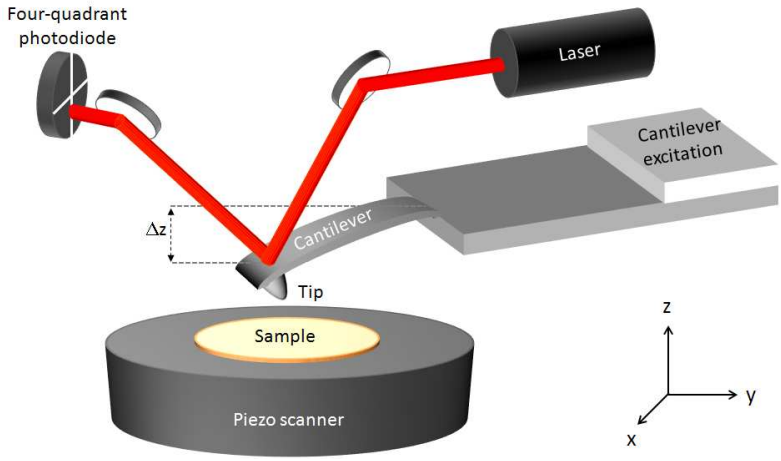

Figure 2.4 Schematic of the basic components of an Atomic Force Microscope. The sample is mounted on a piezoelectric scanner which moves the sample in all three spatial directions with high precision. The tip-sample interaction force is determined through the cantilever deflection Δz, determined by a laser beam reflected on the cantilever's back side and registered in a four quadrant photodiode. In dynamic mode the cantilever is usually excited by a small piezo. The scheme is not drawn to scale. For reasons of clarity, electronic control unit and PC are not included in this scheme.

Cantilever and tip A wide variety of cantilevers and tips are commercially available to satisfy the needs of the large community using AFM in many different fields (it is estimated that by 2006 there were already about 10 000 Force Microscopes in use around the world)[64]. Most commonly, cantilevers and tips are made of monocrystalline silicon or silicon nitride. Tips terminate in a nanometer sized apex (Figure 2.5). Most cantilevers are coated with a highly reflective material on their back. The tip apex is of utmost importance in AFM experiments, since local forces between the tip apex and the relevant sample region are responsible for the cantilever deflection (or the changes in cantilever movement in dynamic modes). Thus, the tip apex plays a fundamental role for AFM measurements - a fact that is often neglected and results are solely related to the sample. The importance of the tip apex for capillary interactions is discussed in Chapter 3.

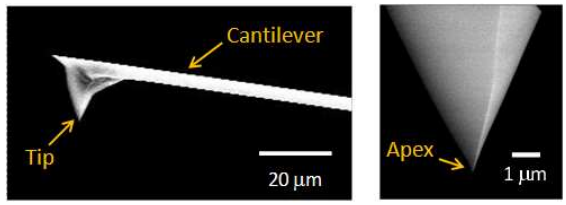

Figure 2.5 SEM images of cantilever and tip from Nanosensors (type PointProbe® Plus). Images were taken at 25 kV.

Imaging For acquiring images of the sample surface, the sample is scanned line by line with the piezo scanner (see Figure 2.4). For standard applications, an image usually consists of 512 x 512 pixels, and typical scanning speeds are around one line per second, so that one image is taken in 5–10 min. Naturally, for particular applications these values may vary considerably. The maximum image size depends on the characteristics of the piezo scanner; commonly used scanners allow for scanning up to 70 µm

with scanners for large scans over rough samples, or rather 10 μm with scanners for high resolution. Lateral resolution depends on tip size and measuring conditions. Further details on AFM imaging are presented in Section 2.6.

Spectroscopy In the terminology used by the AFM community, performing approach-retraction curves is called spectroscopy. It represents a modality where a variety of parameters (normal force, amplitude, phase...) can be obtained as a function of the tip-sample distance. Generally, approach-retraction curves are performed at a determined spot of the sample - the sample area is not scanned. In contrast, when imaging, a certain sample area is scanned at a determined tip-sample distance. There exist, however, combinations of the two, where approach-retraction curves are performed while scanning (for example in the *jumping mode* described on page 49). The two spectroscopy modes relevant for this thesis are discussed in Section 2.5.

Feedback control and setpoint In many measuring applications a feedback control mechanism is used to maintain a parameter of interest constant by varying another. The most common example is to maintain the cantilever deflection at a constant value by moving the sample towards the tip or retracting it; in this way the tip-sample force is maintained constant. The value to which the parameter in question is to be fixed is called *setpoint*. The feedback control mechanism that is generally used in AFM is a PI circuit (acting on the proportional (P) and the integral (I) of the error between the actual value and the setpoint) which allows for maintaining stable measurement conditions. Several feedback loops may work simultaneously, each controlling a different parameter.

Operation modes

Today, after 25 years of development, a variety of AFM operation modes are at the user's disposal, offering the possibility to study diverse characteristics of a variety of samples (biological, magnetic, semiconductor, ...) in liquids, air or vacuum. Due to this versatility, AFM has found its place in a wide spectrum of applications. AFM operation modes can first be divided into static and dynamic operation modes, which will then ramify further to more distinctive ones.

Static operation When AFM was invented in 1986, it was operated in what today we call the static mode, since, in contrast to the later developed dynamic modes, the cantilever is not brought to oscilate. The tip-sample interaction forces F_{ts} lead to a cantilever bending Δz, which, if we neglect the spatial extension of the cantilever and apply the point mass model, is given by Hooke's law

$$F_{\mathrm{ts}} = -k\Delta z, \tag{2.6}$$

where k is the effective elastic constant of the cantilever (out of contact), or rather of cantilever and sample (at contact). The cantilever deflection Δz is determined by the laser beam reflected on the cantilever's back side and registered in the four quadrant photodiode (see Figure 2.4). By knowing the force constant k, the force F_{ts} acting between tip and sample can be determined.

Static mode can be used in steady tip-sample contact or out of contact (for example to measure electrostatic forces)[65]. In the contact mode, soft (for example biological) samples are deformed by the lateral and normal

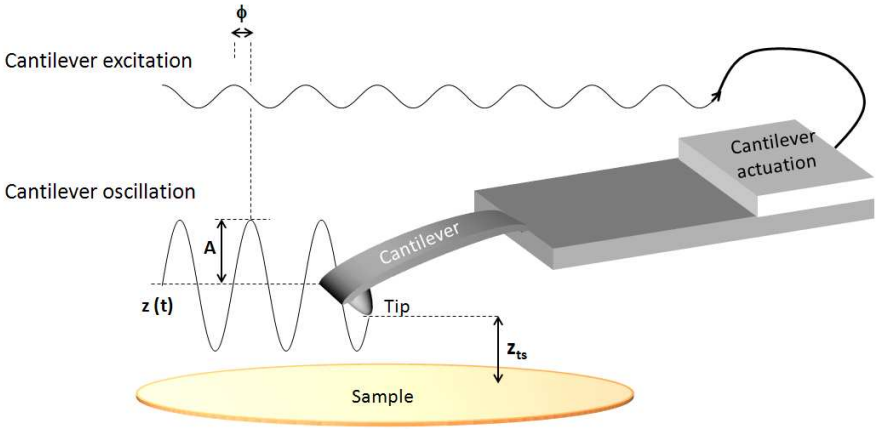

Figure 2.6 Schematic of dynamic AFM operation. The cantilever oscillation of amplitude A is phase shifted (phase shift ϕ) with respect to the cantilever excitation.

forces exerted by the tip. To solve this problem, the dynamic operation has been developed.

Dynamic operation Only one year after its invention,[66] a significant step in the development of AFM was taken when the cantilever was brought to oscillate at its resonance frequency close to the surface and the effects of the tip-sample interaction force gradients on this oscillation were studied (see the schematic representation in Figure 2.6). Tip-sample force gradients modify the cantilever oscillation which is described by the oscillation amplitude A, the phase shift between cantilever excitation and oscillation ϕ and the resonance frequency ω_{res}. In consequence, the proximity to the sample surface can be adjusted by controlling any of these parameters. In the dynamic mode, lateral forces are almost eliminated and normal forces minimized, which permits to analyze soft biological samples without deforming them.

Cantilever oscillation is usually achieved mecanically by transferring the vibration of a piezo to which the silicon chip supporting the cantilever is attached (Figure 2.6). When working in liquids, however, the mecanical vibration is transferred through the liquid to the liquid cell and further oscillations (of components other than the cantilever) are excited, making the determination of the cantilever's resonance frequency difficult. Therefore, in liquids other cantilever actuation mechanisms are used which act exclusively on the cantilever, for example magnetic[67] or magnetostrictive[68] actuation.

In the following, dynamic operation will be described with particular detail, emphasising the aspects relevant in this thesis.

2.4 Dynamic Atomic Force Microscopy

To understand the basic notions of dynamic operation, it is instructive to consider the *point mass model*, a simple model which describes the cantilever as a point mass with effective mass m, effective force constant k and effective coefficient of friction γ. Although this model presents limitations (e.g. it does not take into account higher oscillation modes), it allows to understand the basic phenomenology necessary to operate an AFM in dynamic modes and interprete experimental results.[69–72]

The equation of motion describing the deflection $z(t)$ of the cantilever is given by

$$\ddot{z} + \frac{\omega_0}{Q}\dot{z} + \omega_0^2 z = F_{\mathrm{exc}}(t) + F_{\mathrm{ts}}, \tag{2.7}$$

where ω_0 is the natural frequency of the cantilever given by

$$\omega_0^2 = \frac{k}{m}, \tag{2.8}$$

Q its quality factor (its definition depends on the convention used),

$$Q = \frac{m\omega_0}{\gamma}, \tag{2.9}$$

$F_{\mathrm{exc}}(t)$ the external force exciting the cantilever, approximated by

$$F_{\mathrm{exc}}(t) = F_{\mathrm{exc}}^0 \cos \omega t, \tag{2.10}$$

and F_{ts} the tip-sample interaction force.

While this is the most basic equation describing the cantilever deflection, its solution is rather complex, as the terms for the tip-sample interaction forces generally do not allow for an analytical integration of equation (2.7). Through a numerical intergration, though, the cantilever movement can be determined for different tip-sample interaction forces.

Simple expressions for amplitude and phase can be obtained in absence of tip-sample forces (sufficiently far from the surface).

$F_{\mathrm{ts}} = 0$ (far from the surface)

The solution of equation (2.7) with $F_{\mathrm{ts}} = 0$ (forced damped oscillator) presents a transient and a steady state term, whereby the steady state term, usually considered to be predominant, is given by

$$z_{\mathrm{s}}(t) = A\cos\omega t + \phi. \tag{2.11}$$

The amplitude can be written as

$$A = \frac{A_0\omega^2/Q}{\sqrt{(\omega_0^2 - \omega^2)^2 + \omega^2\omega_0^2/Q^2}}, \tag{2.12}$$

where A_0 is the free oscillation amplitude. The phase is given by

$$\phi = \arctan\frac{\omega\omega_0}{Q(\omega_0^2 - \omega^2)}. \tag{2.13}$$

If the cantilever is excited at ω_0, then $A = A_0$ and $\phi = 90^{\mathrm{o}}$ (see the blue curve in Figure 2.7).

$\underline{F_{\mathrm{ts}} \neq 0}$

When the tip is close enough to the surface, tip-sample interaction forces F_{ts} become significant, and the cantilever behaves like an oscillator with an effective force constant k'. Taking into account only the linear term of the Taylor series for $F_{\mathrm{ts}}(z_{\mathrm{ts}})$ (which is a good approximation for small oscillation amplitudes), the effective cantilever force constant is[73]

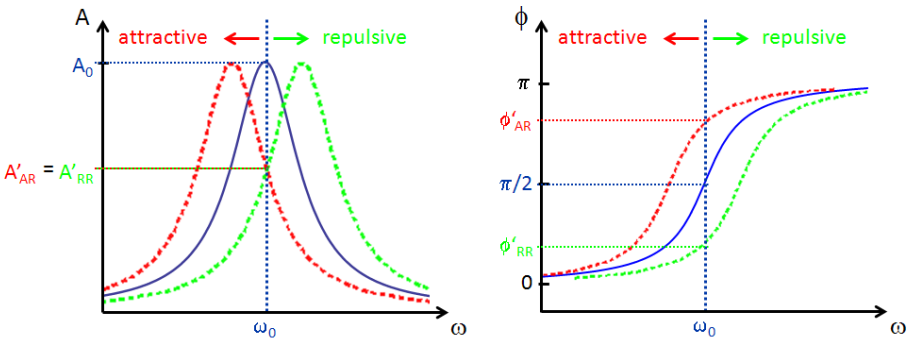

Figure 2.7 Resonance curve under the influence of attractive and repulsive forces. Under the influence of an external force the resonance frequency changes, leading to a shift of amplitude (left) and phase (right) curves. If the cantilever excitation frequency is fixed to $\omega = \omega_0$, the cantilever oscillation amplitude will decrease as tip-sample interaction forces increase and the cantilever resonance frequency moves away from ω_0. The phase, on the other hand, will move away from 90° (it will be $> 90°$ if tip-sample forces are attractive and $< 90°$ if they are repulsive).

$$k' = k - \frac{\mathrm{d}F_{\mathrm{ts}}}{\mathrm{d}z_{\mathrm{ts}}}, \tag{2.14}$$

which, considering equation (2.8), changes the resonance frequency of the cantilever (red and green curves in Figure 2.7). If the excitation frequency is fixed to $\omega = \omega_0$, the cantilever oscillation amplitude will decrease as tip-sample interaction forces increase and the cantilever resonance frequency moves away from ω_0. The phase, on the other hand, will move away from 90° (it will be $> 90°$ if tip-sample forces are attractive and $< 90°$ if they are repulsive).

This simple model illustrates that tip-sample interaction forces $F_{\mathrm{ts}}(z_0)$ change the cantilever oscillation. Thus, the parameters characterizing the oscillation - resonance frequency $\omega_0(z_0)$, amplitude $A(z_0)$ and phase shift

$\phi(z_0)$ - can be used as control parameters to adjust the proximity to the sample surface.

There are two well established dynamic operation modes: Amplitude Modulation Atomic Force Microscopy (AM-AFM),[66] also called *tapping mode*, where the oscillation amplitude is maintained constant, and Frequency Modulation Atomic Force Microscopy (FM-AFM),[74] often referred to as *non-contact* AFM, where the oscillation frequency is maintained constant at resonance. While FM-AFM is mostly operated in vacuum (where true atomic resolution can be obtained)[75,76], AM-AFM yields good results for operation in air or liquids.[77] An extensive review on both dynamic operation modes is given in Reference [73], and cantilever dynamics in AM-AFM is reviewed in Reference [78]. AM-AFM is the mode on which parts of this work have been focussed, and in the following a more detailed description of this mode shall be given.

Amplitude Modulation The cantilever is forced to oscillate at a fixed frequency close or at resonance. Far from the surface, when interaction forces are zero, the tip oscillates with a certain oscillation amplitude, the free oscillation amplitude A_0 (typically 1–100 nm), and the phase lag between cantilever excitation and oscillation ϕ is 90°. Once tip and sample are close enough so that interaction forces between both become significant, the oscillation amplitude decreases approximately linearly with decreasing mean tip-sample distance. Thus, by fixing the oscillation amplitude to a value smaller than A_0 (setpoint amplitude A_{sp}), the tip-sample distance will be held constant. ($A_{\mathrm{sp}}/A_0 < 1$). When the tip, scanning the sample parallel to the sample surface, approaches a protrusion on the sample surface, the sample has to be retracted in order to evade the diminishing of the oscillation amplitude and to maintain the amplitude constant. Thus, topography profiles and maps are obtained through the piezo movement.

The above said is true if tip-sample interaction forces are constant over the scanned sample surface. When tip-sample interaction forces change throughout the scanned area (for example when the sample is of heterogeneous material), the amplitude vs distance profile varies. Consequently, scanning with a constant oscillation amplitude does not correspond to scanning at a constant tip-sample distance, and ultimately an erroneous topography profile is obtained.[79]

If the cantilever excitation frequency is fixed to $\omega = \omega_0$, the phase will move away from 90^o as tip-sample interaction forces increase and the cantilever resonance frequency moves away from ω_0 (Figure 2.7). Several authors have studied the relation of phase maps to variations in material properties such as adhesion, elasticity or viscoelasticity.[80–83] Optionally, a second feedback loop can be turned on which maintains the phase constant to $\phi = 90^o$ by varying the excitation frequency ("phase-locked loop"). In this way, the cantilever will stay in resonance, which might improve the operation in certain measurement conditions.

Bistability Due to the presence of attractive and repulsive forces and the non-linearity of the tip-sample interaction, two stable oscillation states may coexist in a certain mean tip-sample distance range. In this range, the oscillation amplitude, the key parameter in AM-AFM, may adopt two values (see Figure 2.10 in Section 2.5). Experimentally, the cantilever only oscillates in one state at a time, but may jump from one state to the other which results in instable imaging conditions. The coexistance depends on sample properties (like elasticity and adhesion) and operational parameters (free oscillation amplitude A_0 and cantilever force constant k). For certain measurement conditions (generally speaking for low oscillation amplitudes A_0) the system stays in the "low amplitude" state (see Chapter 4). The phase identifies the regime unambiguously:

$\phi > 90°$ in the "low amplitude" atate and $\phi < 90°$ in the "high amplitude" state.

On the other hand we can differenciate two operating regimes: the attractive regime (AR), in which net tip-sample interaction forces (averaged over one oscillation cycle) are attractive, and the repulsive regime (RR), where net tip-sample interaction forces are repulsive. When tip-sample forces are repulsive on average the tip touches the sample in most cycles (intermittent contacts). On the other hand, when tip-sample forces are attractive on average, images can be acquired with no (or few) tip-sample contact(s). Therefore, the nomenclature *tapping mode* is misleading if AM-AFM is operated in AR. It is important to note that here only average forces are considered (over several oscillation cycles). However, cantilever dynamics are not trivial and it is not clear what happens in each single oscillation cycle. This problem is addressed in Chapter 4.

Generally, the "low amplitude" state is associated with the AR, and the "high amplitude" state with the RR. It has been shown that this association is correct if the following three conditions apply: 1.) the cantilever deflection is negligible in comparison to the oscillation amplitude, 2.) the tip-sample dissipation is negligible in comparison with dissipation to the environment, and 3.) the interaction forces are only significant at the oscillation minima.[84] A detailed description of the phenomenon of bistability in AM-AFM is given in [73, 84].

Further development of dynamic modes Other operation modes are being developped to overcome problems in certain measurement conditions and obtain further information on tip-sample interaction forces and material properties. These modes include Phase Modulation (PM-AFM);[85] where the constant tip-sample distance is achieved by maintaining

the phase shift between cantilever excitation and oscillation constant, and Drive-amplitude Modulation (DAM-AFM), where the constant tip-sample distance is achieved by maintaining the power dissipation constant (maintaining both oscillation and excitation amplitude constant)[86,87]. A further recent development is Multifrequency AFM (MF-AFM),[88–90] where the beforementioned parameters (amplitude, phase shift and oscillation frequency) are controlled for various cantilever resonances simultaneously.

A virtual environment for dynamic AFM (VEDA) has been developed, which is a suite of freely available, open-source simulation tools that allow to simulate dynamic AFM operation with different tip-sample interaction models in a variety of operation modes.[91]

2.5 Spectroscopy

The way how tip-sample forces (and related parameters) depend on the tip-sample distance can give further insight into material properties. AFM force spectroscopy offers a high force resolution of few piconewtons and a vertical distance resolution of less than 0.1 nm. Curves are generally performed without feedback. A certain distance for the vertical piezo movement is fixed both for approaching the sample to the tip and retracting it from it, whereby the retraction can be forced by limiting a determined parameter (for example the cantilever deflection). In this way, the tip-sample contact can be controlled or avoided. Furthermore, the velocity of the sample movement can be controlled.

Force spectroscopy can be performed in static and dynamic mode (pages 31ff.). In the following, a more detailed description of static force vs distance curves and dynamic amplitude and phase vs distance curves will

be given, which play a predominant role in this thesis. Force spectroscopy is treated in depth in References [92, 93].

Static Force vs Distance curves As already mentioned in Section 2.3, the tip-sample interaction force leads to the cantilever deflection Δz. By approaching the sample towards the tip and retracting it from it, cantilever deflection vs piezo displacement curves are obtained which, knowing the cantilever force constant k, can then be converted to force vs piezo displacement curves with equation (2.6).

An example force vs piezo displacement curve for a cantilever of force constant $k = 2.7\ \mathrm{Nm}^{-1}$ is shown in Figure 2.8. Far from the surface (zero vertical piezo displacement) tip-sample interaction forces are negligible (position A in Figure 2.8), and piezo elongation with the related tip-sample approach does not implicate a cantilever deflection (*zero force line*). At some point, tip-sample interaction forces are strong enough to produce a detectable cantilever bending - towards the sample if forces are attractive and away from the sample if they are repulsive. If no electrostatic or magnetic forces are present, attractive van der Waals forces predominate and lead to a cantilever bending towards the sample (position B in Figure 2.8). The bending Δz depends on the force constant k. When the derivative of the tip-sample interaction force exceeds the cantilever force constant the tip snaps into contact with the sample surface (*jump to contact*, position C). Extending the piezo further (tip and sample are in contact, and the sample is further approached to the cantilever base) the cantilever bending towards the sample will diminish and eventually turn its sign (position D). In contact, tip and sample may deform elastically (reversibly) and plastically (irreversibly). The cantilever deflection depends approximately linearly on the vertical piezo displacement (*contact line*), whereat the slope depends on sample and

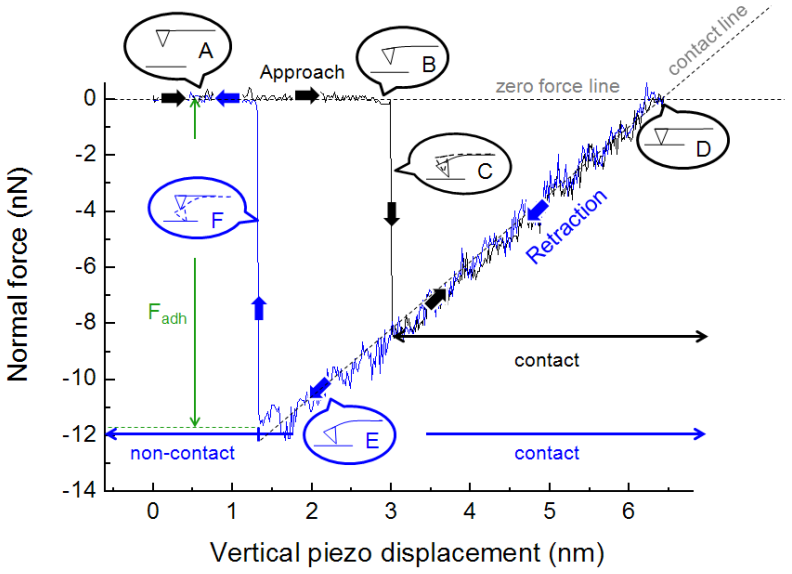

Figure 2.8 Force vs piezo displacement curve. Experimentally obtained curve with a cantilever of force constant $k = 2.7$ Nm^{-1}. The sample is first approached towards the cantilever base (black curve) and then retracted from it (blue curve). The cantilever bending (as schematically indicated in the insets) corresponds to the (attractive or repulsive) net force acting on the cantilever.

cantilever stiffness. In particular, if the sample is much stiffer than the cantilever, the cantilever deflection equals the piezo displacement (and the photodiode sensitivity can be calibrated, see Section 2.7 on page 52).

Once the piezo retracts, elastic deformations will recover while plastic deformations will not. Thus, the force vs piezo displacement curves reveal information on the elasto-plastic behaviour of tip and sample. When deformations are elastic, contact lines of approach and retraction curves overlap (as is the case in the presented figure). If, on the other hand, plastic or viscoelastic deformations have taken place, the contact lines differ (loading-unloading hysteresis). Adhesion will keep the tip in

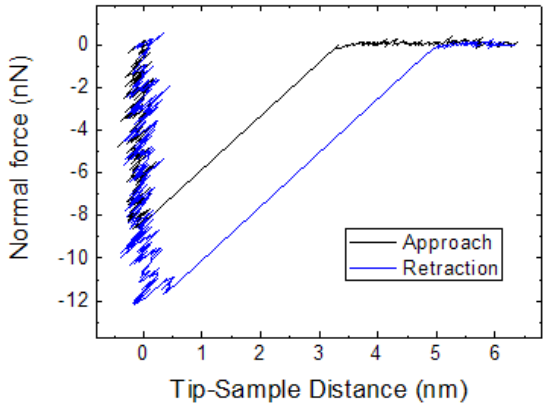

Figure 2.9 Force vs tip-sample distance curve obtained from Figure 2.8. The tip snaps into contact with the sample at a distance of 3.3 nm, and the jump-off-contact distance is 5.0 nm. In order to obtain complete force vs tip-sample distance curves (with no jump-to-contact) one can employ stiff cantilevers on the cost of obtaining less force resolution.

contact with the surface until until the cantilever force overcomes the adhesion force and the tip will snap out of contact (position F). Adhesion forces can include capillary forces and forces due to chemical or otherwise adhesive bonds. For hydrophilic surfaces under ambient conditions the capillary force, which is the attractive force caused by the liquid bridges formed between two objects in contact, are predominant over other surface forces. Naturally, the liquid bridge volume, and thus the capillary force magnitude, depend on relative humidity. How exactly these capillary forces depend on relative humidity when objects become as small as a few nanometres will be discussed in Chapter 3.

The force vs piezo displacement curve can be converted to force vs tip-sample distance curves, whereby the tip-sample distance in each point of the curve is given by the horizontal distance of this point to the contact line. From the force vs tip-sample distance curve (Figure 2.9) one can

read easily that the tip snaps into contact with the sample at a distance of 3.3 nm, and the jump-off-contact distance is 5.0 nm. In order to obtain complete force vs tip-sample distance curves with no jump-to-contact (see Figure 2.1) one can employ stiff cantilevers on the cost of obtaining less force resolution.

Approach-retract curves can be performed while scanning the sample (*jumping mode*), obtaining topography and adhesion images simultaneously (see Section 2.6, page 49).

Dynamic Amplitude and Phase vs Distance curves Analog to the static force vs distance curves, dynamic curves are obtained when the cantilever is oscillating during approach and retraction. During the approach and retraction cycle the oscillation amplitude, phase and resonance frequency vary in response to changes in the interaction forces. An example of an approach-retract curve for a system which enters the RR is shown in Figure 2.10; the black curve represents the approach curve and the blue curve the retraction curve. Far from the surface (in Figure 2.10 the vertical piezo displacement is 0 nm) tip-sample forces are small and the cantilever oscillates with the free oscillation amplitude $A_0 = 41$ nm (the phase is 90^o). While approaching the sample, attractive tip-sample forces lead to a reduction of the oscillation amplitude and a rise in the phase shift to values $> 90^o$ (see also Figure 2.7). At a certain mean tip-sample distance, the system enters the RR - the oscillation amplitude increases abruptly and the phase jumps to values $< 90^o$. When retracting the tip from the sample, the system stays in the RR until - at a higher tip-sample distance than in the approach curve - it finally enters the AR again. The tip-sample distance at which the transition between the two regimes occurs is generally different for approach and retraction curves, giving rise to a hysteresis in amplitude and phase.

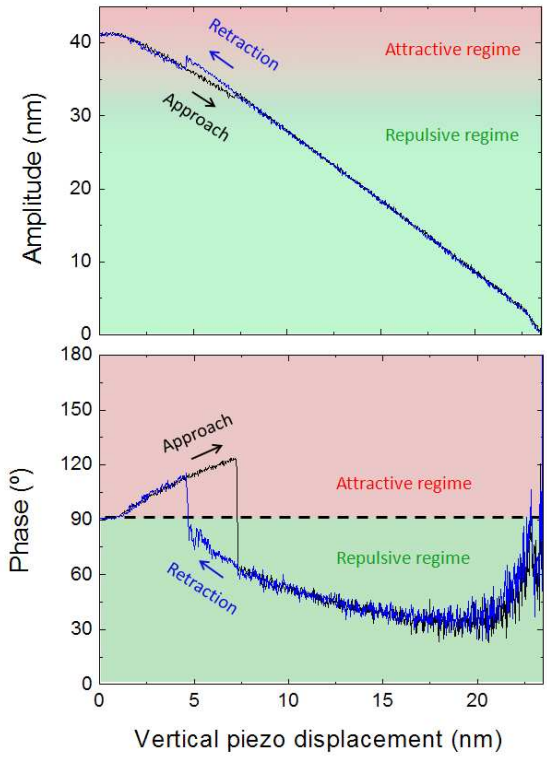

Figure 2.10 Bistability in amplitude and phase. Amplitude and phase measured with a silicon tip (Nanosensors PPP, $k = 1.4$ Nm^{-1}) on a mica sample. The tip is approached towards the sample surface (black curve) and subsequently retracted (blue curve). Far from the surface (vertical piezo displacement 0 nm) tip-sample forces are small and the cantilever oscillates with the free oscillation amplitude $A_0 = 41$ nm (the phase is 90°). While approaching the sample, attractive tip-sample forces lead to a reduction of the oscillation amplitude and a rise in the phase shift to values $> 90°$ (see also Figure 2.7). At a certain mean tip-sample distance, the system enters the RR - the oscillation amplitude increases abruptly and the phase jumps to values $< 90°$. When retracting the tip from the sample, the system stays in the RR until - at a higher tip-sample distance than in the approach curve - it finally enters the AR again. When measuring in AM-AFM there is an amplitude range where measurement conditions are unstable, since the same setpoint amplitude is obtained for two different tip-sample distances, so that the system might jump from the attractive regime to the repulsive regime and vice-versa.

From amplitude and phase, dissipated power can be calculated (equation (4.1)). The link between dissipated power and adhesion hysteresis is discussed in Chapter 4. To achieve a normalization for different free oscillation amplitudes, curves are often represented vs A/A_0 (Figure 4.2).

2.6 Imaging

Topography image Generally, in all imaging operation modes the tip-sample interaction is controlled by a feedback loop which allows for maintaining the AFM tip at a constant tip-sample distance close to or in contact with the sample surface, thus allowing for the acquisition of the sample topography and preventing tip damage due to an uncontrolled tip-sample collision. The tip-sample interaction is not controlled directly, but rather through related parameters (e.g. cantilever deflection or oscillation amplitude; specific examples are discussed further on). An adequate value for this parameter has to be chosen to achieve the desired measurement conditions (to measure out of contact, in (intermittent) contact, or impressing more or less on the sample surface). The value to which this parameter is fixed is called "setpoint". Independently of the parameter which is used as control parameter to obtain the sample topography through the above mentioned feedback loop, it is always the piezo movement needed to compensate for the sample topography and therewith maintain the feedback parameter constant which is interpreted as topography image. Apart from the principal feedback loop which fixes the tip-sample distance and returns the sample topography, further feedback loops may be turned on to obtain further information on material properties (magnetic, electrostatic...) and relate these to the sample topography. For certain applications, however, images are taken without

feedback control (for example for obtaining atomic resolution in contact mode).

Imaging operation modes

A variety of imaging operation modes has been developed, and the selection of the adequate operation mode depends on the particular application, considering the measurement environment (vacuum, air or liquids), the delicateness of the sample and the material properties that should be obtained aditionally to the topography (adhesion, friction, electromagnetic properties...). For completeness, a brief overview over the most common imaging modes shall be given, although in this thesis all images were obtained in the dynamic mode.

Contact Mode Contact mode is one of the static modes, and it is this mode in which first AFM measurements were performed back in 1986. The tip is brought into contact with the sample and scanned ("dragged") over the sample at a constant tip-sample force (normal to the surface), achieved by approaching or retracting the sample with the piezoelectric scanner (Figure 2.4). If, for example, the tip arrives at a protrusion on the sample surface, the sample has to be retracted for the normal tip-sample interaction force to remain constant, as illustrated in Figure 2.11. The piezo movement of the sample reflects, thus, the profile of the sample topography. By scanning the tip over a certain sample area, line after line, topography profiles are appended one to the other, and images of the sample topography are obtained. When operating in contact, the elastic constant k in equation (2.6) is given by

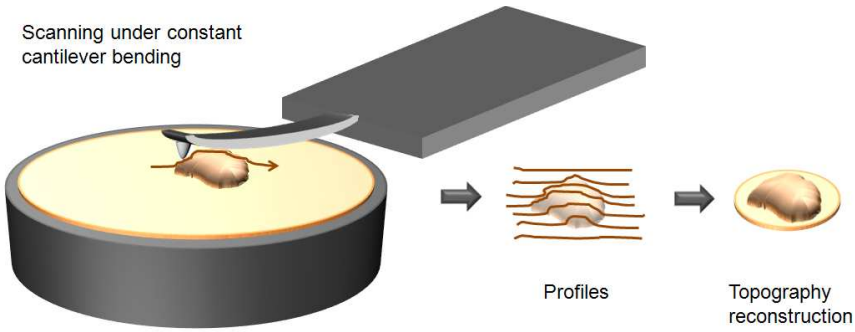

Figure 2.11 Imaging in the contact mode. The tip is brought into contact with the sample and scanned ("dragged") over the sample at a constant tip-sample force (normal to the surface), achieved by approaching or retracting the sample with the piezoelectric scanner. If the tip arrives at a protrusion on the sample surface, the sample has to be retracted for the normal tip-sample interaction force to remain constant. The piezo movement of the sample reflects, thus, the profile of the sample topography. By scanning the tip over a certain sample area, line after line, topography profiles are appended one to the other, and images of the sample topography are obtained. The scheme is not drawn to scale.

$$k^{-1} = k_{cantilever}^{-1} + k_{sample}^{-1}. \tag{2.15}$$

To obtain high force resolution, evade dragging or deforming of the sample material and minimize tip damage, cantilevers of low force constant ($k = 0.01\ \mathrm{Nm}^{-1}$) are used. In contact mode, the interaction force has a lateral component due to friction. Thus, friction maps can be obtained from the lateral force.

Tip-sample interaction forces responsible for cantilever bending in contact are short-range repulsive forces, and therefore, in principle, spatial resolution is high. However, several obstacles (mainly due to van der Waals forces and adhesion) complicate the task of obtaining true atomic

resolution in air and ultra-high vacuum (UHV). When working in UHV, FM-AFM presents an adequate alternative to obtain atomic resolution.

Dynamic modes Since lateral forces on the sample are almost eliminated and normal forces minimized, the dynamic mode is the most adequate for studying delicate biomolecules, polymers, cells, or any other delicate or soft matter.

A special implementation of dynamic modes allows for determining molecular recognition sites (for determining the binding forces quantitatively, see Section 2.5): images of topography and specific recognition between a functionalized scanning probe and the sample can be recorded simultaneously by evaluating oscillation minima and maxima separately when working with a heavily damped system (typically in a liquid environment) in intermittent contact mode, thus separating localized attractive forces caused by recognition events and repulsive ones during contact.[94] Theoretical results predict that also the phase shift could be used to detect recognition sites,[95] which presents an advantage since no extra electronics is necessary.

Jumping mode In jumping mode[96,97] a static force vs distance curve (Section 2.5, page 41) is performed in each pixel of the scanned area, so that topography and adhesion force maps are obtained simultaneously. Jumping mode is less invasive than contact mode since lateral forces are eliminated and normal forces can be kept low by chosing soft cantilevers. Moreover, information on further material properties can be obtained through the adhesion maps when the tip is covered with molecules of interest. For example, by covering the tip with hydrophobic molecules and measuring the adhesion force on living cells in water, nanoscale variations

in the hydrophilicity of the cell surface are determined and related to topographic features.[98]

2.7 Practical aspects for operating an Atomic Force Microscope

Resolution Atomic Force Microscopy offers a very high vertical resolution (commonly up to sub-ångström), and up to atomic lateral resolution. Lateral resolution is limited by the tip apex dimensions and depends on the operation mode and the measurements conditions.[99] From Hooke's law (equation (2.6)) we can deduce that the lowest detectable force depends on the lowest detectable cantilever deflection and the cantilever force constant. The force constant is directly related to the cantilever dimensions. For a rectangular cantilever the force contstant is given by[100]

$$k = \frac{3Ebh^3}{4L^3}, \tag{2.16}$$

with E being Young's modulus of the cantilever material, and b, h and L the cantilever width, thickness and length, respectively. Typical cantilever dimensions are 100–300 µm in length, 20–50 µm in width and 1–10 µm in thickness. By using micrometre sized cantilevers, force constants are low (typically in the range of 0.1 Nm^{-1} to 40 Nm^{-1}) and forces as small as 100 pN to few nanonewtons can be detected. For comparison: the necessary force to break a covalent bond is in the range of nanonewtons.

Noise Instrument and thermal noise limit resolution. While thermal noise is inherent to the system, instrument noise can be reduced by adequate design of the components. Instrument noise arises from different sources, of which the most significant are interference from the laser, air currents around the instrument and electrical noise such as shot noise and Johnson-Nyquist noise of the photodiode. Among the standard strategies to reduce noise, which have also been applied in the presented experiments, are the focusing of the laser spot onto the cantilever back at the "exact" tip position, and the enclosing of the microscope in a chamber to protect it from air currents and vibrations.

Image processing In many cases, some image processing is necessary to reduce measuring artefacts. Commonly images need to be levelled (subtracting a local or global plane) due to the tilted position of the sample or scanner and thermal drift. Further image processing includes filtering to eliminate noise at a certain frequency. It is important to register all performed processing steps and preserve the original images.

Lock-in amplifier Phase shift and amplitude of the oscillating cantilever are determined with a lock-in amplifier integrated into the AFM electronics, which compares the cantilever oscillation to the cantilever excitation (the reference wave). The output of the lock-in, X and Y, can readily be transformed to phase ϕ and amplitude A by transforming cartesian coordinates to radial coordinates:

$$A = \sqrt{X^2 + Y^2}, \tag{2.17}$$

and

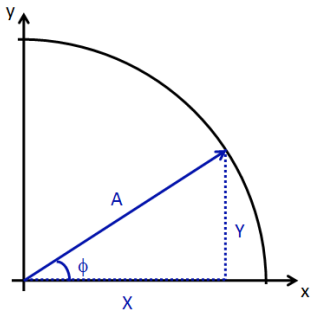

Figure 2.12 The output of the lock-in amplifier, X and Y, can readily be transformed to phase ϕ and amplitude A by transforming cartesian coordinates to radial coordinates.

$$\phi = \arctan \frac{Y}{X}. \tag{2.18}$$

Calibrations

Piezoelectric scanning tubes The voltage applied to the piezoelectric tubes corresponds to a certain distance the piezo expands or contracts (this relation is linear for small voltages). The displacement of the piezoelectric tubes for scanning the sample in all three spatial dimensions has to be recalibrated every 3–6 months. For this purpose special calibration samples are employed which feature a periodic pattern (cylinders, cubes or lines) of known dimensions. The WSxM software (Nanotec Electronica, Spain) permits to account for the nonlinearity which becomes important when the piezo is operated close to the maximum voltage.

Photodiode sensitivity The response of the photodiode has to be calibrated to convert the voltage signal it returns to the distance the cantilever is deflected (in nanometres). The most common way for this calibration is to take a force vs distance curve on a hard, clean surface. Once tip and sample are in contact, the cantilever deflection equals the vertical piezo displacement if the sample does not deform. The vertical piezo displacement yields a reliable distance measurement since it is calibrated every 3–6 months (see above). The voltage difference between the top two segments and the bottom two segments of the photodiode is, in a good approximation, linear with deflection, so that the calibration constant (in V/nm) is given by the slope of the linear region where the tip contacts the surface.

A drawback of this calibration method is that the tip-sample contact will change the tip (size and/or geometry), especially if the tip is sharp and if it is the first contact. Depending on the experiment in question, a tip change might be detrimental for the further course of the experiment. Tip damage can be minimized by limiting the normal force the tip exerts on the sample to small values (few nanonewtons). In some cases the calibration can even be performed at the end of the experiment. If non-invasiveness is indispensible or the surface is soft or deformable, other non-contact calibration methods can be used.[101,102]

Cantilever force constant Equation 2.16 is used by the manufacturers to give an approximate value of the force constant, assuming standard values for E, b, h and L for all cantilevers in one batch. However, due to the fabrication process the cantilever thickness is subject to significant fluctuations, and whenever an accurate value of the force constant is required, a calibration must be carried out for each cantilever. Due to the difficulty to determine the cantilever thickness (electron microscopy

is too time-consuming to be carried out routinely on every cantilever), other calibration methods exist which do not require the knowledge of the cantilever's thickness. The two most common methods for the calibration of the cantilever force constant are:

Sader's method For rectangular cantilevers, Sader and coworkers have developed a calibration method which gives good accuracy of the force constant and which is easy to apply experimentally, since only readily determinable quantities are required: the cantilever's resonance frequency ω_{res} and quality factor Q in fluid (typically air) as well as its length L and width b:[103]

$$k = \frac{\pi}{16}\rho b^2 L \omega_{\mathrm{res}}^2 Q \Gamma''\left(\omega_{\mathrm{res}}\right). \tag{2.19}$$

ρ is the density of the fluid and $\Gamma''\left(\omega_{\mathrm{res}}\right)$ the imaginary component of the hydrodynamic function in the fluid. This expression is valid if $Q \gg 1$, which is typically satisfied when a cantilever oscillates in air. Cantilever width and length are easily determined by optical microscopy, and resonance frequency and quality factor are obtained from the amplitude vs frequency spectrum. Sader's method has been used for cantilever force constant calibration throughout this thesis.

Thermal cantilever movement According to the equipartition theorem, the mean value of the potential energy $\frac{1}{2}k\langle x\rangle^2$ equals the thermal energy $\frac{1}{2}k_{\mathrm{B}}T$, so that the cantilever force constant k is given by

$$k = \frac{k_{\mathrm{B}}T}{\langle x^2 \rangle}. \tag{2.20}$$

T is the absolute temperature (in Kelvin), k_{B} the Boltzmann constant and $\langle x^2 \rangle$ the mean displacement due to thermal noise. Although this calibration method is valid for any cantilever geometry, it is limited by the sensitivity of the device. The thermal motion of stiff cantilevers ($k \approx 40\ \mathrm{Nm}^{-1}$) is low and can only be detected if noise due to other sources (e.g. electrical noise) is sufficiently low.

Chapter 3

Nanogeometry Matters: Unexpected Decrease of Capillary Adhesion Forces with Increasing Relative Humidity[1]

"In all affairs it's a healthy thing now and then
to hang a question mark on the things you have long taken for granted."
— Bertrand Russell, 1872–1970

Generally, adhesion between two objects with hydrodphilic surfaces increases with humidity, due to an increasing liquid meniscus. This sticking effect between hydrophilic surfaces occurring at increasing relative humidity is a day life phenomenon with uncountable implications. Here experimental evidence is presented for a counterintuitive monotonous

[1]The essential parts of this chapter have been published as *Nanogeometry Matters: Unexpected Decrease of Capillary Adhesion Forces with Increasing Relative Humidity* by Mariana Köber, Enrique Sahagún, Pedro García-Mochales, Fernando Briones, Monica Luna and Juan José Sáenz in Small **6** 2725 (2010).

decrease of the capillary adhesion forces between hydrophilic surfaces with increasing relative humidity for the whole humidity range. It is shown that this unexpected result is related to the actual shape of the asperity at the nanometer scale: a model based on macroscopic thermodynamics predicts this decrease in the adhesion force for a sharp object ended in an almost flat nanometer sized apex, in full agreement with experiments. This anomalous decrease is due to the fact that a significant growth of the liquid meniscus formed at the contact region with increasing humidity is hindered for this geometry. These results are relevant in the analysis of the dynamical behavior of nanomenisci. They could also have an outstanding value in technological applications since the undesirable sticking effect between surfaces occurring at increasing relative humidity could be avoided by controlling the shape of the surface asperities at the nanometric scale.

3.1 Capillary forces

Moisture alters the cohesion among particles in powders and the adhesion of particles to surfaces. The principal reason for this effect is the formation of a liquid meniscus at the contact region between the two objects in question. The attractive force caused by such a liquid meniscus is called "capillary force". For hydrophilic surfaces it predominates over other surface forces under ambient conditions.[9]

Understanding the way humidity influences adhesion is of fundamental importance when treating with powders,[104] friction related problems[105] and phenomena driven by hydrophobic interactions and has, thus, implications in important industries such as the pharmaceutical, food and materials industry. Given the fact that macroscopic tribology phenomena involve the contact of a multitude of micro- and nanometric asperities,[10,105,106]

a profound understanding of the capillary forces occurring at one single asperity contact is of fundamental importance. This is particularly relevant in the rapidly growing field of nanobiotechnology where capillary induced adhesion and friction become a serious tribological concern. Nature provides uncountable examples of adhesion mechanisms involving capillary forces and is the source of bioinspired strategies in the design of adhesive systems. An especially inspiring example, which has aroused a large scientific interest over the last decade, is the adhesion and friction of the gecko pad during climbing and traversing ceilings.[107] Gecko pads exhibit a fine structure of hierarchically arranged fibers which, by means of van der Waals and capillary forces, enable the geckos to adhere to surfaces with great efficiency (Figure 3.1).[107–112] A current technological effort is focused on the biomimetic design of surfaces with controlled adhesive and lubricant properties.[111] Some applications, however, require low adhesion forces. Nanodevices, for example, may lose reliability because of capillary induced adhesion and friction, which can even prevent them from working.[11] In any case, tailoring the adhesion at the nanoscale presents a technological challenge.

On account of this, an extensive study of the capillary forces acting at micro- and nanoasperity contacts has been performed over the last years.[6,9–22] Despite all these efforts, the underlying principles of capillary adhesion are not fully understood even for a single nanoscale contact. The reason lies in the large number of parameters involved in the process. Nanoasperity shape, contact radius, length, contact angles, relative humidity, etc. are known to play a crucial role in determining the adhesion properties. It is extremely difficult to control all the relevant parameters at the nanoscale level and, in practice, quantitative results are not fully reproducible.

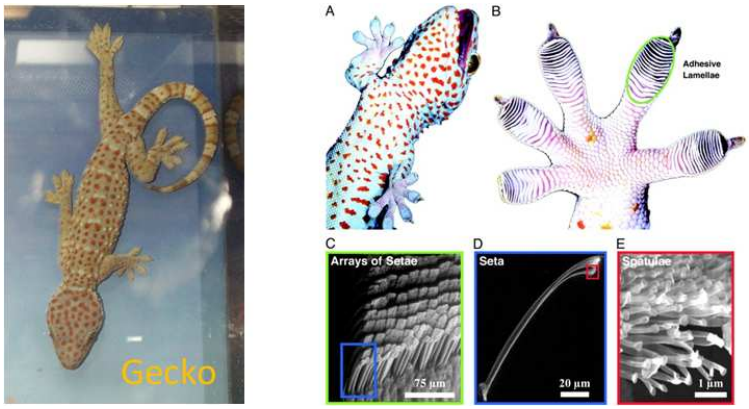

Figure 3.1 The gecko is a prominent example demonstrating that adhesion is strongly influenced by the micro- and nanostructure of surfaces. Micro- and nanostructures at the toes allow the gecko to adhere to almost any surface topography. The hierarchical structure consists of lamellae (400–600 µm long), setae (2–10 µm wide, 100 µm long), and spatulae (200 nm wide and long). In this way the surface area is so high that geckos stick to the ceiling merely through van der Waals forces. Reprinted with permission from [113]. ©2005 National Academy of Sciences, U.S.A.

In spite of the diversity of the experimentally obtained adhesion force vs relative humidity (RH) curves, all the reported curves have one feature in common: starting from low relative humidity values the adhesion force increases with humidity. In fact, the curves show either a monotonous increase[9,17] or a maximum at a certain humidity value[15,16,19,114] (see Reference [9] for a recent review on experimental and theoretical studies on the humidity dependence of the adhesion force). This trend reflects the expected natural behavior we are familiar with, for example when playing with sand: with dry sand we cannot build a sandcastle; a certain amount of water, though, makes the particles stick to each other (Figure 3.2).

However, here the inverse effect is reported: even in dry environments (at low humidity values) the adhesion force decreases with increasing relative humidity. Starting from 0% RH, a monotonous decrease of

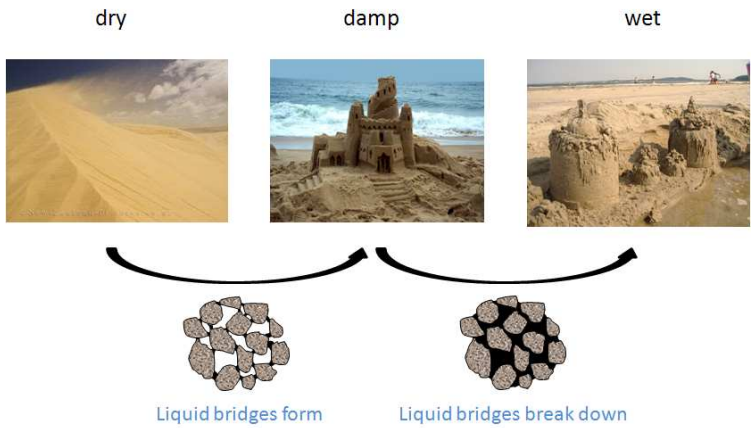

Figure 3.2 The sand castle reflects the expected dependence of adhesion on moisture: When a certain amount of water is added to the sand grains, adhesion increases due to the formation of liquid necks between the sand grains, and a sand castle can be built. When even more water is added, liquid necks break down and the sand castle collapses.

the adhesion force is observed for the entire RH range between two hydrophilic materials. These experimental results were obtained through AFM measurements, using sharp monocrystalline silicon tips of very small tip apex (< 10 nm) and applying very low normal loads (< 10 nN). A theoretical model using continuum theory and the formation of minimum energy water necks demonstrates that the decrease in the adhesion force between hydrophilic surfaces is related to the object's geometry: only a sharp object finished in an almost flat (truncated) nanometer sized apex gives rise to this behavior.

3.2 Unexpected observation: capillary adhesion forces may decrease with relative humidity

Experiments were carried out with a commercial AFM (Nanotec Electrónica, Cervantes FullMode AFM System, http://www.nanotec.es/) enclosed in a humidity control chamber. Adhesion force vs RH curves were obtained by measuring force vs distance curves (Section 2.5), from which adhesion forces were extracted,[115] while increasing the relative humidity slowly from 0 to 100% (see the Experimental Section for details on the measurement procedure). Adhesion forces were measured between a flat muscovite mica substrate cleaved prior to the experiment and monocrystalline silicon as well as silicon nitride tips (for a detailed description of the tips employed see the Experimental Section). These materials are predominantly hydrophilic (the contact angles for mica, Si_3N_4 and $Si0_2$ are 0°, 3°and 20°, respectively[116,117]).

Curve progressions of adhesion force vs RH curves obtained with different AFM tips may differ considerably from one another, but we can clearly distinguish two trends when employing monocrystalline silicon tips: decreasing curves and curves displaying a maximum. From the results of a series of experiments we can conclude that this different adhesion force behavior is clearly related to the tip dimensions. When the tip radius exceeds 15 nm we find the common behavior reported in the literature[9,15,18,118] with a maximum at a certain humidity value. However, whenever tip apex dimensions are maintained sufficiently small (radius < 10 nm), the adhesion force either decreases in the whole humidity range or decreases until it reaches a constant value. Examples of this monotonous decrease are shown in Figure 3.3a. The Scanning Electron Microscopy (SEM) images of the tips taken after each experiment show (Figure 3.3b) that - within the resolution - in all three cases the nominal

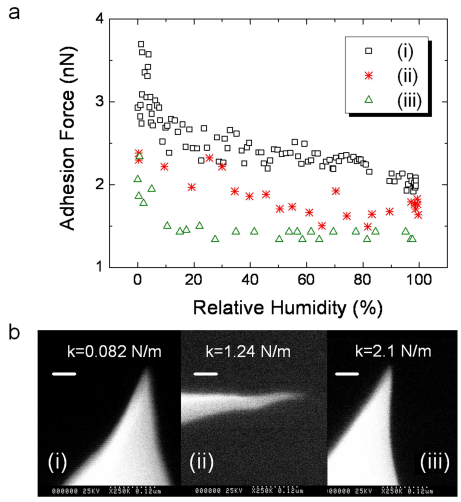

Figure 3.3 Decreasing Adhesion Force: (a) Adhesion force measured between a sharp Si tip and a flat mica sample as function of the relative humidity, for three different tips. Nominal tip radii are < 7 nm for (i) and (iii) and about 2 nm for (ii). The experiments were performed with a maximum applied load of 10 nN. (b) SEM images showing the three tips after they had been used to measure the adhesion force (the scale bars represent 60 nm). Within the resolution the nominal tip radius is preserved after the experiment in all three experiments.

tip radius is preserved (see also Figure 3.8). This preservation is achieved by means of controlling the maximum applied normal load after the tip-sample contact, thus ensuring that the tip would hardly impress on the surface. For the data shown in Figure 3.3 the maximum normal force exerted on the cantilever was less than 10 nN.

If, on the contrary, the maximum normal load reach tens of nanonewtons during the measurement of the force vs distance curves, the tip dimensions are not preserved and the force vs RH curves show a maximum at a certain humidity value. In Figure 3.4a (experiment (i)) an example is shown where an initially sharp monocrystalline Si tip was used to measure the adhesion force on mica allowing high applied loads (50 nN). The SEM

image (Figure 3.4b, (i)) taken after the experiment had been performed shows a truncated tip with a radius of 20 nm. In previous works where tips were used for scanning at a load of 30 nN the tips show the same truncated shapes.[22] In addition to the SEM evidence, larger values of the adhesion force indicate larger tip radii.[119]

When silicon nitride tips with larger initial radius (15 nm nominal) were employed, the maximum behavior was always observed. Experiment (ii) in Figure 3.4a is an example (the normal force was not limited). The general trend - the occurrence of a maximum - is the same as for curve (i), although, both position and width of that maximum differ for the different tips. After the experiment the tip radius is 25 nm (SEM image 3.4b, (ii)).

A special experiment is presented in Figure 3.4a (iii) which further exemplifies the key role of the tip apex dimensions in the capillary adhesion force. In this particular case, an occasional accident happened in the middle of the experiment which caused a significant increase of the monocrystalline Si tip radius and therewith a dramatic change in the curve progression. At the beginning of the experiment (starting from low RH) the monocrystalline Si tip radius was small (nominal tip radius $<$ 7 nm) and the normal load applied was limited to 18 nN. At some point during the experiment (RH $\approx$ 65%) a power outage led to the crashing of the tip against the sample which resulted in a cleavage of the tip apex. SEM inspection after the completion of the experiment revealed a tip radius of 18 nm. Hence, in this experiment tip apex size is small for the humidity range between 0 and 65% and larger from 65% on. Both behavior and magnitude of the adhesive force correspond to these different tip dimensions: at low humidities the trend is similar to that for a tip of small radius and for RH $>$ 65% the curve shows the decline of a broad maximum, the behavior which is typical for large tip radii.

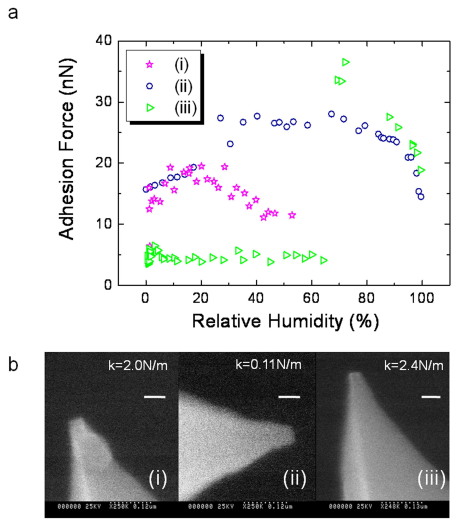

Figure 3.4 Common Maximum Behavior: (a) Adhesion force vs relative humidity curves for three different tips on a flat mica surface. (i): initially sharp Si tip (nominal radius < 7 nm), normal force limited to 50 nN. (ii): Si_3N_4 tip of 15 nm nominal tip radius, no normal load limitations. (iii): special case with initially sharp tip and normal force limited to 18 nN; at about RH 65% the tip crashed against the sample (the load remained 18 nN). (b) SEM images showing the three tips after they had been used to measure the adhesion force. The scale bars represent 60 nm. The SEM images of the tips taken after the experiments show larger tip radii than the nominal values.

Throughout a series of 17 experiments tip size and shape at the nanoscale have shown to have a dramatic effect on the humidity dependence of the capillary force. Although the tip shape was known to influence the capillary forces[17] (increasing with humidity for conical tips or having a broad maximum for quasi-spherical apexes), to our knowledge, the monotonous decreasing observed in these experiments has not been reported. In order to understand the origin of the different adhesion force behaviors, the group of Prof. J. J. Sáenz (Universidad Autónoma de Madrid) developed a theoretical model which determines the capillary

adhesion forces between a flat hydrophilic surface and a sharp hydrophilic object of different apex shapes and sizes.

3.3 Theory predicts decreasing capillary forces for truncated nanocones

A simplified model based on equilibrium thermodynamics is considered[2], similar to the one used to describe the hysteresis associated to the formation and rupture of liquid bridges.[6] As in previous theoretical work,[6,9,10,14,17,22] the approach is based on macroscopic continuum theory.[10] This approach is valid even when dimensions fall below a few nanometres, which is the range where the discrete molecular nature of the liquid could be relevant.[120] Molecular Dynamics[121,122] and Monte Carlo[123,124] simulation studies have also been carried out, confirming the validity of the continuum theory.

After condensation, the liquid meniscus is assumed to have a radius of curvature R_c. For a given tip shape and tip-sample distance D, the pendular ring geometry is fixed by R_c and the tip and sample contact angles. The equilibrium properties of the water meniscus depend on the "excess" grand potential[125,126] given by the sum of surface, $\Delta\Omega_S{=}\gamma\ (S_{LV} - S_{LT} - S_{LS})$, and volume, $\Delta\Omega_V{=}\gamma\ V(\frac{RT}{\gamma v_m}\ln(\frac{1}{H}))$, contributions, where the S's are the surface areas of the liquid-vapor (LV), liquid-sample (LS) and liquid-tip (LT), and $\gamma \equiv \gamma_{LV}$ is the liquid-vapor surface energy. Tips and samples used in the experiments are predominantly hydrophilic. To simplify matters, in the model zero contact angles are considered (for hydrophilic surfaces, an increase in the contact angle leads to a decrease in the adhesion force magnitude but does not

[2]The theoretical analysis was performed by Dr. E. Sahagún, Dr. P. García-Mochales and Prof. J. J. Sáenz (Universidad Autónoma de Madrid).

change the adhesion force vs humidity curve behavior[22]). Qualitative changes in the dependence of adhesion with relative humidity are expected at much larger contact angles or for hydrophobic surfaces.[110] υ_{m} is the molar volume, $R = 8.31\mathrm{Jmol}^{-1}\mathrm{K}^{-1}$ and H is the relative humidity. At a given temperature, the condensation energy is proportional to the meniscus volume V and inversely proportional to (the absolute value of) the Kelvin radius r_{K}. For D smaller than a critical distance, the grand potential as a function of R_{c} presents a local minimum ($\Delta\Omega_0(D, R_{\mathrm{eq}}(D))$) which corresponds to a meniscus of radius $R_{\mathrm{c}} = R_{\mathrm{eq}}$ in equilibrium. Assuming that the meniscus evolves in thermodynamic equilibrium, the pulling-off force is simply given by $F = -\frac{\partial\Delta\Omega_0}{\partial D}$.

To study a large family of tip shapes the tip was modeled as a cone with an ellipsoidal cap end, the cone side being tangential to the ellipsoid (see Figure 3.5a). The tip shape is then characterized by three parameters: the cone angle (ν), the transverse (horizontal) semi axis of the apex (a) and the apex form factor b/a, where b is the conjugate (vertical) semi axis. Varying b/a it is possible to study the force vs RH curves for a continuum family of tip apex shapes: prolate ($b/a > 1$), conventional spherical apex ($b/a = 1$), oblate ($b/a < 1$) and quasi-truncated blunt ($b/a \ll 1$) tips. Changing the cone angle ν, the effect the tip sharpness has on the capillary force can be analyzed. Naturally, the capillary force also depends on the initial tip-sample distance D.[17,114]

Calculated capillary adhesion force vs RH are depicted in Figure 3.5 for different tip shapes and sizes at a fixed tip-sample distance $D =$ 0.2 nm (mimicking the presence of an adsorbed water layer on the sample). Figures 3.5b and 3.5c reproduce the expected results for conical and spherical tips. For a relative small aspect ratio ($b/a = 0.2$, Figure 3.5d) they resemble those obtained with the paraboloidal model discussed in Reference [17]. The adhesion curve still shows a maximum but its behavior

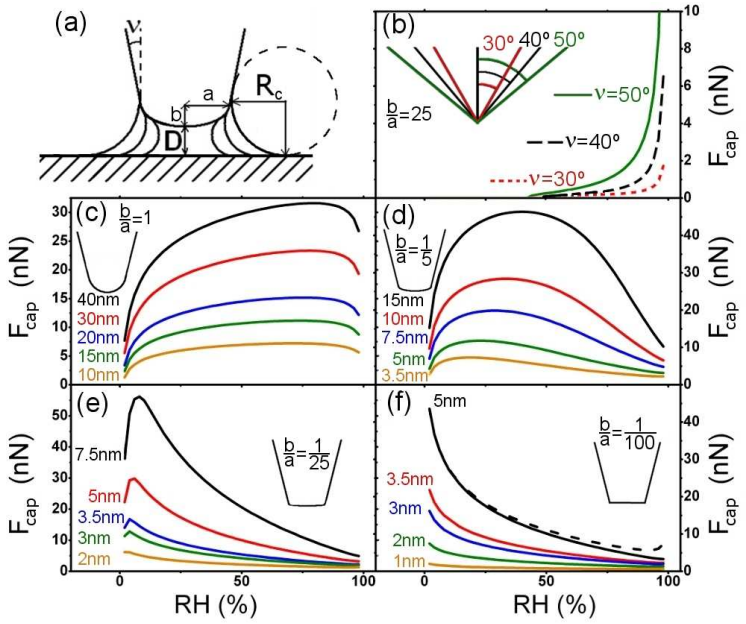

Figure 3.5 Capillary Forces vs Geometry: (a) Sketch of the modeled tip geometry and water meniscus (b-f) Calculated adhesion force vs humidity for different values of the tip apex form factor b/a (= 25, 1, 0.2, 0.04 and 0.01, respectively) and the ellipsoid transverse semi axis a. In (b) the results for a quasi conical tip are shown ($b/a = 25$, $a = 5$ nm) for different aperture angles. In (c-f) solid lines are results for tips with $\nu = 10°$ and different a values. In (f) the dashed line corresponds to a quasi-truncated tip with $a = 5$ nm and $\nu = 30°$.

has changed in comparison with the spherical model: the general shape of the curve changes with the tip size and the maximum position decreases with decreasing size. In contrast, sharp oblate and blunt tips with $a \gg b$ (Figures 3.5e and 3.5f) show a completely different behavior. If the tip is relatively large ($a \approx 8$ nm) and not too flat ($b/a \approx 0.04$), the force curve still presents a maximum at very low humidity. In the limit of an almost truncated tip ($b/a \leq 0.01$, $a \leq 5$ nm), the force decreases for the whole RH range. Very close to saturation, the force may increase again with RH,

showing a minimum for large cone opening angles ($\nu \geq 25°$), as shown in Figure 3.5f.

3.4 Discussion

In order to understand the different behaviors, note that the equilibrium force is approximately given by the Laplace pressure acting on the cross-sectional area defined by the radius r_2 of the contact line at the top of the meniscus,

$$F \approx P_{\text{Laplace}} \pi r_2^2 \tag{3.1a}$$

$$\approx \gamma \left(\frac{RT}{\gamma \upsilon_{\text{m}}} \ln \left(\frac{1}{H} \right) \right) \pi r_2^2. \tag{3.1b}$$

Except for some limiting cases, the results are well described by this simple expression. In this formula the behavior of the force versus RH can be seen as a result of two competing effects. As RH increases, the Laplace pressure decreases (independently of the objects' geometry) while the meniscus cross section increases (this increase does depend on geometry). As a simple example, one can consider a conical tip shape where r_2 increases linearly with r_{K}. The capillary force on the cone grows then linearly with r_{K} (diverges as the inverse of $\ln(1/H)$) in agreement with Figure 3.5b. Since the curvature of the meniscus is approximately given by the Kelvin radius, the cross-section and, subsequently, the behavior of the adhesion with RH, mainly depends on the shape of the tip at the scale determined by the Kelvin radius. This is illustrated in Figure 3.6 where both r_2 and F versus RH are plotted for a relatively blunt tip (with $b/a = 1/25$ and $a = 5$ nm). At low RH, i.e. small r_{K}, the Kelvin radius

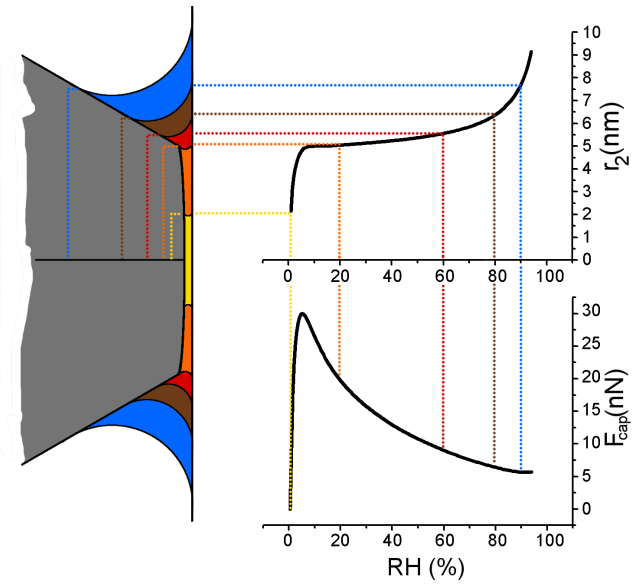

Figure 3.6 Meniscus blockade: Calculated radius r_2 of the contact line at the top of the meniscus and capillary adhesion force F_{cap} versus RH for a relatively blunt tip ($b/a = 1/25$, $a = 5$ nm).

fits beneath the flat end of the tip apex and r_2 grows very rapidly with r_{K} (with RH). Near the edge of the flat area apex, where the tip surface curvature is high, an increase in the meniscus curvature radius (i.e. r_{K}) does not lead to an appreciable increase in r_2 (keeping a zero contact angle with the tip surface). Hence the adhesion force decreases. We could then say that the meniscus growth is blocked (pinned) by the high curvature regions of the tip apex. Figure 3.7 shows an illustration of the liquid neck growth for a truncated nanocone and a nanosphere. Since r_{K} is in the nanometer range, the adhesion curves depend on the details of the tip shape at the nanoscale.

The presented model does not mimic exactly any real tip-sample system since real tips, in general, exhibit a more complex structure than

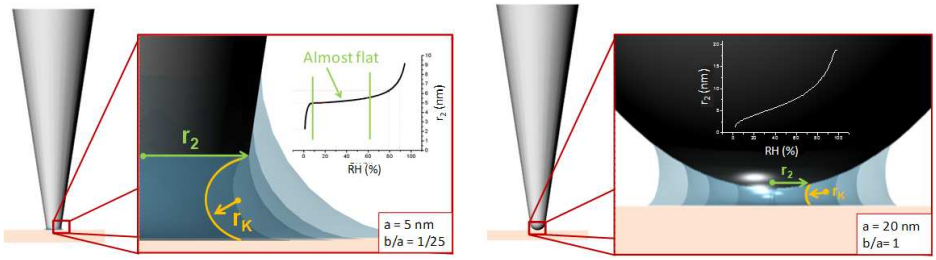

Figure 3.7 Liquid neck growth for different tip geometries. Left: Truncated nanocone for which the meniscus-tip contact area stays constant in a wide relative humidity range (for a wide range of increasing Kelvin radii). Right: For a nanosphere the meniscus-tip contact area increases with increasing relative humidity (increasing Kelvin radius).

the one modeled here. Possible effects of the RH dependence on the adsorption isotherm of the water film[114] or the possibility of an "ice-like" structure of the adsorbed water were not considered.[18] Nonetheless the model shows that the different behaviors observed in the experiment can be understood by simply taking into account the tip shape at the nanoscale. Note the quantitative agreement between theory and experiment assuming a transverse radius of $a \approx 1$ nm and a form factor of $b/a \approx 0.01$ (a can be > 1 nm if the contact angle > 0) which would imply an ultrasharp tip with an almost atomically flat apex!

This is consistent with the fact that the sharp tips with apex radii below 10 nm (and even below 5 nm, see also the Transmission Electron Microscopy (TEM) images in Figure 3.8) used in these experiments are made of monocrystalline Si, since these tips present a nearly perfectly flat fracture surface at the tip apex after entering into first contact with the stiff mica sample[127]. Considering both the theoretical discussion and the experimental adhesion curves, tips with "large" apex (radius > 15 nm) should present some residual curvature (very small b) in the form of atomic terraces or dislocations causing a deviation from the almost perfectly flat

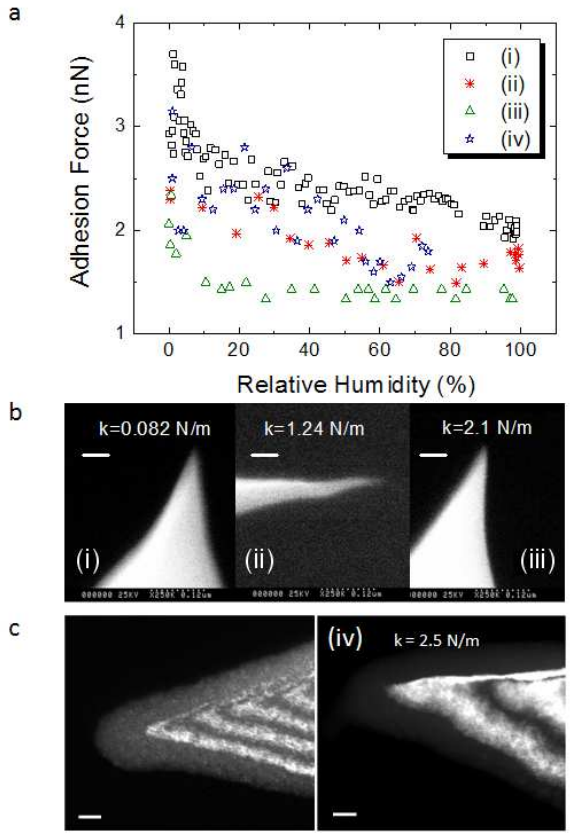

Figure 3.8 TEM images show that a small tip apex (radius ≤ 5 nm) is preserved: (a) Adhesion force as function of the relative humidity for the four sharp Si tips (i)-(iv). Nominal tip radii are 7 nm for (i), (iii) and (iv), and 2 nm for (ii). (b) SEM images showing the three tips (i)-(iii) after they had been used to measure the adhesion force with flat mica surfaces (the scale bars represent 60 nm), (c) Dark field Transmission Electron Microscopy (TEM) images of an unused Si tip (left) and a Si tip after it had been used in experiment labelled (iv) has been performed (the scale bars represent 10 nm). The interference fringes in the dark field TEM images are caused by the thickness variation of the tip. The tip is covered by a layer of amorphous material consisting of the native silicon oxide layer (2 nm thick) and amorphous carbon which is deposited during the irradiation with the electron beam.

Figure 3.9 The tip presents a flat fracture surface after entering into first contact with the stiff mica sample.

surface (notice that for a radius of 15 nm and $b/a \approx 1/15$, b is of the order of 1 nm). These differences in the apex geometry, leading to very different behaviors of the adhesion force, cannot be easily determined from standard SEM images.

3.5 Conclusions

Experimental evidence for a counterintuitive decrease of the capillary force between hydrophilic surfaces with increasing relative humidity was obtained. In concordance with the experimental results, in the theoretical simulation the tip apex shape was identified as the origin of different adhesion force vs RH behaviors. The monotonous decrease of the adhesion force is only found for a sharp truncated object with a narrow contact region. The large variety of meniscus force behaviors found for different tip shapes emphasizes the importance of geometry in the capillary phenomena at the nanometer scale. The results imply that for a correct interpretation of AFM adhesion maps the tip size and shape have to be taken into account - hydrophilic samples do not necessarily yield a capillary force increase with increasing moisture. Our results are also relevant in the analysis of the dynamical behavior of nanomenisci.[128] Furthermore, our findings could be of relevance in technological applications since the undesirable sticking effect between surfaces occurring at increasing relative humidity could be

avoided by controlling the shape of the surface asperities at the nanometric scale.

3.6 Experimental Details

Experimental procedure: The adhesion force between tip and sample was determined by performing force vs distance curves (Section 2.5). After the tip entered in contact with the sample, the force that has to be applied to detach the tip from the surface equals the adhesion force (see Figure 2.8). The RH was increased by introducing humid air (flowing dry nitrogen (N_2) through ultrapure Milli-Q water (Millipore)) at a controlled flow rate into the chamber. The AFM cantilever's vertical velocity was as low as $10\,\mathrm{nm\,s^{-1}}$ during all the force curves, thus ensuring that the meniscus would be in equilibrium with the surrounding atmosphere and, furthermore, minimizing tip damage due to the impact. The cantilevers' force constant k was determined by Sader's method (Section 2.7).[103] Both tip and sample surface were electrically grounded during all experiments in order to minimize the effect of electrostatic forces.

AFM tips: The tips employed in the experiments shown here are: "Nanosensors PointProbe Plus" for experiments (i), (iii) of Figure 3.3 and (i), (iii) of Figure 3.4 (monocrystalline Si, tip radius < 7 nm, cone angle at tip apex $\approx 10°$; http://www.nanosensors.com/PointProbe_Plus.pdf); "Nanosensors SuperSharpSilicon" for experiment (ii) of Figure 3.3 (monocrystalline Si, radius ≈ 2 nm, cone angle $< 7^o$ for the last 150 nm; http://www.nanosensors.com/SuperSharpSilicon.pdf) and Olympus OMCL-RC800PSA-W type (Si_3N_4, nominal tip radius 15 nm; http://probe.olympus-global.com/en/en/specnitrideE.html) for experiment (ii) of Figure 3.4.

Acknowledgments

The essential parts of this chapter have been published as *Nanogeometry Matters: Unexpected Decrease of Capillary Adhesion Forces with Increasing Relative Humidity* by Mariana Köber, Enrique Sahagún, Pedro García-Mochales, Fernando Briones, Monica Luna and Juan José Sáenz in Small **6** 2725 (2010). Simulations were performed by Enrique Sahagún under the supervision of Juan José Sáenz (Departamento de Física de la Materia Condensada, Universidad Autónoma de Madrid). AFM, SEM and TEM measurements were conducted by myself, in part together with Mónica Luna. All authors contributed to the discussion of the results as well as to the writing of the manuscript.

Chapter 4

Adhesion Hysteresis in Dynamic Atomic Force Microscopy[1]

In dynamic AFM, the power that is dissipated between tip and sample offers supplementary material information that is still not fully understood. In each cycle of the cantilever oscillation, tip and sample interact, and, depending on the physicochemical sample properties, a certain amount of energy is dissipated in this interaction process. Consequently, the energy that is dissipated in the tip-sample interaction process is related to physicochemical sample properties. However, this dissipated energy is not an experimentally accessible quantity, but rather the dissipated power, which presents a time-average over several oscillation cycles. To be able to translate images of dissipated power into maps of physicochemical sample properties, first the dissipated power has to be related to the energy that is dissipated in the tip-sample interaction process. In a second step, this dissipated energy can be related to material properties. Generally, it is assumed that dissipation occurs equally in all oscillation cycles, and

[1]Parts of this chapter have been published as *Adhesion hysteresis in dynamic atomic force microscopy* by Mariana Köber, Enrique Sahagún, Martina Fuss, Fernando Briones, Monica Luna and Juan José Sáenz in physica status solidi (RRL) **2** 138 (2008).

the experimentally obtained dissipated power is directly converted into dissipated energy per cycle. However, our results suggest that this is not always true, but the cantilever motion may actually be irregular, and dissipation may occur only every some oscillation cycles.

The objective of the proposed work was to study dissipation due to adhesion hysteresis and to analyze how the measurable dissipated power relates to the dissipated energy. The effects of adhesion hysteresis in the dissipation curves measured in dynamic AFM are discussed. Numerical simulations show that hysteresis in the interaction forces modify the cantilever dynamics, leading to different power dissipation behavior in the two operating regimes, the repulsive and the attractive regime (the two operating regimes in AM-AFM are described on page 38). The concordance of experimental results with the numerical simulations suggests that only in the RR, where tip-sample contacts occur in every oscillation cycle, power dissipation is proportional to the energy dissipated in the tip-sample interaction process. In this case, the dissipated power can be directly related to physicochemical sample properties. In the AR, however, the tip contacts the sample surface only occasionally. Then, the dissipated power is not directly related to physicochemical sample properties, but rather also depends on the cantilever dynamics. Experimental work is in progress to determine tip-sample contacts in both regimes and relate them to the dissipated power.

4.1 Adhesion hysteresis and dissipation

Most real processes that occur when two materials are brought together involve energy dissipation or hysteretic phenomena. The understanding of the microscopic mechanisms of energy dissipation is then fundamentally relevant for a large variety of basic and applied problems (adhesion,

contact formation, friction, wear) and has motivated extensive theoretical and experimental efforts over a century.[105] The development of the Atomic Force Microscopy (AFM) opened a new way to study energy losses at nanometer scales. Phase shift variations, measured by recording the phase lag of the cantilever oscillation relative to the driving signal, are directly linked to energy dissipation processes.[81,129,130] At fixed feedback amplitude, phase contrast images are proportional to power dissipation maps which can potentially be translated into maps of substrate physicochemical properties.[131]

AM-AFM, also known as tapping mode AFM (see page 37), has been shown to be a powerful tool for qualitative compositional/dissipation mapping. AM-AFM dissipation spectroscopy, based on the analysis of the dissipated power as a function of the cantilever oscillation amplitude, has been proposed as a way to identify specific energy-dissipation processes behind the compositional contrast.[131] However, despite of these important advances, the actual link between power dissipation and nanoscale surface properties is not well understood.

As a general approach, power dissipation in AM-AFM is naturally considered synonymous of the energy that is dissipated per cycle. This energy can then be directly related to specific tip-surface interaction processes, number of chemical bonds, etc. In striking contrast to this apparently natural argument, our results suggest that in the attractive regime (AR) the time-averaged dissipated power is not proportional to the instantaneous energy that is dissipated in the tip-sample interaction of each oscillation cycle, due to the fact that the tip enters into contact with the sample surface only occasionally (e.g. every n oscillations). In consequence, in the AR, measured maps of dissipated power cannot be directly related to dissipative interaction properties of the tip-sample system, but also reflect the dynamics of the cantilever. However, in the

repulsive regime (RR) the tip contacts the surface in every cycle, and the dissipated power can be directly related to specific tip-sample interactions.

Dynamic dissipation experiments performed on mica samples (at 0% RH) are presented together with numerical calculations based on a point mass model. An excellent agreement between experiments and calculations is obtained assuming a simple mechanical hysteresis model where the energy dissipated in every contact process is a fixed quantity. Due to the bistable motion of the cantilever,[132,133] the dissipated power strongly depends on the AFM operating regime. While in the RR power dissipation is constant (as expected from a fixed energy loss per cycle), in the AR both experimental and calculated power dissipation strongly depend on the cantilever oscillation amplitude.

4.2 Measuring dissipation

A set of experiments was performed at room temperature with a commercial AFM (Nanotec Electrónica, Spain) kept in an atmosphere of $(2 \pm 0.5\%)$ RH in order to avoid dissipation due to capillary condensation. In all experiments, we employed a mica substrate which was cleaved immediately prior to the experiment, and monocrystalline silicon cantilevers (Nanosensors, Nanoworld, Switzerland) driven at the free resonance frequency. The dissipated power P_{dis} is related to the oscillation amplitude (A) and the phase shift between the driving excitation and its response (ϕ) through[81]

$$P_{\mathrm{dis}} = \frac{kA_0^2\pi\nu_0}{Q}\left(\frac{A}{A_0}\sin\phi - \left(\frac{A}{A_0}\right)^2\right), \tag{4.1}$$

A_0 being the free oscillation amplitude of the cantilever and Q the quality factor. In order to obtain P_{dis}, Q must be determined close enough to the surface to include film damping effects.[81] Therefore an oscillation spectrum (Figure 4.1) was recorded at a tip-sample distance D_{ts} which was just a few nanometres larger than the free oscillation amplitude. Q was determined by a Lorenztian fit to the experimental data. Dynamic dissipation curves were obtained approaching the oscillating cantilever towards the surface while recording both A and ϕ (see Section 2.5, page 44) for different free oscillation amplitudes A_0. Results for a representative experiment are shown in Figure 4.2a and c.

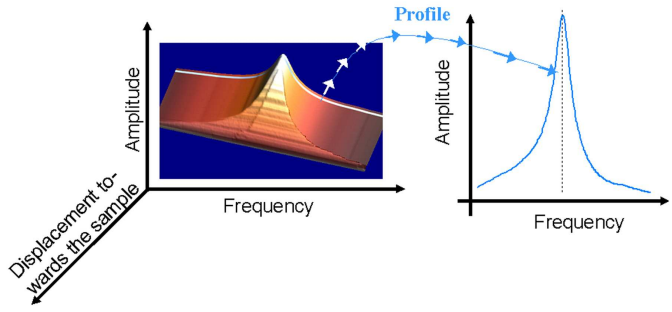

Figure 4.1 Amplitude vs frequency curves are recorded while the tip approaches the surface (left). The quality factor Q is obtained from a Lorentzian fit close to the region in which the amplitude starts to diminish due to tip-sample interactions (right).

4.3 Modeling dissipation due to adhesion hysteresis

The group of Prof. J. J. Sáenz[2] (Universidad Autónoma de Madrid) developed a theoretical model which takes into account a hysteretic

[2]The theoretical analysis was performed by Dr. E. Sahagún, Dr. P. García-Mochales and Prof. J. J. Sáenz.

adhesion force. In this model, dissipation only originates from tip-sample contacts (through adhesion hysteresis), and the energy that is dissipated in one contact event is constant. Consequently, the dissipated power is directly related to the number of tip-sample contacts.

The dynamics of the tip-cantilever ensemble is approximately described as a driven anharmonic oscillator including the cantilever elastic response, the hydrodynamic damping with the medium and the tip-sample interaction forces F_{ts} (including both van der Waals and Dejarguin-Muller-Toporov[56] contact forces as discussed in Reference [71]). Dissipation is taken into account by adding a hysteretic force F_{hys}. Molecular Dynamics (MD) simulations[7] predicted hysteresis in the force versus tip-sample distance related to intrinsic mechanical instabilities at the atomic scale. As the tip approaches the sample, the interaction is essentially given by the attractive conservative forces (i.e. $F_{\mathrm{hys}} = 0$). Just before contact, there is a sudden jump of the interaction force resulting in the formation of an atomic scale connective neck and, as the tip retracts, there is an additional adhesive force which drops approximately linear in a few interatomic distances (D_0). It is worth noticing that this behaviour associated with the formation and rupture of a solid neck[7] is similar to the one discussed in the context of capillary induced liquid bridges.[6] As a simple approach, they consider a linear adhesive force (when the tip retracts)

$$F_{\mathrm{hys}} = \frac{2\Delta E}{D_0^2}\,(D_{\mathrm{ts}} - D_0) \qquad \text{for } D_{\mathrm{ts}} < D_0, \tag{4.2}$$

where D_{ts} is the tip-sample distance and ΔE the energy dissipated in the contact process. The simulations were performed by solving numerically the cantilever's equation of motion at fixed excitation frequency ν_0. The values for k, ν_0 and Q were set to the values determined in the

experiments. The tip radius R was set to 15 nm, the Hamaker constant for mica to 10^{-20} J and the effective Young Modulus to 54 GPa. The tip-sample contact takes place when D_{ts} is of the order of an intermolecular distance a_0 (0.25 nm). Following typical MD results,[7] D_0 was assumed to be $3a_0$ while ΔE was a fit parameter to experimental results.

4.4 Comparing experimental and calculated dissipation curves

Previous works[134] had focused on the effect of adhesion hysteresis in the Frequency Modulation Atomic Force Microscopy (FM-AFM), where the resonance frequency shift is recorded while keeping $\phi = 90°$. Assuming that the dissipation takes place in each oscillation cycle,[134] P_{dis} would be proportional to the frequency. In AM-AFM we would then have $P_{\mathrm{dis}} = \Delta E \nu_0$ which, for fixed ΔE and ν_0, would be constant and independent of the amplitude. However, when tip-sample contacts do not occur in every oscillation cycle, but only occasionally[135], P_{dis} is lower than the expected value.

Figure 4.2 shows the phase and the dissipated power, experimentally measured (a and c) and theoretically calculated (b and d), versus the normalized amplitude, as the tip approaches the surface. A remarkable agreement between experiments and calculations is obtained with this model with a fixed energy dissipated per contact $\Delta E = 56$ eV. It should be stressed that this agreement does not specifically support the simple linear force model for F_{hys}. Any arbitrary F_{hys}, acting whenever the tip-sample distance reaches a minimum, would produce similar results.

For high free oscillation amplitudes ($A_0 > 40$ nm for this experiment), as the tip approaches the sample the system enters abruptly into the

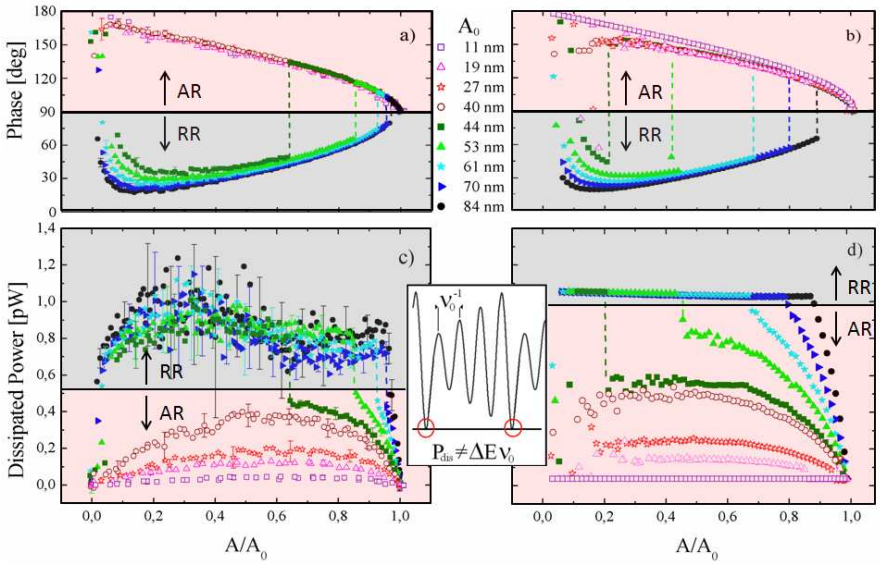

Figure 4.2 Experimental (a) and calculated (b) phase shift and experimental (c) and theoretical (d) dissipated power versus the oscillation amplitude obtained as the tip-sample distance is reduced. Symbols correspond to different free oscillation amplitudes A_0 ranging from 11 to 84 nm. The cantilever showed a free resonance frequency of $\nu_0 = 85.3$ kHz and a spring constant of $k = 3.2\,\mathrm{Nm}^{-1}$, determined following Sader's method (Section 2.7).[103] Q was determined to 160. Experimental data were smoothed (average over 10 data points) and the standard deviation is shown. The time evolution of the tip-sample distance in the attractive regime is sketched in the central inset.

repulsive regime (RR, $\phi < 90°$). Whenever the system is in the RR, the dissipated power is constant: $P_{\mathrm{dis}} = \Delta E \nu_0$. Simulation results show that, here, the tip contacts the sample in every oscillation cycle. Starting from lower A_0 ($A_0 < 44$ nm for this experiment), the system remains in the attractive regime (AR, $\phi > 90°$) while the sample approaches the tip. For these A_0 the dissipated power shows a maximum which increases for increasing A_0. A detailed analysis of the simulated results reveals that these variations in the dissipated power are directly related to variations in the number of tip-sample contacts. In the AR, after the contact process,

the cantilever, which has lost energy, will not reach the same amplitude as before the contact, and the tip may not hit the sample surface during the next swings (sketched in the inset in Figure 4.2). The power dissipation is then lower than expected. Similar qualitative phenomena have been predicted for capillary interactions.[6]

Although this model is rather simple, since it does not take into account other possible mechanisms that can give rise to hysteresis in an adhesion/decohesion process, such as plastic or viscoelastic deformations, it describes the experimentally observed behavior well. Naturally, other materials or experimental conditions might require the consideration of further parameters.

4.5 Experimental investigations on the correlation of tip-sample contacts and dissipated power

Work is in progress to analyze the cantilever motion in AR and RR experimentally, and determine whether the tip contacts the surface every now and then in the AR. Experiments consisted in approaching the oscillating cantilever towards the surface while recording amplitude and phase vs tip-sample distance for dissipation analysis (as above) and, simultaneously, high resolution normal cantilever deflection vs tip-sample distance in order to determine contact events. The correlation of dissipation and tip-sample contacts as a function of tip-sample distance was then analyzed.

Experimental conditions were as before (Section 4.2): experiments were performed with a commercial AFM (Nanotec Electrónica, Spain) at room temperature (23 °C). The mica substrate was cleaved immediately prior to the experiment. In order to simplify the interpretation of the data

by minimizing effects due to water adsorption or capillary condensation, the RH was kept constant at $(2 \pm 0.5)\%$ during the experiment, achieved by a gentle flow of N_2 into a glass chamber which isolated the AFM from the surroundings. The cantilever was approached to the surface until tip and sample entered steady contact (approach velocities were 10–40 $\mathrm{nm\,s^{-1}}$). In order to be able to access the low frequency movement of the cantilever in steady contact, the normal cantilever deflection was obtained before it went through the AFM electronics, and it was only low-pass filtered with a cutoff frequency of 1 MHz. Force vs distance curves were recorded with oscilloscopes that allowed a high resolution (LeCroy Waverunner 6050 and Tektronix DPO 7054).

The occurrence of tip-sample contacts was determined by analyzing each cantilever oscillation in real space (from the high resolution normal cantilever deflection vs tip-sample distance curves, Figure 4.3a-c). The sample surface was defined by the contact line, which is a straight line in case tip and sample do not deform.[93] Here, we define the position of the mica surface through a linear regression to the contact line (see Figure 4.3a-c). There are two effects that introduce some uncertainty in determining the sample surface that the tip actually "sees" while approaching: First, even at relative humidities as low as $\leq 5\%$ a uniform water layer adsorbed on the hygroscopic mica surface has been observed.[136] Consequently, in the AR the tip could contact an adsorbed water layer every now and then, without actually touching the mica surface. Second, the first atomic mica layers might get somewhat compressed upon constant tip-sample contact (at the contact line). Thus, before steady contact the mica surface might have been actually somewhat closer to the tip than the contact line suggests. To minimize this second effect, the linear regression is performed only to the data range that is close to the point where tip and sample enter into steady contact (hardly impressing on the surface, data marked yellow in Figure 4.3a-c).

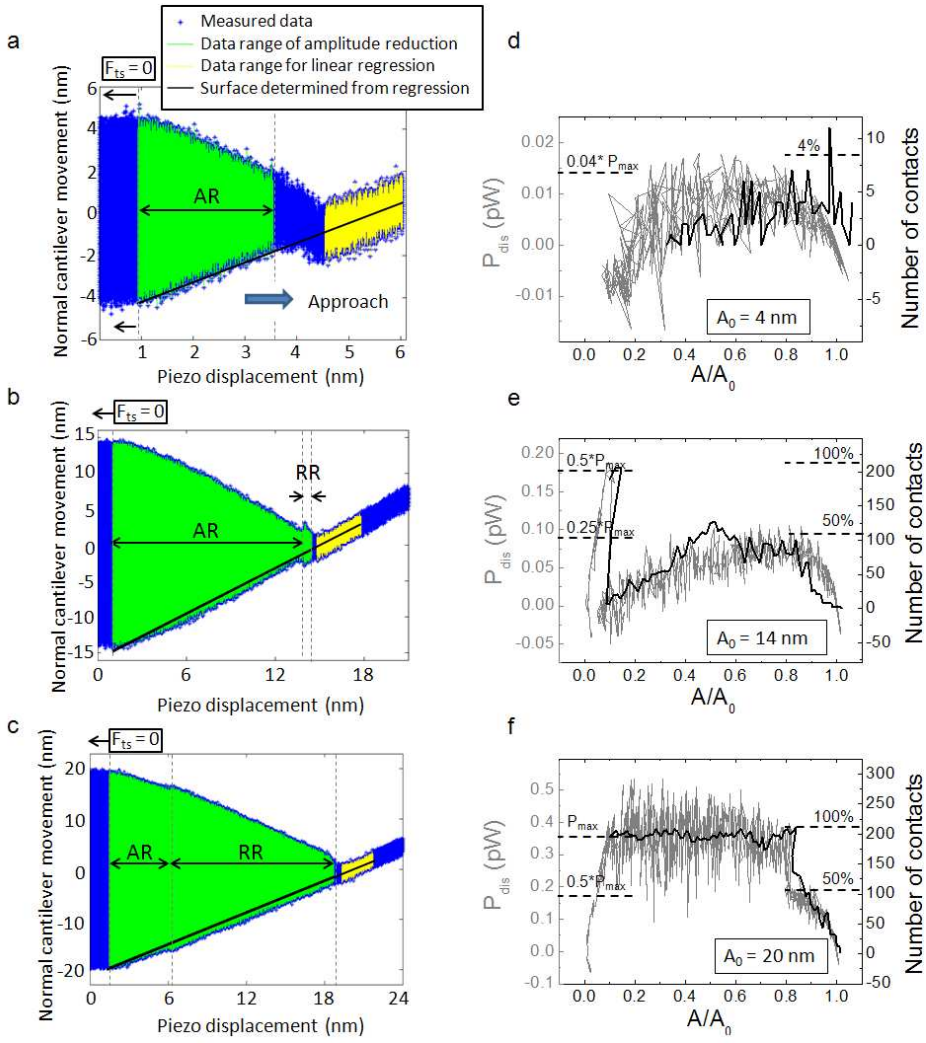

Figure 4.3 a-c: Cantilever oscillation while tip and sample were approached, for different free oscillation amplitudes. The sample surface (black line) was determined by performing a linear fit to the contact line (data range marked yellow). The curves were recorded with an oscilloscope with 8 bit resolution and a sampling rate of 1 MS/s (LeCroy Waverunner 6050, France). The cantilever showed a free resonance frequency of 67.2 kHz and a force constant of 1.39 Nm^{-1}. In this case, each oscillation is defined by 15 points. d-f: Number of contacts in 212 oscillations (black line, right scale) determined from the curves shown in a-c, and corresponding dissipated power calculated from amplitude and phase curves (grey line, left scale).

Upon surface definition, amplitude and oscillation minima were determined for each oscillation cycle, and it was checked whether the oscillation minimum was above or below the determined surface line (black line in Figure 4.3a-c). In order to relate the time-averaged dissipated power to the number of tip-sample contacts occurring in the respective time window, the contact events were counted in this time interval, and the number of contacts was assigned to the mean amplitude value for this interval. On the other hand, the dissipated power has been calculated from the amplitude and phase curves, as explained above (Section 4.2). Both dissipated power and number of contacts are graphed vs the normalized amplitude in Figure 4.3d-f.

These first evaluations seem to confirm our suppositions: Dissipated power and number of contacts follow the same trend. When the free oscillation amplitude is low (Figure 4.3d, A_0 =4 nm, the RR is not reached), the number of contacts is very low (tip-sample contact occurs only in about 1 of every 50 oscillation cycles at the maximum). When the free oscillation amplitude is increased (Figure 4.3e, A_0 =14 nm), the RR is reached just before the tip enters in steady contact with the sample. In the AR, the sample is contacted at most about once every two cycles, while in the RR tip-sample contacts occur almost every oscillation cycle. For higher free oscillation amplitudes (Figure 4.3f, A_0 =20 nm), the number of contacts increases in the AR and reaches its maximum value in the RR, where contact occurs in almost each oscillation cycle (100%).

However, further evaluation of the data has shown that the recorded data is very noisy. In particular, the determined fluctuation of the minimum tip-sample distance of each oscillation cycle (Figure 4.4a-c) is very high, namely 2 nm. Even for experiments in which each oscillation cycle was defined by 70 points, the same variation in the minimum tip-sample distance was obtained. Moreover, far from the surface, where

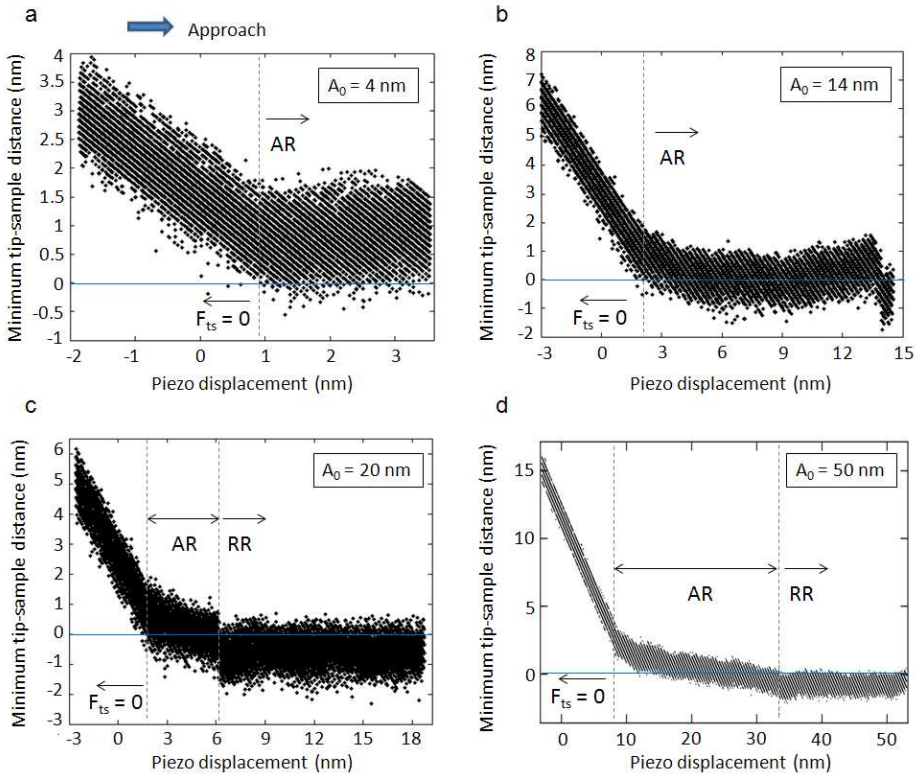

Figure 4.4 a-c: Minimum tip-sample distance corresponding to the curves shown in Figure 4.3a-c. d: Minimum tip-sample distance determined from the cantilever oscillation measured with the home-built low noise AFM of Prof. Jarvis' group (Conway Institute, University College Dublin). This curve was recorded with a Tektronix DPO 7054 oscilloscope with 8 bit resolution and a sampling rate of 5 MS/s. In this case, the cantilever showed a free resonance frequency of 69.6 kHz (so each oscillation is defined by 70 points) and a force constant of 1.5 Nm^{-1}.

tip-sample interaction forces are insignificant, the cantilever oscillation would be expected to be more regular. However, data dispersion is almost equally high at all tip-sample distances. Consequently, we suppose that the observed data dispersion is actually related to noise. The reduction

of this noise is necessary in order to determine the actual tip position in each oscillation cycle.

In order to compare our data obtained with a commercial AFM to that obtained with a home-made instrument specifically designed for low noise, we contacted with Prof. S. Jarvis (Conway Institute, University College Dublin) who is renowned for her expertise in this field. In her laboratory, we repeated the same experiments, using the same materials and conditions as before.[3] However, the minimum tip-sample distance shows the same noise of about 2 nm, even at distances far from the surface (Figure 4.4d).

The origin of this noise becomes clear when we analyze the thermal noise spectrum (Figure 4.5): While the noise level in the frequency band around the cantilever resonance frequency is low, namely 70 fm/$\sqrt{\text{Hz}}$,[4] the low-frequency $1/f$ noise is relatively high, which is affecting the deflection curves. Generally, in AFM operation, filters are applied that only let the frequency band around the cantilever resonance frequency pass. Here, however, we are interested in conserving the low frequency component of the cantilever movement, which allows us to determine the sample surface position. The low-frequency $1/f$ noise is due to flicker noise caused by the photodiode and optical beam deflection electronics, and cannot be reduced without modifying the instrument. From the evaluation and discussion of these data with Prof. S. Jarvis' group we conclude that a possibility to overcome this problem is to split the deflection signal into several versions and process them separately. One version is low-pass filtered to provide the cantilever deflection on the mica surface, and a second version is notch-filtered around the cantilever resonance frequency,

[3] Experiments were performed with T. Brosnan, and with the advice of Prof. Jarvis and Dr. J. Kilpatrick.

[4] The typical value for commercial AFMs is about 800 fm/$\sqrt{\text{Hz}}$.

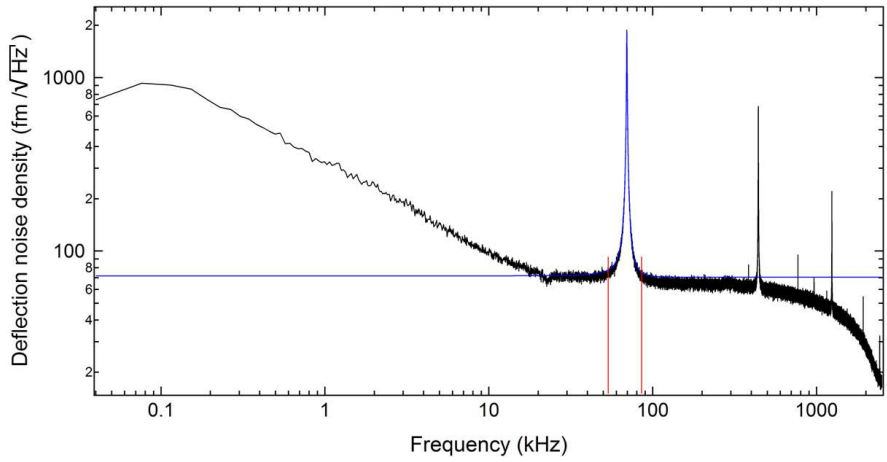

Figure 4.5 Thermal noise spectrum corresponding to Figure 4.4d, measured with the home-built low noise AFM from Prof. S. Jarvis' group (Conway Institute, University College Dublin).

giving high-resolution cantilever oscillation data. Both versions can be time-correlated and combined to form the complete curve.

4.6 Imaging evidence of occasional tip-sample contacts in the attractive range

In the experiment presented earlier (Figure 4.3), a water island was observed after the first force vs distance curve had been performed at 2% RH. The AM-AFM topographic images of that area (Figure 4.6a-d), taken in AR operation, show a flat island of 7 Å in height. Successive images showed the receding island that finally disappeared after about 90 min. No islands were created in following force vs distance curves at this low RH of 2%. We conclude that water (which still remained on the tip after reducing the RH from ambient humidity to 2%) has been

transfered to the mica sample, while water condensation is not favorable at this low RH.

Interestingly, next to the water island of approximately 100 nm in lateral extension, small water "drops" (with lateral extensions of less than 20 nm) can be observed throughout the scanned area. This suggests that occasional tip-sample contacts occur, through which water is transferred from the principal water island throughout the whole scanned area. Consequently, these images indicate that occasional tip-sample contacts occur in the AR, at least when some water is present. Other experimental results that have been reported previously also suggest occasional tip-sample contacts in the AR under the presence of water.[137]

4.7 Conclusions

The agreement of experimental and theoretical power dissipation curves suggests that adhesion hysteresis modifies the cantilever dynamics, leading to different dynamic dissipation behaviors in the two operating regimes, the repulsive and the attractive regime: in the repulsive regime, the tip touches the surface in every oscillation cycle and, consequently, the dissipated power can be easily related to the energy that is dissipated per cycle. Thus, in the RR, the dissipated power can be directly related to physicochemical sample properties. However, in the attractive regime, tip-sample contacts occur only occasionally. As a consequence, power dissipation maps cannot be directly related to physicochemical sample properties. Experimental work is in progress to determine tip-sample contacts in both regimes and relate them to the dissipated power.

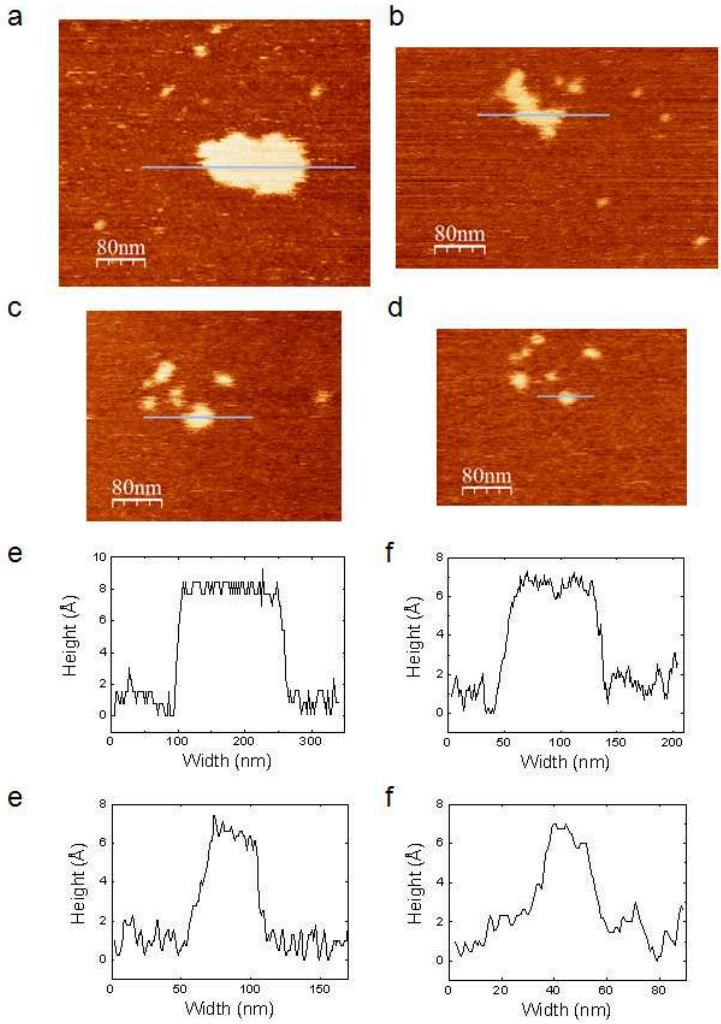

Figure 4.6 Topography images of a flat water island adsorbed on mica after the first force vs distance curve was performed at 2% RH (with an approach velocity of 22 nms^{-1}, a tip-sample contact time of 0.4 s, and a maximal force exerted by the cantilever on the surface of 8 nN). The island was imaged by AM-AFM in the AR, with a free oscillation amplitude of $A_0 = 4$ nm and a setpoint of $A/A_0 = 0.74$ (a) and $A/A_0 = 0.88$ (b) and (c). Images were taken successively 20 min (a), 55 min (b), 61 min (c) and 70 min (d) after the first force vs distance curve. Profiles of the water islands are shown in (e)-(h).

Author contributions and acknowledgments

Parts of this chapter have been published as *Adhesion hysteresis in dynamic atomic force microscopy* by Mariana Köber, Enrique Sahagún, Martina Fuss, Fernando Briones, Monica Luna and Juan José Sáenz in physica status solidi (RRL) **2** 138 (2008). Simulations were performed by Enrique Sahagún under the supervision of Juan José Sáenz (Departamento de Física de la Materia Condensada, Universidad Autónoma de Madrid). AFM experiments were performed by myself, with the assistance of Mónica Luna. All authors participated in the discussions as well as in the writing of the manuscript. Part of the experiments of Section 4.5 was performed in the group of Suzi Jarvis (Conway Institute, University College Dublin), together with Tim Brosnan, and with the advice of Suzi Jarvis and Jason Kilpatrick. We also acknowledge fruitful discussions with Luis Colchero on noise and filtering.

Part II

Transient Magnetic Birefringence for studying interactions of magnetic nanoparticles in physiological media

Chapter 5

Transient Magnetic Birefringence in Magnetic Nanoparticle Suspensions

The second part of this thesis deals with the implementation of the experimental setup to measure Transient Magnetic Birefringence (TMB) (Chapter 6), and with its application to dense media (Chapter 7) and molecular recognition studies (Chapter 8). TMB is based on the birefringence that is induced magnetically in a suspension of magnetic nanoparticles (MNPs). In this chapter, an introduction to colloidal nanoparticles (NPs) is given (Section 5.1), and the underlying physics of TMB is outlined to understand the MNP response to the magnetic field and the resulting birefringence (Section 5.2).

5.1 Nanoparticles for biomedical applications

Nanoparticles are particles with a size (the length of at least one dimension) of 1–100 nm. They may exhibit size-related properties that differ significantly from those observed in bulk material. NPs can be

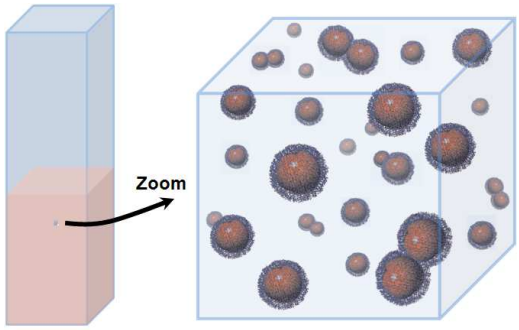

Figure 5.1 Illustration of colloidal nanoparticles (NPs). For most applications in life sciences and biomedicine, NPs are suspended in water or biocompatible (buffer) solutions, in which the NPs undergo Brownian motion.

made of many different materials, such as polymers, lipids, dendrimers and inorganic materials. For inorganic NPs, composition, size and shape are of utmost importance for the physical properties of the particle. Most inorganic NPs are made of semiconductor (*quantum dots*), metallic (especially Au and Ag) and magnetic materials.

Colloidal nanoparticles Nanoparticles can either be suspended in fluids, attached to a surface or integrated into bulk material. For most applications in life sciences and biomedicine, NPs are suspended in water or biocompatible (buffer) solutions, as illustrated in Figure 5.1. In this way, NPs can be easily introduced into the body for *in vivo* applications (e.g. drug delivery, hyperthermia, imaging and diagnosis). To use these NPs in biomedical applications, they must meet important requirements such as biocompatibility and stability in physiological media. Particle aggregates of sizes larger than 200 nm cause thrombus formation in blood vessels with serious consequences for the human body.[138] Stable suspensions of NPs can be achieved by coating the inorganic core with ligand molecules

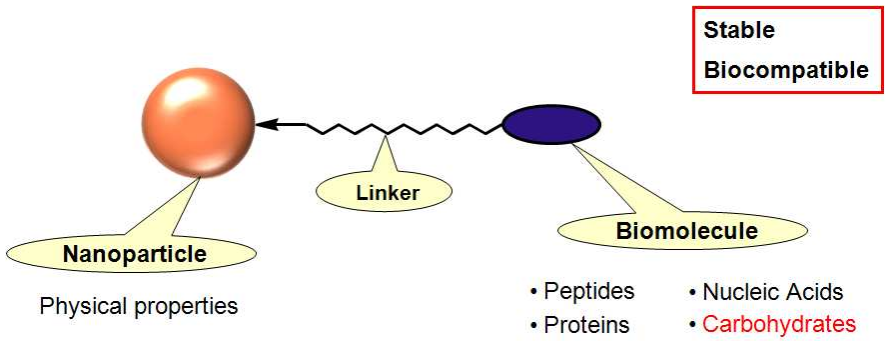

Figure 5.2 Nanoparticle functionalization. Capping ligands assure nanoparticle dispersion and prevent nanoparticle aggregation. Proper particle functionality is achieved by adding DNA, peptides, proteins and/or carbohydrates. To use these particles in medical applications, they must be biocompatible and stable in physiological media.

that balance attractive and repulsive forces through steric stabilization and/or electrostatic repulsion. We then speak of colloidal NPs.

Particle functionalization Capping ligands assure nanoparticle dispersion and prevent nanoparticle aggregation due to attractive van der Waals forces. To achieve proper particle functionality (e.g. chemical or biochemical functionality), ligands can be further modified, as illustrated in Figure 5.2. This process is called particle functionalization. The desired biochemical functionality is achieved by functionalizing the NPs with DNA, peptides, proteins and carbohydrates, for example. NPs functionalized with monosaccharides or oligosaccharides are called glyco-nanoparticles (GNPs). In this thesis, GNPs functionalized with glucose (Glc) and galactose (Gal) were used to perform lectin-carbohydrate recogniton studies (Chapter 8).

Nanoparticle interactions and aggregation Colloidal particles interact with the suspending medium and with the other particles in their surroundings. Generally, NP-NP interactions include attractive van der Waals forces, repulsive electrostatic forces and steric effects. In case the NPs are magnetic, attractive magnetic dipolar interactions occur. Furthermore, interactions can be mediated by molecular recognition.

Attractive van der Waals forces are always present and must be balanced by repulsive electrostatic forces and steric stabilization (introduced by the capping ligands) to avoid unspecific aggregation. Nevertheless, the transfer of NPs from organic solvents (in which the particles are synthesized) to water based solutions often involves the formation of some small aggregates.[139]

Under the application of a magnetic field to a suspension of magnetic nanoparticles (MNPs), particle chains may form if attractive magnetic dipolar interactions are strong enough and if the magnetic field is applied for a sufficiently long time interval. On the other hand, the application of very short magnetic field pulses (of less than one millisecond) to the suspensions of superparamagnetic nanoparticles used in our studies does not give rise to a magnetic field induced aggregation, since superparamagnetic particles only present a magnetic moment during the pulse duration, and in this time the particles do not drift far enough to join another particle in a diluted suspension.

Also molecular recognition can give rise to NP cluster formation if the bound biomolecule presents more than one binding site.

Brownian motion In the carrier liquid, colloidal NPs undergo Brownian motion, a random movement due to fluctuations in the collective bombardment of the thermally agitated solvent molecules that surround

the particles in the suspending medium. Robert Brown was the first to describe this phenomenon on pollen grains in water in 1828.[140] The theory on Brownian motion was first developed independently by Einstein[141] and Schmochulowski[142] in 1905 and 1906, and experimentally proven by Perrin in 1909.[143] The collective bombardment of thermally agitated solvent molecules exerts a random force and torque on the nanoparticles, which is why Brownian motion has a translational and a rotational component. The speed at which particles move depends on temperature, solvent viscosity and particle size.

Hydrodynamic diameter When particles diffuse in the carrier liquid, they drag along a layer of solvent molecules (*solvent layer*) which are bound to the particles through electrostatic interactions. Decisive for the particle diffusivity is what we call the hydrodynamic volume, which comprises the inorganic core, the surfactant molecules and the solvent layer attached to the particle when it moves (Figure 5.3). Studies have shown that hydrodynamic radii are strongly affected by nature and lateral extension of the capping ligands and, furthermore, systematically larger than the geometric radii for the inorganic core plus cap, since the coating layer strongly interacts with the surrounding solvent.[144] While the geometric size of the inorganic core has been extensively characterized, little is known about the hydrodynamic size of water soluble nanoparticles, even though it is an important parameter for understanding, controlling and optimizing the nanoparticles' performance in biological assays as well as the particles' migration in live cells and tissues. Since both the conformation of the surfactant molecules[145] and the hydration layer[146] affect the particles' chemical functionality, monitoring the hydrodynamic particle diameter is of major interest in a variety of applications. Furthermore, the hydrodynamic diameter indicates the aggregation state of the particles.

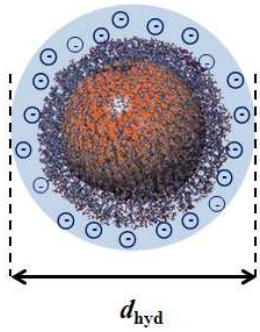

Figure 5.3 Hydrodynamic diameter. The hydrodynamic volume is decisive for the nanoparticle diffusivity. It comprises the inorganic core, the surfactant molecules and the solvent layer attached to the particle when it moves. Often the three-dimensional hydrodynamic volume of a non-spherical particle is not determined, but rather the hydrodynamic diameter d_{hyd}, which is the diameter of a hypothetic sphere which has the same diffusion properties as the particle in question.

Often the three-dimensional hydrodynamic volume of a non-spherical particle is not determined, but rather the hydrodynamic diameter d_{hyd}, which is the diameter of a hypothetic sphere which has the same diffusion properties as the particle in question.

For a spherical particle the translational diffusion constant D_{t} is given by the Stokes-Einstein equation

$$D_{\mathrm{t}} = \frac{kT}{3\pi\eta d_{\mathrm{hyd}}}, \tag{5.1}$$

and the rotational diffusion constant D_{r} by

$$D_{\mathrm{r}} = \frac{kT}{\pi\eta d_{\mathrm{hyd}}^3}, \tag{5.2}$$

where $k = 1.38{*}10^{-23}\ \mathrm{m^2 kg\,s^{-2}K^{-1}}$ is Boltzmann's constant, T the temperature of the solution and η the solvent viscosity.

5.2 Transient Magnetic Birefringence

In a suspension of MNPs optical anisotropy can be induced upon the application of a magnetic field. MNPs with shape anisotropy and/or intrinsic optical anisotropy will rotate in the solution to align with respect to the magnetic field. The necessary coupling of the field induced magnetic moment to the optical anisotropy axis of the nanoparticle depends on magnetic anisotropy, particle size, and temperature. When NPs present neither shape nor intrinsic optical anisotropy, as for example spherical magnetite NPs used in this thesis, anisotropic aggregates provoke optical anisotropy when the magnetic dipole-dipole interaction is strong enough to align the aggregate with the magnetic field. Upon removal of the magnetic field, the induced optical anisotropy disappears gradually due to the Brownian rotational motion which the particles undergo in the liquid. This decay is exponential with a characteristic relaxation time dependent on the hydrodynamic particle diameter as well as the viscosity and temperature of the solution. The transient birefringence that is induced by applying a pulsed magnetic field to a suspension containing magnetic nanoparticles is called Transient Magnetic Birefringence (TMB).

In the following the underlying physical mechanisms that are fundamental for understanding TMB are reviewed, focussing on the most

relevant issues for the experiments presented in this work. First, light scattering at NPs and the optical anisotropy induced in a suspension of NPs will be treated, followed by the discussion of the response of suspended magnetic nanoparticles to a pulsed magnetic field. Finally, the magnetically induced birefringence, where optical and magnetical properties of the NP suspension are combined, is considered.

5.2.1 Light scattering at nanoparticles and birefringence

When illuminating a suspension of nanoparticles with light, the light will be scattered, and light transmission depends mainly on particle properties such as composition, size, and shape. If the suspension is optically anisotropic, light scattering is polarization dependent. The solvent influences light transmission slightly, mainly causing depolarization. In the following, some basics of light scattering at small particles, optical anisotropy in NP suspensions and birefringence are discussed.

Mie Scattering The Mie solution to Maxwell's equation for the scattering of electro-magnetic radiation describes the scattering by particles independently of their size. It presents an analytical solution to Maxwell's equations and has to be applied when the particle diameter is similar to the scattered light wavelength, since only for particles much larger or much smaller than the light wavelength simple approximations exist. The latter, called Rayleigh approximation, is of interest when treating with visible light scattered at nanoparticles.

Rayleigh Scattering For spherical particles of sizes which are smaller than one tenth of the light wavelength, the intensity I_{Rayleigh} of unpolar-

ized light of wavelength λ and intensity I_0 scattered by a single small particle is given by[147]

$$I_{\text{Rayleigh}} = I_0 \frac{1 + cos^2\Theta}{2R^2} \left(\frac{2\pi}{\lambda}\right)^4 \left(\frac{n^2 - 1}{n^2 + 2}\right)^2 \left(\frac{d}{2}\right)^6, \tag{5.3}$$

where R is the distance to the particle, Θ is the scattering angle, n is the refractive index of the particle, and d is the particle diameter. In this thesis, helium-neon (HeNe) laser light of $\lambda = 543$ nm is used. Then, the Rayleigh approximation holds for NPs smaller than 50 nm.

Most importantly, the scattered light intensity varies as the sixth power of the particle size, so the light intensity scattered from a 50 nm particle is one million times higher than the light intensity scattered from a 5 nm particle. This makes it difficult to detect small particles in a mixture of particles with a wide size distribution, since the contribution of small particles is extremely low. On the other hand, since the scattered light intensity is inversely proportional to the fourth power of the scattering light wavelength it is better to use light of lower wavelength. By using a green HeNe laser of $\lambda = 543$ nm instead of a red HeNe laser of $\lambda = 633$ nm the scattered light intensity is almost doubled.

Rayleigh scattering is isotropic, while Mie scattering is larger in the forward direction than in the reverse direction (the greater the particle size, the more of the light is scattered in the forward direction).

Optical Anisotropy An object is optically anisotropic if the index of refraction n depends on polarization and direction of the incident light. The object can have one or two anisotropy axes and is accordingly called uniaxially or biaxially anisotropic. The optical anisotropy factor

$\chi_{\parallel} - \chi_{\perp}$ is the difference of polarizability parallel and perpendicular to the anisotropy axis.[37] Optical anisotropy can either be intrinsic, for example crystalline as in calcite, or induced externally by electric or magnetic fields, streaming, ultrasounds and stress. Crystalline anisotropy originates from an anisometric arrangement of the atoms in the crystal structure.

When NPs are suspended in an isotropic solvent, optical anisotropy is induced if

1. the scattering particles are optically anisotropic (due to their aggregation state, their form and/or crystalline anisotropy) **and**

2. the particles show a net orientation in space.

An optically anisotropic suspension of non-spherical NPs which show a net orientation in space is schematically shown in Figure 5.4a. When particles are spherical and do not show any crystalline optical anisotropy, as occurs for spherical magnetite (Fe_3O_4) and maghemite (γ-Fe_2O_3) NPs which have a cubic crystallographic structure, optical anisotropy arises when two (or more) particles form a non-sherical cluster. In the electrical field of a light beam the nanoparticles in an aggregate are oscillating dipoles interacting with each other, and the interaction strength depends on the interparticle distance.[37] The dipolar interaction in a particle chain is asymmetric with respect to the orientation of the light polarization. Thus, if the majority of the linear chains aligns with their symmetry axes in the same direction, the medium becomes optically anisotropic (Figure 5.4b).

As extensively discussed in Chapter 7, experiments demonstrate that for the spherical magnetite NPs used in this thesis, the induced optical anisotropy is mainly due to small particle aggregates (Figure 7.3 and Figure 7.6). It should be noted that clusters of more than two particles may present different arrangements of the particles in the cluster. For example, in a cluster of three particles the particles may be arranged in

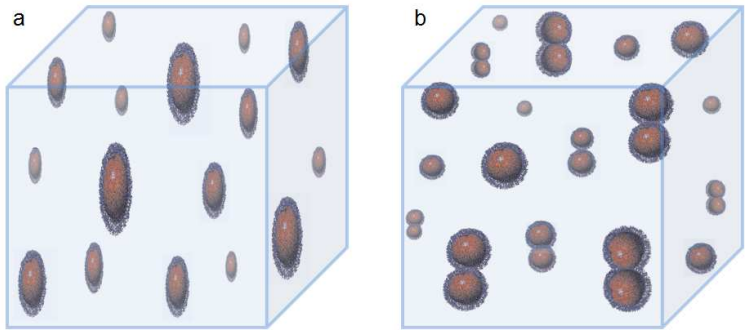

Figure 5.4 Schematic illustrating optically anisotropic nanoparticle suspensions. Suspensions of NPs showing a) form anisotropy or b) dimerization become optically anisotropic when the particles hold a net orientation in space.

a chain or in a triangle. Consequently, the optical anisotropy depends on the exact configuration of the aggregate and does not necessarily increase with the number of particles in the aggregate.

Calculations of the optical anisotropy of Fe_3O_4 NPs of 8 nm in diameter and 1 nm coating layer suspended in water have been performed by Xu and Ridler.[37] Although they only considered linear chain aggregates and no other particle arrangements in the aggregate, the results are very instructive and shall be briefly reviewed here, since NPs used in this thesis are Fe_3O_4 nanoparticles of 6–8 nm in diameter suspended in water. Figure 5.5 shows the calculated optical anisotropy factor as a function of the number of nanoparticles composing the aggregate chain (a) and as a function of interparticle distance (b). The optical anisotropy increases strongly with the number of particles until the chain contains about five particles, and then rapidly saturates as the number of particles further increases. On the other hand, the optical anisotropy factor decreases with increasing distance between the magnetic particle cores, for example due to a thick particle coating.

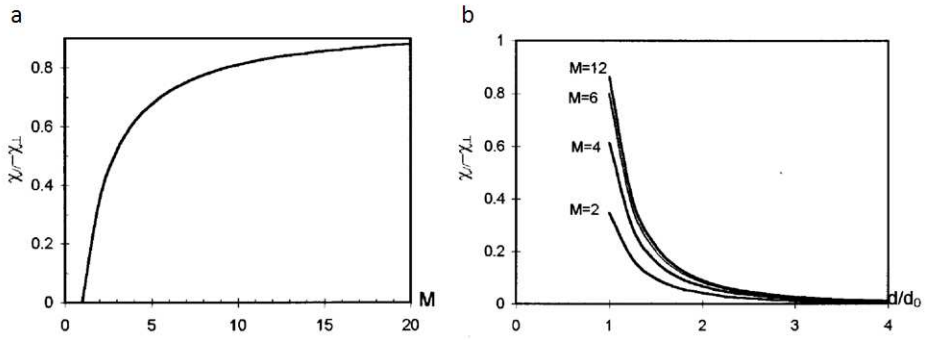

Figure 5.5 Optical anisotropy of linear chain aggregates of spherical Fe_3O_4 NPs. Shown is the calculated optical anisotropy factor for nanoparticles of 8 nm in diameter suspended in water, a) as a function of the number M of nanoparticles composing the aggregate chain (only separated by the coating layers of the particles of 1 nm each) and b) as a function of interparticle distance. Reprinted with permission from [37]. ©1997, American Institute of Physics.

The comparison of the optical anisotropy due to particle shape anisotropy and due to a linear chain of spherical NPs (Figure 5.6) shows that the optical anisotropy of dimers of spherical magnetite nanoparticles of 8 nm in diameter is much stronger than that of slightly anisometric particle spheroids of the same volume (with axis ratios of up to 1.2), provided that the particles are only separated by the coating layers of the particles of 1 nm each. Since the magnetite NPs used in this thesis show no appreciable non-sphericity (see TEM image in Figure 7.6), optical anisotropy is expected to result only from anisotropic particle clusters.

Scattering at objects presenting optical anisotropy is polarization dependent, giving rise to different phenomena: linear birefringence (different phase velocity for each polarization component), linear dichroism (different attenuation for each polarization component), circular birefringence (rotation of the polarization plane) and circular dichroism (differential absorption of left and right circularly polarized light). However, for

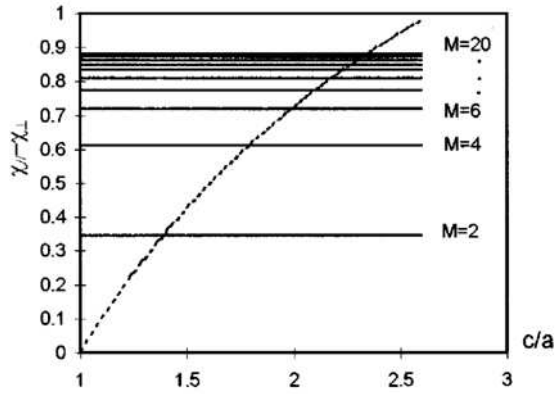

Figure 5.6 Comparison of optical anisotropy due to particle shape anisotropy and due to a linear chain of spherical NPs. Shown is the calculated optical anisotropy factor for linear chain aggregates of M spherical Fe_3O_4 particles of 8 nm in diameter (continuous lines, here $a = c$) and for spheroidal particles of the same volume, but with axis lengths a and c (dotted line, here $M = 1$). Particles, suspended in water, are separated by the coating layers of the particles of 1 nm each. Reprinted with permission from [37]. ©1997, American Institute of Physics.

particles that are small compared to the light wavelength (Rayleigh scattering), both circular dichroism and circular birefringence are small (see Reference [148], page 58). Since we are interested in the regime of Rayleigh scattering, in the following we will concentrate on linear birefringence, or short simply birefringence. Suspensions of iron oxide NPs also present a weak dichroism which is small compared to the birefringence.[32]

Birefringence When light travels through an optically uniaxially anisotropic medium, light polarized parallel to the anisotropy axis will travel at a different speed than light polarized perpendicular, $v_{\parallel} = \frac{c}{n_{\parallel}}$ and $v_{\perp} = \frac{c}{n_{\perp}}$, which results in a retardation phase shift δ between light of these two polarizations. After passing a distance L in the medium exposing the

birefringence Δn, the phase shift δ between the polarizations parallel and perpendicular to the optical axis of light of wavelength λ accounts to

$$\delta = \frac{2\pi L}{\lambda}\Delta n. \tag{5.4}$$

Birefringence is a relevant macroscopic physical property of colloidal NP suspensions, since it allows to obtain information on several particle properties (such as size, shape, interparticle interactions, response to external fields...) through an externally induced (by electric or magnetic fields, flow...) particle orientation and relaxation. Thereby, mean values of these particle properties are obtained for a sample fraction that contains a statistically relevant particle number, in contrast to other techniques (e.g. TEM or AFM) that probe rather a small fraction of particles. Moreover, birefringence probes these particle properties directly in the suspension. In this way, artifacts are excluded that would be due to a change of the particle environment (e.g. through the deposition of the particles on a copper grid or a mica sheet for subsequent TEM or AFM inspection).

In the following, the birefringence which can be induced in a suspension of magnetic nanoparticles by the application of a magnetic field will be treated. Therefore, first the response of magnetic nanoparticles to a pulsed magnetic field will be discussed.

5.2.2 Response of suspended magnetic nanoparticles to a pulsed magnetic field

The studies in this thesis were performed with colloidal superparamagnetic magnetite (Fe_3O_4) NPs. Superparamagnetic magnetite NPs are widely used in biomedical applications due to the ease of preparation, their low

toxicity and low aggregation. Below 851 K magnetite is ferrimagnetic, but magnetite nanoparticles that are smaller than a critical size are superparamagnetic.

Superparamagnetic nanoparticles Ferromagnetic and ferrimagnetic NPs become superparamagnetic when, at a given temperature, the particle size falls below a critical value. Then the magnetic moment flips directions randomly inside the particle when no external magnetic field is applied, and on a time-average the magnetic moment is zero. The average time between two flips, called Néel relaxation time τ_{N}, depends exponentially on the relation between magnetic anisotropy energy KV and thermal energy kT,

$$\tau_{\mathrm{N}} = \tau_0 \exp \frac{KV}{kT}, \tag{5.5}$$

with τ_0 being a material characteristic time span called "attempt time", typically 10^{-9}-10^{-10} s, K the nanoparticle's magnetic anisotropy energy density, V its volume (only of the magnetic core, in contrast to the hydrodynamic volume), T the temperature and k Boltzmann's constant. Consequently, the critical particle size depends on the material characteristic anisotropy energy density K. Due to the exponential dependence of the Néel relaxation time on the particle volume, Néel relaxation becomes important only for small nanoparticles. In other words, nanoparticles have to be sufficiently small for random flips to occur with significant frequency. For bulk material the Néel relaxation time amounts to years or much longer. For magnetite ($K = 3.2{*}10^4$ Jm^{-3}) nanoparticles of 10 nm in diameter, $\tau_{\mathrm{N}} \approx 10^{-7}$ s at room temperature ($T = 25°\mathrm{C}$). When

the time used to measure the magnetization of the nanoparticles is much longer, their magnetization appears to be in average zero.

The name "superparamagnetism" alludes to the parallelism with paramagnetic materials for which, likewise, a magnetic moment prevails only when a magnetic field is applied. However, for superparamagnetic materials the magnetic moment is much larger than for bulk paramagnetic materials – thus the prefix "super".

Response to a pulsed magnetic field

In TMB the colloidal MNPs are subjected to a pulsed magnetic field. In this section the particle movement in a liquid under a pulsed magnetic field is discussed. First the magnetization and particle alignment at the rising edge of the magnetic field pulse is treated, then the relaxation at the falling edge.

1. Rising edge of the magnetic field pulse

When a unidirectional magnetic field $\vec{H}$ is applied, a magnetic moment

$$\vec{m} = V\vec{M}, \tag{5.6}$$

is induced in the particles, where $\vec{M}$ is the particle magnetization given by

$$\vec{M} = \chi\vec{H}, \tag{5.7}$$

and χ is the magnetic susceptibility. A torque

$$\vec{\tau} = \vec{m} \times \vec{H}. \tag{5.8}$$

results, to align the magnetic moment in direction of the magnetic field. The magnetic energy of the particle,

$$E_{\text{mag}} = -\vec{m}\vec{H} = -mH\cos\Theta, \tag{5.9}$$

is the work of magnetic torque to realign the vector of the magnetic dipole moment, where Θ is the angle between the direction of the magnetic moment and the direction of the magnetic field.

If $T \geq \frac{KV}{k}$, the magnetic moment aligns inside the particle in direction of the magnetic field, irrespective of the material's easy axis (Néel mechanism), and without any particle rotation in the fluid. Then, the total magnetic energy of the nanoparticle is the sum of the applied field energy and the magnetic anisotropy energy,

$$E_{\text{mag}} = -\vec{m}\vec{H} - KV\left(\hat{\mathbf{m}}\hat{\mathbf{e}}\right), \tag{5.10}$$

where $\hat{\mathbf{m}}$ is the unit vector of the magnetic moment and $\hat{\mathbf{e}}$ is the unit vector of the easy axis.

Magnetic dipole-dipole interactions When nanoparticles are close to each other, magnetic dipolar interactions become important. For example, when particle aggregation exists, magnetic dipolar interactions play a key role. The interaction energy between two magnetic dipoles $\vec{m}_i$ and $\vec{m}_j$ in the point dipole approximation is given by

$$E_{\text{pot,ij}}^{\text{dip}} = \frac{\mu_0\mu_s}{4\pi r^3}\left[\left(\vec{m}_i\vec{m}_j\right) - 3\left(\vec{m}_i\hat{\mathbf{r}}\right)\left(\vec{m}_j\hat{\mathbf{r}}\right)\right], \tag{5.11}$$

where $\hat{\mathbf{r}} = \vec{r}/r$ the unit vector in direction of the line joining the centers of particles i and j, with $\vec{r} = \vec{r}_j - \vec{r}_i$. μ_0 is the magnetic permeability of vacuum.

In the energetically most favorable configuration both magnetic moments point in the same direction and are aligned with the magnetic field. The dipolar interaction depends strongly on the magnitude of the particles' magnetic moments and the interparticle distance. For magnetite NPs, the magnetic moment drops significantly when the particle size falls below 5 nm.[149] Consequently, magnetic dipolar interactions of magnetite NPs < 5 nm in diameter are very weak. Furthermore, the dependence of the dipolar interaction energy on the interparticle distance to the third power implicates that magnetic dipolar interactions are only significant for particles that are in closest proximity. For example, when the particle distance doubles, the interaction energy falls to one eigth.

The application of short pulses (of less than one millisecond in duration) to the diluted suspensions of superparamagnetic nanoparticles used in our studies has the advantage that particle aggregation due to dipolar magnetic ineractions is avoided, in contrast to the application of a constant (e.g. rotating) magnetic field. Superparamagnetic particles only present a magnetic moment during the pulse duration, and in this time the particles do not drift far enough to join another particle in a diluted suspension. On the other hand, aggregates that are due to stable chemical bonds (for example due to molecular recognition) will orient in the field to minimize their potential energy. Anisotropic NP aggregates will align with their long axes parallel to the magnetic field direction and the suspension becomes optically anisotropic.

Magnetization and degree of orientation in the suspension Due to the thermal agitation in the suspension, the particles and particle aggregates

(their magnetic moments) will not be completely aligned with the magnetic field. The orientation of the particles rather depends on the relation of their magnetic energy E_{mag} to the thermal energy kT, following a Boltzmann distribution. The magnetization M of a suspension of non-interacting superparamagnetic particles depends on the strength of the magnetic field H as[150]

$$M\left(H\right) = \frac{1}{V}\sum_{i=1}^{N} m_{\mathrm{i}} L\left(\frac{m_{\mathrm{i}} H}{kT}\right), \tag{5.12}$$

where $L(x) = \frac{1}{tanh(x)} - \frac{1}{x}$ is the Langevin function, V is the volume of the suspension, and N the number of NPs in the suspension. Under the presence of particle aggregates the magnetization deviates from this behavior. Nonetheless, at low fields the magnetization generally increases strongly with the applied magnetic field strength, and saturates at higher fields.

2. Falling edge of the magnetic field pulse

When the magnetic field drops to zero, the particles will gradually lose their net orientation in space due to the rotation that they will undergo in the fluid as a result of Brownian motion. This process is called Brownian relaxation. As a consequence, the optical anisotropy disappears.

Brownian relaxation does not only have an effect on the optical properties of the suspension, but also leads to the decay of the magnetization of the suspension. Depending on particle size, material, and temperature, Néel relaxation may also occur in the relevant measuring time (see equation (5.5)). However, since we are detecting birefringence

and not the magnetization, Néel relaxation is not relevant here, since it does not have any effect on the optical properties of the suspension (it does not implicate a rotation of the particle in the fluid but only a rotation of the magnetic moment inside the particle). The Brownian relaxation time of the magnetization of the NPs, however, has to be taken into account in the design of the magnetic field pulses (Section 6.2). In particular, the magnetic field has to decay faster than the magnetization relaxation due to Brownian motion. Otherwise the particles would not rotate freely due to Brownian motion at the falling edge, but would rather be further retained by the magnetic field until the latter completely drops to zero. The apparent rotational diffusion constant would be smaller than the real diffusion constant, and the determined hydrodynamic diameter higher than the real one.

The Brownian relaxation time of the magnetization of the NPs, τ_B, is given by

$$\tau_\mathrm{B} = \frac{1}{2D_\mathrm{r}} = \frac{\pi}{2} d_\mathrm{hyd}^3 \frac{\eta}{kT}. \tag{5.13}$$

Brownian relaxation times for the hydrodynamic particle diameter range relevant in this thesis are given in Table 5.1.

5.2.3 Transient Magnetic Birefringence in a suspension of magnetic nanoparticles

A suspension of MNPs may become optically anisotropic when an external magnetic field is applied. As mentioned earlier, this is the case if the scattering particles are anisotropic due to the presence of anisotropic

d_{hyd} [nm]	τ_{B} [μs]
7	0.1
11	0.5
14	1
25	5
53	50
114	500

Table 5.1 Brownian relaxation time of the magnetization of a NP suspension for certain hydrodynamic particle diameters.

aggregates or due to the particles' form or crystalline anisotropy. The magnetic field induces a net orientation of the particles and particle aggregates. Consequently, the resulting birefringence depends on the magnetic response of the NPs and aggregates to the magnetic field, on the optical properties of the NPs and the coupling of optical and magnetic anisotropy axes.

In this thesis the suitability to use birefringence to detect the presence of small aggregates of these particles was examined. To this end, spherical magnetite NPs were employed which do not present any significant form or crystalline anisotropy. In the following, the birefringence that is induced magnetically in a suspension of dimers (and higher order linear chain aggregates) of magnetite NPs is estimated and compared to the birefringence due to a slight non-sphericity of monomer particles.

Birefringence vs magnetic field strength Xu and Ridler have calculated the birefringence that is induced magnetically in a suspension of linear chain aggregates. When assuming that the orientation of the particle

chains follows a Boltzmann distribution, the birefringence Δn is given by[37]

$$\Delta n = \frac{1}{2} n_{\mathrm{m}} C \underbrace{\left(\chi_{\parallel} - \chi_{\perp}\right)}_{\text{optical anisotropy}} \underbrace{\left[1 - \frac{3}{x}\coth(x) + \frac{3}{x^2}\right]}_{\text{degree of orientation}}, \tag{5.14}$$

with n_{m} being the refractive index of the suspending medium of the particles, C the volume fraction of nanoparticles and $x = \frac{2mH}{kT}$. Thus, birefringence is proportional to the optical anisotropy factor $\chi_{\parallel} - \chi_{\perp}$ (see pages 105ff., and in particular Figure 5.5 and Figure 5.6). The reduced birefringence is concentration independent, $\Delta n/C$.

Figure 5.7 shows the reduced birefringence as a function of the applied magnetic field strength H, calculated for linear chain aggregates (of M particles composing the aggregate chain) of spherical magnetite nanoparticles (spheroid axis ratio $c/a = 1.0$) of 8 nm in diameter, and for single magnetite nanoparticles ($M = 1$) that are slightly non-spherical ($c/a = 1.1$) but present the same particle volume. The particles are assumed to have a surfactant coating layer of 1 nm and are suspended in water. At low fields, birefringence increases strongly with the magnetic field strength, up to approximately 50 kA/m. Birefringence saturates at magnetic field strengths > 100 kA/m. Birefringence due to single particles ($M = 1$) is very small, in contrast to birefringence due to particle dimers and higher order chain aggregates ($M > 1$). Consequently, for practically spherical magnetite nanoparticles even a very small volume fraction of dimers and small aggregates yields the dominant contribution to birefringence. It has to be taken into account that the birefringence due to aggregates of three or more particles depends on the arrangement of the NPs in the aggregate

– birefringence due to aggregates that are approximately sherical in shape is small compared to that due to linear particle chains.

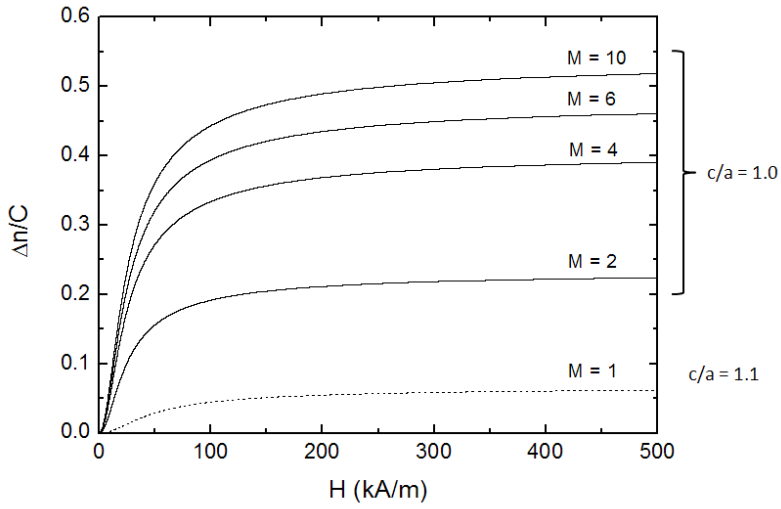

Figure 5.7 Reduced birefringence induced in a suspension of MNPs as a function of the applied field strength, calculated for single particles ($M = 1$) that are slightly non-spherical (spheroid axis ratio $c/a = 1.1$), and for linear chain aggregates ($M > 1$) of spherical particles ($c/a = 1.0$). According to the experimental conditions in this thesis, parameter values have been set to $n_{\mathrm{m}} = 1.33$, $T = 300$ K, and $m = 3.29{*}10^{-25}$ Wb/m following [37].

Birefringence relaxation Upon removal of the magnetic field, the optical anisotropy disappears gradually due to the Brownian rotational motion which the particles undergo in the liquid, and the magnetically induced birefringence decays as[151]

$$\Delta n\,(t) = \Delta n_0 \exp\left(-6D_{\mathrm{r}}t\right), \tag{5.15}$$

where n_0 is the birefringence at the time the magnetic field is switched off.

The rotational diffusion constant D_r is related to the hydrodynamic diameter d_hyd as given in equation (5.2). Thus, from the birefringence decay the hydrodynamic diameter can be determined. It should be noted that the rotational diffusion of a particle aggregate depends on the aggregate shape – a more compact (spherical) configuration leads to higher rotational diffusion constants than rather extended (chain) configurations.[152] Consequently, the derived hydrodynamic diameter of an aggregate of three particles is smaller when the particles are arranged in a triangle than when they are arranged in a linear chain.

Upon the application of a pulsed magnetic field, a transient birefringence appears that reflects the particle alignment and relaxation in response to the pulsed magnetic field. When only the particle relaxation is evaluated, the technique has also been referred to as Magnetically Induced Birefringence Relaxation (MBR).[33]

Chapter 6

Implementation of the Experimental Setup[1]

In this chapter the implementation and optimization of the experimental setup is presented.

6.1 Photoelectric measurement of weak birefringence

When linearly polarized light is sent through a birefringent sample, the light emerges with elliptical polarization. Thus, Transient Magnetic Birefringence (TMB) is detected with polarimetric measurements, sending linearly polarized light through the sample, and detecting polarization changes by help of an analyzer before collecting the transmitted light in the photodiode (Figure 6.1a). In the experimental configuration several

[1]Parts of this chapter have been published as *Transient magnetic birefringence for determining magnetic nanoparticle diameters in dense, highly light scattering media* by Mariana Köber, María Moros, Valeria Grazú, Jesus M. de la Fuente, Mónica Luna and Fernando Briones in Nanotechnology **23** 155501 (2012).

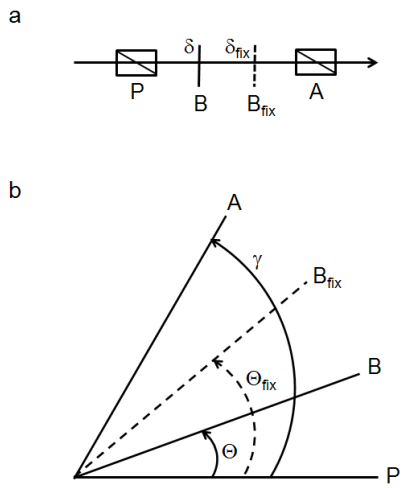

Figure 6.1 Setup for the polarimetric measurement of birefringence (a) Laser light passes through a polarizer (P), the birefringent sample (B) that introduces the phase shift δ and the analyzer (A). Optionally a further birefringent element (B_{fix}) introducing a fixed phase shift δ_{fix} can be included in between B and A. (b) Azimuth angles of the fast axes of the birefringent elements Θ and Θ_{fix} and of the vibration direction of the analyzer γ with respect to the vibration direction of the polarizer.

angles have to be adjusted to achieve optimal sensitivity, as illustrated in Figure 6.1b. To determine the optimal optical configuration with high sensitivity we have to consider the light flux φ arriving at the photodiode, following [153] and [154].

The light flux can be decomposed into two terms: the flux φ_{fix} that passes the system when no birefringent sample is present and the flux φ_{bir} that depends on the birefringence of the sample. Let φ_0 be the light flux arriving at the photodiode when the polarizers are in parallel and no sample is present. Part of φ_{fix} is due to the imperfection of crossed polarizers and to the depolarization caused by the studied substance, and can be written as $k_{\mathrm{i}}\varphi_0$, where k_{i} is the extinction coefficient. Another part

of φ_{fix} depends on the angle γ between polarizer and analyzer axes, but at this point cannot be written in a closed form since it is correlated to φ_{bir}. The total light flux is given by[153,154]

$$\varphi = \underbrace{k_{\text{i}}\varphi_0}_{\varphi_{\text{fix},1}} + \underbrace{\varphi_0 \left(\cos^2(\gamma) + \sin(2\Theta)\sin(2(\gamma-\Theta))\sin^2\left(\frac{\delta}{2}\right)\right)}_{\varphi_{\text{fix},2}+\varphi_{\text{bir}}}, \tag{6.1}$$

where Θ is the angle between the polarizer axis and the optical axis of the birefringent medium, and δ the small phase shift to be detected.

In the most common setup for detecting weak birefringences, polarizer and analyzer are crossed ($\gamma = 90°$), so that

$$\varphi = k_{\text{i}}\varphi_0 + \varphi_0 \left(\sin^2(2\Theta)\sin^2\left(\frac{\delta}{2}\right)\right).$$

In order to achieve maximum sensitivity in our setup, Θ is adjusted to 45°, and thus

$$\varphi = k_{\text{i}}\varphi_0 + \varphi_0 \sin^2\left(\frac{\delta}{2}\right) \tag{6.2}$$

$$= k_{\text{i}}\varphi_0 + \varphi_0 \left(\frac{\delta}{2}\right)^2 \text{ for small } \delta. \tag{6.3}$$

In the case treated in this thesis, the phase shift is of the order of 0.014 rad (0.8°), so that $\sin\frac{\delta}{2} \approx \frac{\delta}{2}$.

The photoelectric current detected in the photodiode is then

$$I = \underbrace{k_{\mathrm{i}} I_0 + I_{\mathrm{obs}}}_{\text{apparatus}} + \underbrace{\left(\frac{\delta}{2}\right)^2 I_0}_{\text{birefringent sample}} \tag{6.4}$$

$$= I_{\mathrm{fix}} + I_{\mathrm{bir}}, \tag{6.5}$$

where I_{obs} is the dark current of the photodiode. Thus, in the setup where the birefringent sample is positioned in between two crossed polarizers, the photoelectric current varies quadratically with δ.

By introducing a further birefringent element creating a fixed phase shift δ_{fix} into the optical path, a linear dependence of the detected current on δ is achieved if the birefringent element is chosen and positioned adequately. In this way sensitivity is increased.[153] The most common way to introduce the necessary fixed phase shift is by means of a quarter wave plate positioned in between sample and analyzer (Figure 6.1). The quarter wave plate introduces a phase shift δ_{fix} of $\pi/2$ (the electric field in direction of the wave plate's slow axis gets a $\pi/2$ delay). The resulting intensity due to birefringence is then[154,155]

$$\frac{I_{\mathrm{bir}}}{I_0} = \left(1 - \sin^2\left(2\Theta_{\mathrm{fix}}\right)\right)\left(\frac{\delta}{2}\right)^2 + \frac{1}{2}\sin\left(2\Theta_{\mathrm{fix}}\right)\delta + \frac{1}{2}\sin^2\left(2\Theta_{\mathrm{fix}}\right). \tag{6.6}$$

If the angle between the polarizer axis and the quarter wave plate's fast axis, Θ_{fix}, is chosen such that $\sin\left(2\Theta_{\mathrm{fix}}\right) \gg \delta/2$, the term quadratic in δ in equation (6.6) can be neglected and the dependence of the detected current on δ is linear,

$$I = \underbrace{\left(k_{\mathrm{i}} + \frac{1}{2}\sin^2\left(2\Theta_{\mathrm{fix}}\right)\right) I_0 + I_{\mathrm{obs}}}_{\text{apparatus}} + \underbrace{\frac{1}{2}\sin\left(2\Theta_{\mathrm{fix}}\right)\delta I_0}_{\text{birefringent sample}}. \tag{6.7}$$

If we assume that the highest phase shift δ resulting from our suspensions of magnetite NPs is 0.014, $\sin\left(2\Theta_{\mathrm{fix}}\right) \gg \delta/2$ is fulfilled for a slight rotation (a few degrees) of the quarter wave plate's fast axis out of the plane parallel to polarizer ($\Theta_{\mathrm{fix}} = 0°$) or analyzer ($\Theta_{\mathrm{fix}} = 90°$).

We implemented the experimental setup sketched in Figure 6.2. On an optical bank a HeNe laser beam of wavelength $\lambda = 543\,\mathrm{nm}$ and low power (2 mW) was aligned to pass through a polarizer, sample, quarter wave plate and analyzer and to be detected in a photodiode with low noise current to voltage converter. In an oscillograph the signal was averaged over 100 cycles to improve the signal to noise ratio. Polarizer - rotated 45° respective to the magnetic field direction - and analyzer are crossed, and the direction of the quarter wave plate's fast axis is slighly rotated out of the plane parallel to the analyzer's polarization axis, as indicated in Figure 6.2. The sample, fixed in between two non-birefringent glass slides, was submitted to magnetic field pulses produced by a Helmholtz coil.

Since the light intensity detected in the photodiode, I, depends linearly on the retardation phase shift in this experimental configuration, it follows together with equation (5.15) and equation (5.4)

$$I\left(t\right) = I_0 \exp\left(-6D_{\mathrm{r}}t\right), \tag{6.8}$$

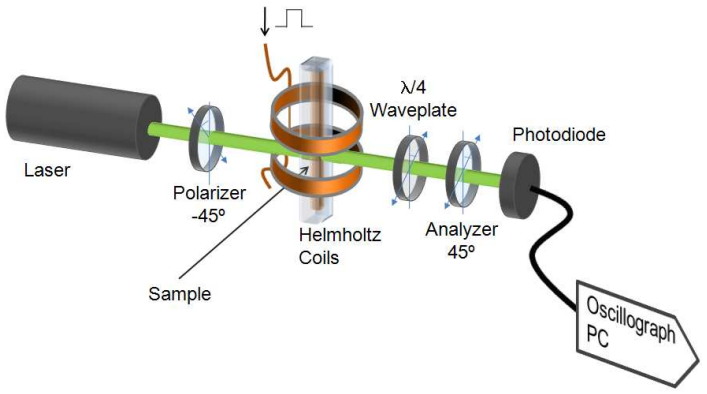

Figure 6.2 Schematic of the experimental setup for measuring Transient Magnetic Birefringence

where I_0 denotes the light intensity at the time the magnetic field is switched off. Once the rotational diffusion constant is obtained the hydrodynamic diameter of the particles can be determined with equation (5.2).

Particle size distribution When the particle size distribution cannot be neglected, the birefringence relaxation does not follow a simple exponential decay, and the detected intensity is

$$I(t) = \int I_0(d_{\mathrm{hyd}}) \exp(-6D_{\mathrm{r}}(d_{\mathrm{hyd}})\, t)\, P(d_{\mathrm{hyd}})\, \mathrm{d}d_{\mathrm{hyd}}, \tag{6.9}$$

$P(d_{\mathrm{hyd}})$ being the probability density function of the particle size distribution. The dependence of I_0 on d_{hyd} is weak compared to the dependence of P on d_{hyd}, so I_0 can be assumed to be constant in a good approximation. Since nanoparticles are generally log-normally

distributed[156] we used the log-normal distribution to approximate the particle size distribution:

$$P_{\log-\text{normal}}\left(d_{\text{hyd}};\mu,\sigma\right) = \frac{1}{d_{\text{hyd}}\sigma\sqrt{2\pi}}\exp\left(-\frac{\left(\ln\left(d_{\text{hyd}}-\mu\right)\right)^2}{2\sigma^2}\right), \quad (6.10)$$

with μ and σ being the mean and standard deviation of d_{hyd}'s natural logarithm, respectively. In case birefringence is caused by particle aggregates rather than by individual particles, the particle size distribution in equation (6.9) is actually the distribution of the aggregate size.

Due to the asymmetry of the log-normal distribution geometric mean and standard deviation (which is multiplicative) are best suited as characterization parameters.[157] Then the confidence interval is asymmetric around the mean, and for one standard deviation (68.3%) the lower interval endpoint is calculated by dividing the geometric mean by the standard deviation, whereas the upper interval endpoint is obtained by multiplying both terms. Geometric mean $\overline{d_{\text{hyd}}}$ and standard deviation σ^* of d_{hyd} are given by

$$\overline{d_{\text{hyd}}} = e^{\mu} \quad (6.11)$$

and

$$\sigma^* = e^{\sigma}. \quad (6.12)$$

6.2 Optimizing magnetic field pulses

For TMB, the regime in which birefringence saturates is technically inaccessible since magnetic field pulses have to be not only quite high in order to align even the smallest nanoparticles, but it must also be very sharp so that the fall time of the magnetic field is much lower than the relaxation time of the particles. For example, in order to magnetize and align a dimer of nanoparticles with magnetite nucleus of 8 nm, a relatively high magnetic field strength of > 100 kA/m has to be applied (see Figure 5.7). If those particle dimers, suspended in water ($\eta = 0.89$ mPa s) at room temperature ($T = 25$ °C), have a hydrodynamic diameter of 22 nm, the Brownian relaxation time is only 3.5 µs (see equation 5.13 and Table 5.1). Thus, ideally, magnetic field pulses should have a strength of > 100 kA/m and fall times of only few microseconds.

A homogeneous magnetic field is created with two coils arranged in the Helmholtz configuration. In the following we will determine the adequate characteristics of the coils and the electronic circuit with which high field strengths and low rise and fall times (transition times) can be achieved. The optimization of these components is not trivial since there is a trade-off between the magnetic field strength and the inductance of the coil.

To achieve low rise and fall times, the inductance should be low, since the application of a voltage pulse to a solenoid leads to a current I that increases and decreases exponentially with the time constant L/R, where L and R are the inductance and resistance of the circuit, respectively. Both low inductance and high resistance diminish the transition time, but a high resistance also restricts the current (since $I = U/R$), and thus, should not be too high.

For the inductance of a short solenoid we have

$$L \propto \frac{n^2 r^2}{l + 0.9r}, \tag{6.13}$$

n being the number of windings in one coil, r the coil radius and l the length of the coil. Consequently, inductance will be low for coils of few windings and small radius.

On the other hand, for the magnetic field strength H in the center of an ordinary Helmholtz coil holds

$$H \propto \frac{nI}{r}, \tag{6.14}$$

where I is the current. Thus, high magnetic field strengths are achieved with high currents, a high number of windings, and a small coil radius.

To achieve both high magnetic field strengths and low inductance, the coil radius should be minimized. The lower bound of the coil dimensions is given by the size of the samples that have to be positioned in the center of the coil. We fabricated slightly elongated coils, since we are interested in creating a homogeneous field in direction of the laser beam, while the coils' cross-sectional area should be as small as possible. Optimized coil dimensions were found to be 15 x 8 x 5 mm, with a distance between coils of 8 mm (Figure 6.3a). Since H increases linearly with n, but L goes with the square of n, the number of windings should be kept rather low. We chose n to be 20. The magnetic field strength achieved with this coil was calibrated with a magnetometer (Magnet-Physik FH 54) to 0.96 kA/m per ampere (12 Oe per ampere). Furthermore we checked that the magnetic field in the center of the Helmholtz coils was homogeneous (in the volume

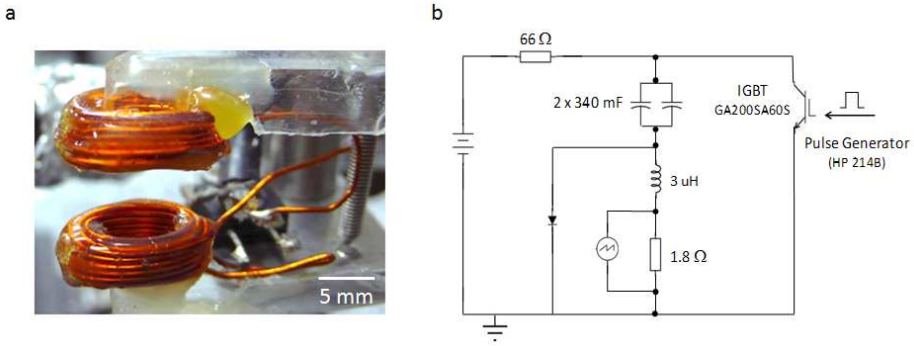

Figure 6.3 Setup optimization to create high and sharp magnetic field pulses. a) Small coil dimensions for low inductance and high magnetic fields. b) Electronic circuit to achieve fast switching and high currents.

in which the laser passes through the sample). The inductance of this coil was determined to be 3 μH.

High magnetic field strengths are achieved with high currents. Naturally, the voltage pulses applied to the solenoid must have short transition times, in order not to limit the rise and fall times of the current pulses. The high power pulse generator HP 214B creates voltage pulses of 100 V with a transition time of less than 15 ns. However, the maximum output current is only 2 A, so that the maximum magnetic field strength generated with this pulse generator and the optimized coils is merely 2 kA/m – a magnetic field strength at which birefringence is very low (see Figure 5.7). To create pulses of high current with low rise and fall times, a circuit was designed which employs a standard speed transistor IGBT (Insulated Gate Bipolar Transistor) and capacitors, as shown in the circuit diagram in Figure 6.3b. Two capacitors of 340 mF each are charged at high voltage (150 V, but only 250 mA, Delta Elektronika ES 0300-0.45) when the IGBT is closed. The gate of the IGBT is opened through voltage pulses delivered by the pulse generator HP 214B, leading to the capacitor

discharge. The current decay during capacitor discharge is not important here, since we are only interested in the magnetic field strength at the falling edge. When indicated, this current decay can be eliminated through including a further resistance between emitter and ground.[158] The IGBT GA200SA60S from International Rectifier offered optimal characteristics, since it allows collector-to-emitter voltages of up to 600 V and continuous collector currents of 100 A (at 100 °C). Furthermore, the gate closes (fall time) in less than 1 µs (the exact value depends on temperature). The IGBT dissipates maximally 250 W at 100 °C, which puts further constraints on voltage, current, resistance and duty cycle. To maintain the duty cycle as low as possible, the pulse period was set to the maximum the pulse generator allows (100 ms). The minimum pulse width, however, is given by the time the biggest particles present in the sample need to align with the magnetic field (400 µs for our particles), and limits the minimum duty cycle to 0.4%. Since both resistance (for low transition times) and current (for high field strengths) should be high, the voltage should be as high as possible. Nonetheless, the power must be significantly below the maximum power the IGBT can dissipate. We found the best compromise in using pulses of 130 V (at the rising edge) with 1.8 Ω, so that maximally 72 A flow through the coil (at the falling edge the current has decreased to 58 A). With a duty cycle of 0.4%, the power amounts to less than 38 W.

With these components, magnetic field pulses of 55 kA/m (700 Oe) field strength, 5 µs fall time and 400 µs pulse width (large enough so that equilibrium birefringence is reached) were applied, the pulse period being 100 ms. As Figure 5.7 shows, at $H = 55\,\mathrm{kA/m}$ and $T = 300\,\mathrm{K}$, birefringence due to the alignment of (aggregates of) Fe_3O_4 NPs of 8 nm in diameter is already close to the saturation value. On the other hand, particle dimers and higher order aggregates with hydrodynamic diameters greater than 25 nm show Brownian relaxation times greater than 5 µs. In

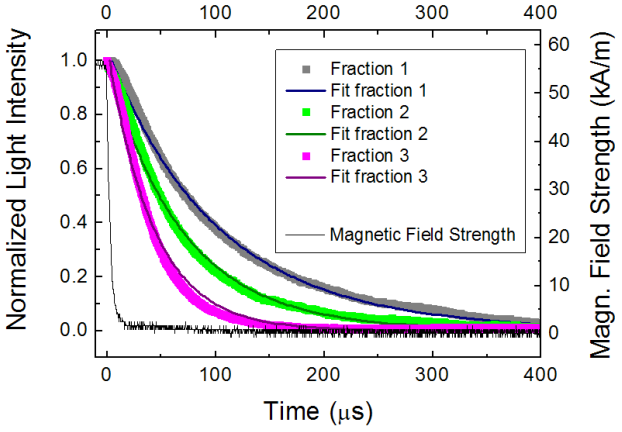

Figure 6.4 Measured magnetic field and birefringence decay. Decay of the magnetic field (black line) and the birefringence induced in a suspension of Fe_3O_4 NPs that have been separated by size (fractions 1 to 3). A fit of equation (6.9) yields the particle size distribution of the particles. Clearly, the decay of the magnetic field is significantly faster than the particle relaxation.

fact, for all particles studied in this thesis, the decay of the magnetic field has been significantly faster than the particle relaxation (see Figure 6.4).

6.3 Cuvette

A cuvette was designed to fit into the coil of reduced dimensions (Figure 6.5). The sample volume was minimized, consisting in a cylinder of a diameter of 2.8 mm (just slighly larger than the diameter of the laser beam) and a length of 8 mm. Thus, the sample volume amounts to only 50 μL. Naturally, the glass windows, through which the laser light passes, are nonbirefringent.

Measurements had to be performed at controlled temperature to control the protein quaterny structure. Since the application of the

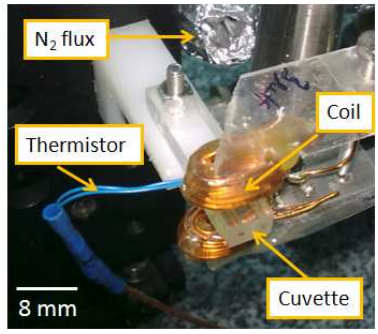

Figure 6.5 Photograph of cuvette and coil. A cuvette was designed to fit into the coil of reduced dimensions and to minimize the sample volume to only 50 µL. Temperature was measured in close proximity to the liquid cavity with a thermistor, and controlled by regulating the N_2 flow introduced for heat dissipation.

intense magnetic fields led to the heating of the sample, a slight N_2 flow was introduced to conduct the heat away. Due to the lack of space, temperature could not be measured directly inside the sample volume, but was rather measured in close proximity to the liquid cavity. Since no strong temperature gradients were present, this strategy allowed for a satisfactory temperature control. For the temperature measurements a thermistor (miniature NTC S861, 10 kΩ) was used in combination with a temperature controller (Newport 325B).

A photograph of the complete experimental setup is shown in Figure 6.6. The experimental procedure is straightforward: The sample is inserted in the setup (Figure 6.2), the magnetic field pulses are turned on and the transmitted light intensity is acquired in a time interval of 10 s. A regression of equation (6.9) to the transmitted light intensity yields the particle size distribution of the particles.

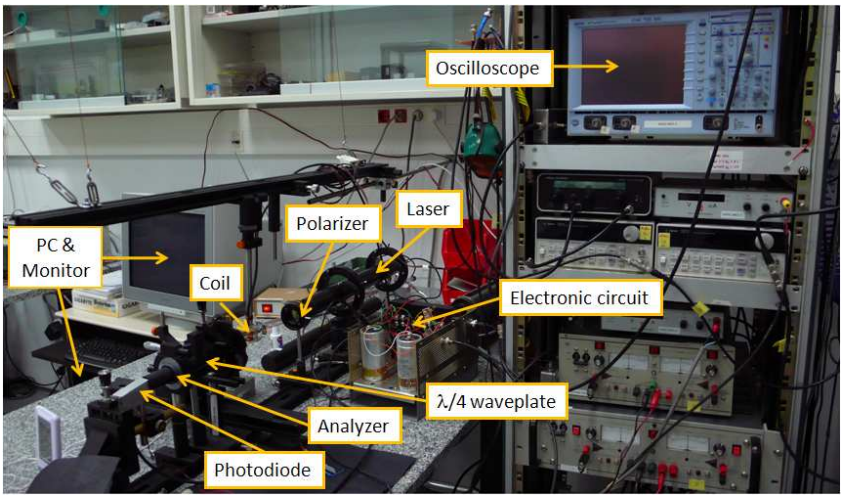

Figure 6.6 Photograph of the experimental setup for measuring Transient Magnetic Birefringence

Author contributions

Parts of this chapter have been published as *Transient magnetic birefringence for determining magnetic nanoparticle diameters in dense, highly light scattering media* by Mariana Köber, María Moros, Valeria Grazú, Jesus M. de la Fuente, Mónica Luna and Fernando Briones in Nanotechnology **23** 155501 (2012). The implementation and optimization of the Transient Magnetic Birefringence (TMB) measurement setup has been accomplished by myself under the supervision of Fernando Briones.

Chapter 7

Application of Transient Magnetic Birefringence to Dense, Highly Light Scattering Media[1]

The increasing use of biofunctionalized magnetic nanoparticles in biomedical applications calls for further development of characterization tools that allow for determining the interactions of the nanoparticles with the biological medium *in situ*. In cell-incubating conditions, for example, nanoparticles may aggregate and serum proteins adsorb on the particles, altering the nanoparticles' performance and their interaction with cell membranes. In the following it is shown that the aggregation of spherical magnetite nanoparticles can be detected with high sensitivity in dense, highly light scattering media by making use of magnetically induced birefringence. Moreover, the hydrodynamic particle diameter distribution of anisometric nanoparticle aggregates can be determined directly in these media by monitoring the relaxation time of the magnetically induced

[1]The essential parts of this chapter have been published as *Transient magnetic birefringence for determining magnetic nanoparticle diameters in dense, highly light scattering media* by Mariana Köber, María Moros, Valeria Grazú, Jesus M. de la Fuente, Mónica Luna and Fernando Briones in Nanotechnology **23** 155501 (2012).

birefringence. As a proof of concept, measurements were performed on nanoparticles included in an agarose gel, which scatters light in a similar way as a more complex biological medium but where particle-matrix interactions are weak. Magnetite nanoparticles were separated by agarose gel electrophoresis and the hydrodynamic diameter distribution was determined *in situ*. For the different particle functionalizations and agarose concentrations tested, it could be shown that gel electrophoresis did not yield a complete separation of monomers and small aggregates, and that the electrophoretic mobility of the aggregates decreased linearly with the hydrodynamic diameter. Furthermore, the rotational particle diffusion was not clearly affected by nanoparticle-gel interactions. The possibility to detect nanoparticle aggregates and their hydrodynamic diameters in complex scattering media like cell tissue makes Transient Magnetic Birefringence (TMB) an interesting technique for biological applications.

7.1 Introduction

Biofunctionalized MNPs are of growing interest for biomedical applications such as magnetic resonance imaging contrast enhancement, immunoassay, hyperthermia, and drug delivery.[23,24] For these biomedical applications, colloidal nanoparticles are manipulated in physiological conditions, those being buffer, serum or cell tissue. Recent studies confirm that proteins and other biomolecules adsorb onto the nanoparticles when those are exposed to biological fluid.[159] Moreover, some aggregation may occur despite adequate particle functionalization, and both - adsorption of proteins and particle aggregation - may directly affect nanoparticle performance, for example in cell-incubating conditions where nanoparticle aggregation and protein adsorption alter the nanoparticles' interaction with the cell

membranes.[38] To control nanoparticle performance *in situ*, techniques are needed which allow for detecting the presence of nanoparticle aggregates and the adsorption of biomolecules in dense, highly light scattering media.

The hydrodynamic particle diameter is an indicator of particle aggregation and the adsorption of biomolecules, since it comprises the inorganic core, the surfactant molecules and the solvent layer attached to the particle when it moves. While the geometric size of the inorganic core has been extensively characterized, little is known about the hydrodynamic size of water soluble nanoparticles, even though it is an important parameter for understanding, controlling and optimizing the nanoparticles' performance in biological assays as well as the particles' migration in live cells and tissues. Studies have shown that hydrodynamic radii are strongly affected by nature and lateral extension of the capping ligands and, furthermore, systematically larger than the geometric radii for the inorganic core plus cap, since the coating layer strongly interacts with the surrounding solvent[144]. Since both the conformation of the surfactant molecules[145] and the hydration layer[146] affect the particles' chemical functionality, monitoring the hydrodynamic particle diameter is of major interest in a variety of applications.

In the following the benefits and drawbacks of using Transient Magnetic Birefringence (TMB) to determine the hydrodynamic diameters of magnetite nanoparticles in dense, highly light scattering media will be analyzed. So far, TMB has only been applied to nanoparticle suspensions,[32–34] but never to dense, highly light scattering media. Here, the method is studied for magnetite nanoparticles included in an agarose gel – a model system in which the viscosity inside the gel cavities is known and the particle interaction with the matrix is weak. As a proof of concept for this technique, nanoparticles of different functionalizations were separated by agarose gel electrophoresis and their hydrodynamic

diameters were determined *in situ* as a function of electrophoretic mobility. In these experiments, we expect that a moderate light depolarization due to multiple scattering has no major effect on the determination of the hydrodynamic radius by means of TMB, since the basis of this method is the analysis of the time dependence of the birefringence decay after the magnetic field is switched off, whereby this birefringence emergence and decay only arises from magnetic nanoparticle alignment and relaxation upon the application of magnetic field pulses, while light depolarization due to background scattering is constant at all times.

A systematic study is presented, comparing the hydrodynamic diameter values obtained *in situ* by TMB with those obtained *ex situ* by Dynamic Light Scattering (DLS), and correlate both to observations made in microscopy studies (TEM and AFM). In this way it is demonstrated that the main contribution to the birefringence signal comes from dimers and higher order aggregates of spherical Fe_3O_4 nanoparticles, while monomers do not yield an appreciable birefringence signal. Therefore, magnetically induced birefringence can be used in sensitive sensor applications, where molecular recognition is detected through a significant rise in birefringence through specific and controlled aggregation of adequately functionalized magnetite particles. The presented results pave the way to use magnetically induced birefringence for studying possible interactions of the nanoparticles with their biological surroundings in dense, highly light scattering media like living cells and tissue.

7.2 Experiments in agarose gels

Experiments were performed with spherical Fe_3O_4 (magnetite) nanoparticles with different functionalizations.[160] Magnetite nanoparticles are widely employed in biomedical applications due to the ease of fabrication and

their low toxicity. Monodisperse spherical Fe_3O_4 nanoparticles of 8 nm mean diameter (see the TEM image in Figure 7.6a and Figure 7.11) were synthesized following the seed-mediated growth method.[161] In order to achieve water solubility, the synthesized NPs were coated with an amphiphilic polymer shell, namely a poly(maleic anhydride-alt-1-octadecene) (PMAO) shell.[162] PMAO functionalized Fe_3O_4 nanoparticles are stable in aqueous solutions - currently available data demonstrate stability for over two years.[163] A fraction of these particles was modified subsequently with galactose (Gal) and another fraction with polyethylene glycol (PEG), as shown schematically in Figure 7.3a.

Here the application of TMB to magnetite nanoparticles included in an agarose gel was studied, for which particles were separated by their electrophoretic mobility in the gel.

Particle separation by gel electrophoresis

The movement of electrically charged particles through a transport material in an electrical field is called electrophoresis. The velocity of migration is proportional to the applied field strength and the particle's net charge, and inversely proportional to the effective radius and the viscosity of the mixture. Gel electrophoresis uses a gel as an anticonvective or sieving medium (see the schematic representation in Figure 7.1). It is commonly employed to separate biomolecules (DNA, RNA, proteins), and has lately also been applied to the separation of NPs and NP-biomolecule conjugates according to differences in their size and/or zeta potential (for a recent review see [164]). The electrophoretic particle mobility (= particle velocity / electric field strength) depends on the relation of the particle size to the gel pore size and on the particles' net charges. When the nanoparticle size is very small compared to the gel pore size, the particles'

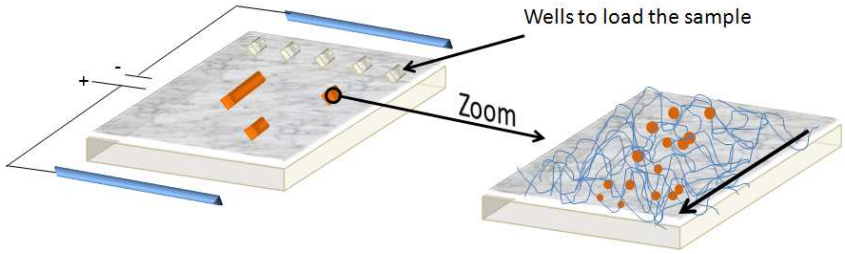

Figure 7.1 Schematic illustration of gel electrophoresis. Left: The NP suspension is loaded in the wells and a voltage is applied across the gel. The zoom on the right shows how the particles move through the matrix formed by polymer bundles and interstitial spaces (pores), whereby the pore size of the gel matrix decreases with the polymer concentration. The electrophoretic particle mobility depends on the particles' net charges and on the relation of the particle size to the gel pore size.

net charges are determinant for the electrophoretic mobility. In this case the electrophoretic mobility may increase with particle size.[165] On the contrary, when the nanoparticles are big enough to "sense" the gel pore walls, steric restrictions and an increased hydrodynamic drag caused by the pore walls lead to a reduced electrophoretic mobility for bigger particles.[166] Gel electrophoresis has proven useful to separate nanoparticle assemblies according to their size[166], shape[165] or even to the number of functional groups attached to them[145,167]. The separation quality has been shown to be strongly influenced by the functionalization layer.[165,167]

Here, a separation of the magnetic nanoparticles through their electrophoretic mobility was carried out in agarose gels. Agarose is a polysaccharide of neutral charge which forms an inert matrix that is not likely to interact with biomolecules. Therefore, it is a standard matrix for gel electrophoresis. The matrix is formed by polymer bundles and interstitial spaces (pores), whereby the pore size decreases with the agarose concentration.[168] Gels of 0.5% and 2% w/v agarose concentrations in 0.5x Tris-Borate-EDTA (TBE) buffer (pH $\approx$ 9) were prepared, and NPs were

separated by applying 5 $\mathrm{Vcm^{-1}}$ for 105 min and 110 min, respectively. Photographs (Figure 7.3b and 7.3c, true color brightness-enhanced) show that the particles move in a single band for both agarose concentrations.

7.2.1 Measuring procedure

After electrophoretic separation the hydrodynamic particle diameters were determined *in situ* (while the particles remained included in the gel) with TMB, as a function of electrophoretic mobility. The *in situ* determination of the hydrodynamic particle diameter through Transient Magnetic Birefringence (TMB) shall be illustrated schematically for the nanoparticles functionalized with PMAO+PEG separated in a 0.5% w/v gel. For measuring the relaxation time one gel lane was cut and fixed on the sample holder (see the experimental setup illustrated in Figure 6.2). The relaxation of the magnetically induced birefringence was measured as a function of the distance from the well as indicated in Figure 7.2a. The normalized light intensity transmitted through different spots in the gel lane is shown in Figure 7.2b. A regression of equation (6.9) to the transmitted light intensity yields the hydrodynamic diameter distribution of the particles (with $\eta = 0.89$ mPa s and $T = 25$ °C), shown in Figure 7.2c. It can be seen how the size distribution narrows as the distance traversed by the particles increases.

7.2.2 Results for different pore sizes and particle functionalizations

Results for particles of the three different functionalizations (PMAO, PMAO+Gal and PMAO+PEG) and two different agarose concentrations (0.5% w/v and 2% w/v) are summarized in Figure 7.3. The regions in

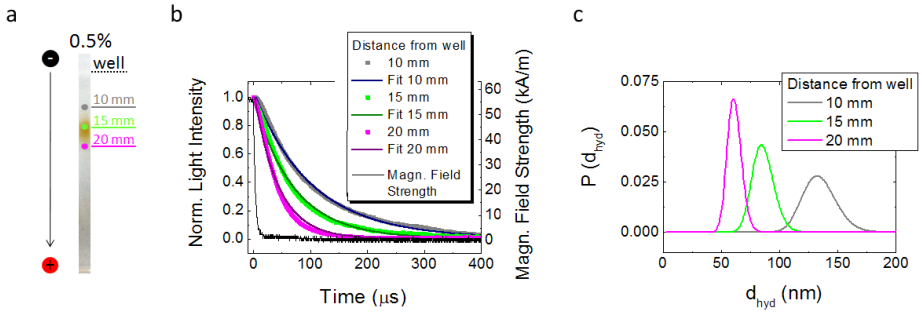

Figure 7.2 Procedure to determine hydrodynamic nanoparticle diameter distributions *in situ* by Transient Magnetic Birefringence. (a) Brightness enhanced true color photograph of the 0.5% w/v agarose gel showing the Fe_3O_4 nanoparticles functionalized with PMAO+PEG after the electric field had been applied. (b) Normalized light intensity transmitted at three different spots of the gel lane. A regression of equation (6.9) to the signal amplitude yields the hydrodynamic diameter distribution of the particles. (c) Distribution of the hydrodynamic particle diameters $P(d_{\mathrm{hyd}})$ present at the different spots in the gel lane.

which the birefringence signal was significant (> 5 mV) is marked by a dotted box in the photographs.

The electrophoretic mobility depends approximately linearly on the hydrodynamic diameter, independently of the particle functionalization and agarose concentration. Among the particles of the same functionalization a separation by size occurs, due to a reduced electrophoretic mobility for increasing hydrodynamic diameters. The electrophoretic mobility depends strongly on the agarose concentration, in consequence of the pore diameter. From the finite rotational mobility observed with TMB it can be deduced that particles are not trapped, but rather retained through an increased hydrodynamic drag caused by the pore walls and/or steric restrictions. Only particles with a hydrodynamic diameter > 80 nm in the 2% gel are trapped in the first gel section close to the well, in contrast to the 0.5% gel where aggregates of 140 nm pass. Also the particle size distribution

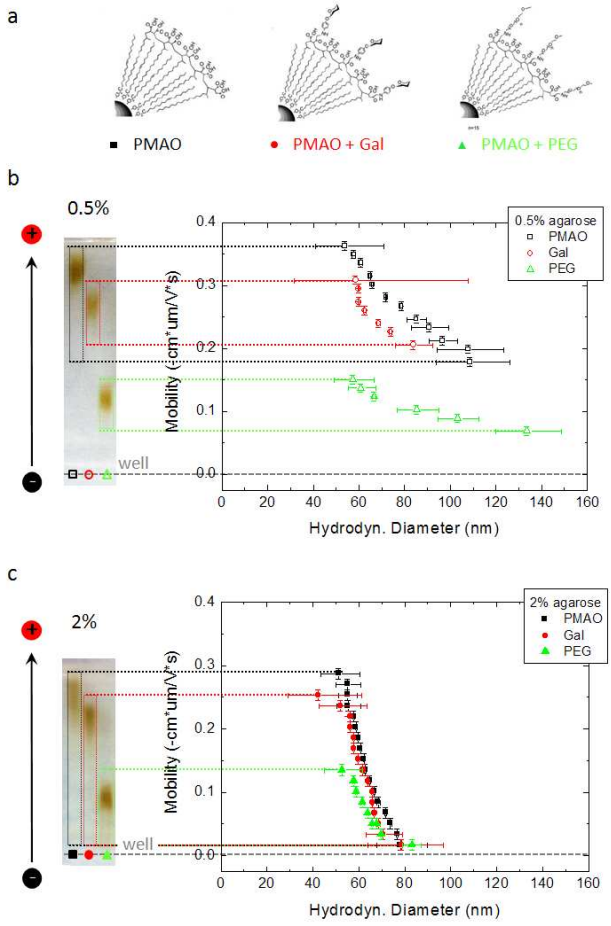

Figure 7.3 Electrophoretic nanoparticle mobility as a function of the mean hydrodynamic particle diameter determined *in situ* by Transient Magnetic Birefringence (TMB). (a) Functionalization of the Fe_3O_4 nanoparticles (PMAO with optional Gal or PEG modification) (b) and (c) left: Brightness enhanced true color photograph of a 0.5% and 2% agarose gel, respectively, after the electric field had been applied. The three lanes contain particles functionalized with PMAO (left lane), PMAO+Gal (middle lane) and PMAO+PEG (right lane), as indicated by the symbols; right: Electrophoretic mobility dependence on the hydrodynamic particle diameter, as measured *in situ* by TMB. Plotted is the geometric mean diameter with the confidence interval of one standard deviation.

width depends clearly on the gel pore size, as the confidence intervals of one standard deviation, represented through x-bars in the graphs, show. While for a 0.5% gel the size distribution width decreases slowly with increasing traversed distance, for a 2% gel it is negligibly small even for particles that have hardly traversed any distance in the gel. At the forefront of the band (high electrophoretic mobility) some size dispersion remains for both agarose concentrations. Smaller gel pores would be necessary to achieve a full size separation.

The differences in electrophoretic mobility resulting from modifying the particle functionalization can be attributed mainly to the differences in the particles' net charges since the hydrodynamic particle diameters are very similar. This tendency is reflected in the zeta potentials determined in water, which resulted to be -53 mV for the PMAO functionalized particles, -32 mV for the particles modified with galactose and -1.8 mV for those modified with PEG. The deprotonation of the PMAO carboxilic groups in the basic environment of the TBE buffer (pH $\approx$ 9) is responsible for the PMAO coated particles to be negatively charged. By adding galactose or PEG molecules to the coating layer, charge and, therewith, particle mobility is reduced significantly, whereas the hydrodynamic particle size is hardly affected.

Figure 7.3 demonstrates clearly that with TMB magnetite nanoparticle diameters can be determined in dense, highly light scattering media with high sensitivity (170 µM Fe_3O_4) and low dispersion of the data. In particular, it should be stressed that, while the color in the photo clearly indicates strong fluctuations in particle concentration along the gel lane, the electrophoretic mobility vs hydrodynamic diameter does not deviate from a linear behavior. This suggests that fluctuations in the number of light scattering events do not affect the determination of the particle diameter with TMB, even though we are in the multiple

scattering regime. In fact, cross-check experiments have shown that the light depolarization caused by the gel and fluctuations in the particle concentration do not affect the hydrodynamic diameter measurements significantly, and hydrodynamic diameter fluctuations lie within only 1.7% (Figure 7.4). In fact, our 2% agarose gel samples of 6 mm thickness imply a depolarization of the transmitted laser light of only 0.3%. Measurements were performed on nanoparticle suspensions of different concentrations (ranging from the maximum concentration used in our experiments to the minimum concentration giving detectable birefringence), and with a 2% agarose gel positioned behind the nanoparticle suspension to take into account the light depolarization caused by the gel but rule out gel-NP interactions.

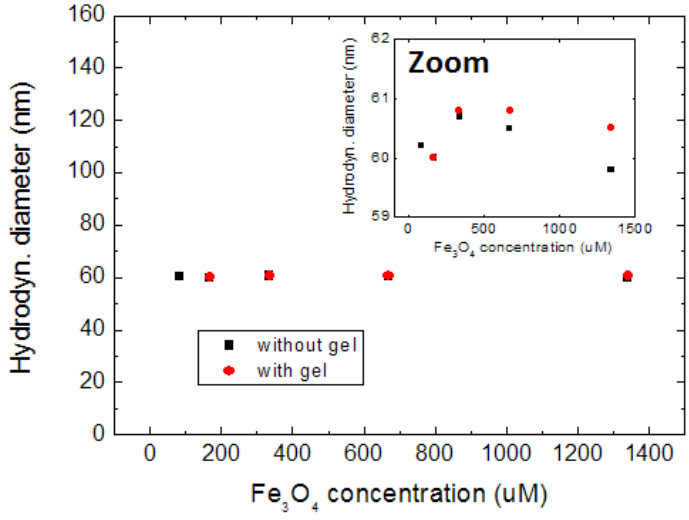

Figure 7.4 Effect of the gel and fluctuations in the particle concentration on the particle sizes with TMB. Hydrodynamic diameter vs nanoparticle concentration (scaled as in Figure 7.3 and zoomed in the inset). Measurements were performed on nanoparticle suspensions of different concentrations (black squares), and with a 2% agarose gel positioned behind the nanoparticle suspension (red dots).

Unlike for the electrophoretic mobility, no clear evidence was found that the rotational mobility depends on the gel pore size: the lowest detected hydrodynamic diameter is very similar for both agarose concentrations, and results of *in situ* and *ex situ* measurements do not show an unambiguous trend (Figure 7.5). After TMB measurements were performed in situ, the gel was cut into pieces and the pieces were submerged in TBE buffer. After most of the particles had diffused out of the gel (which took a few days) TMB measurements were performed *ex situ*, where the particles were freely moving in the buffer. Note that the 0.5% agarose gel data corresponds to that presented in Figure 7.3, while the 2% agarose gel data is from another experiment performed under the same conditions. In Figure 7.5 some differences (deviations are within 10%) for the hydrodynamic diameters determined *ex situ* and *in situ* can be observed. Nonetheless, it has to be taken into account that possibly not all particles diffuse out of the gel and that after the particle extraction the cluster size distribution may have changed. Therefore, those differences should not be interpreted as any clear evidence that rotational diffusion depends on pore size.

We can see in Figure 7.3 and Figure 7.5 that obtained diameter values are relatively high. Theoretical studies suggested that the main contribution to the birefringence signal comes from the orientation of pre-existing dimers and anisometric aggregates,[36,37] since both shape anisotropy and intrinsic optical anisotropy of nominally spherical magnetite nanoparticle monomers are low. The fact that the transfer of nanoparticles from organic solvents to water based solutions usually involves the formation of some small aggregates supports this suggestion.[139]

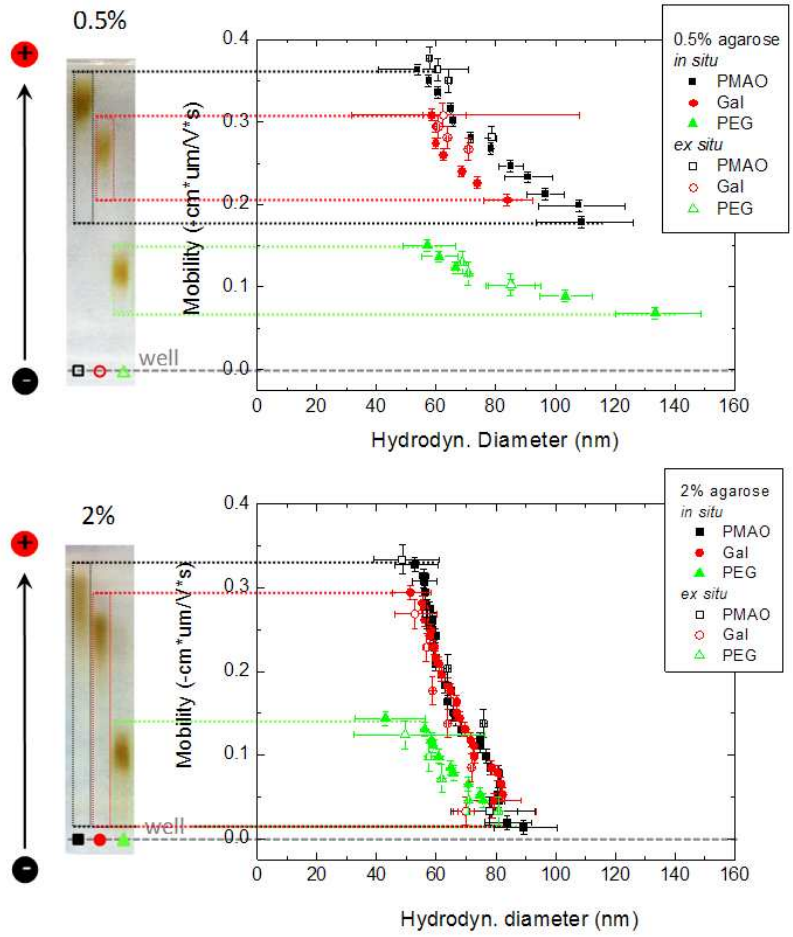

Figure 7.5 Comparison of TMB *in situ* and *ex situ* measurements. Electrophoretic nanoparticle mobility as a function of the mean hydrodynamic particle diameter determined *in situ* and *ex situ* by TMB. Particles of different functionalizations (PMAO with optional subsequent Gal or PEG modification) had been separated by electrophoresis in agarose gels of different agarose concentrations (0.5% and 2%). Plotted is the geometric mean diameter with the confidence interval of one standard deviation.

7.3 Contrasting studies

7.3.1 Microscopy studies

Microscopy measurements were performed to check for the presence of aggregates. TEM images of PMAO functionalized nanoparticles show mainly monodisperse nanoparticles, but suggest the presence of some aggregates (Figure 7.6a). However, organic material is not visible in these images, and it is not clear whether several particles are enwrapped in a common polymer shell. With AFM organic material is imaged, and with Amplitude Modulation Atomic Force Microscopy (AM-AFM) with phase-locked loop different materials can be differentiated through the excitation frequency shift (see Section 2.3, page 37f.). Aggregates appearing as one single cluster in the topography image (Figure 7.6b, left) can be assigned the number of particles constituting them from the excitation frequency shift image (Figure 7.6b, right). AFM inspection revealed that, although a large part of the particles is monodispersed, a considerable fraction of the particles is present in the form of dimers, trimers and higher order aggregates which mainly contribute to the birefringence.

7.3.2 Ex situ Dynamic Light Scattering measurements

In order to cross-check the measured hydrodynamic diameter values with an established technique, *ex situ* Dynamic Light Scattering (DLS) measurements were performed. DLS is a widely used method for measuring the hydrodynamic diameter distribution of suspended particles and their aggregates due to its versatility, based on the fact that it detects any kind of particles (of sizes between approximately 1 nm and 10 µm) present in very dilute suspensions, independently of their physical (optical, magnetic...) properties. The insensitiveness to a certain particle

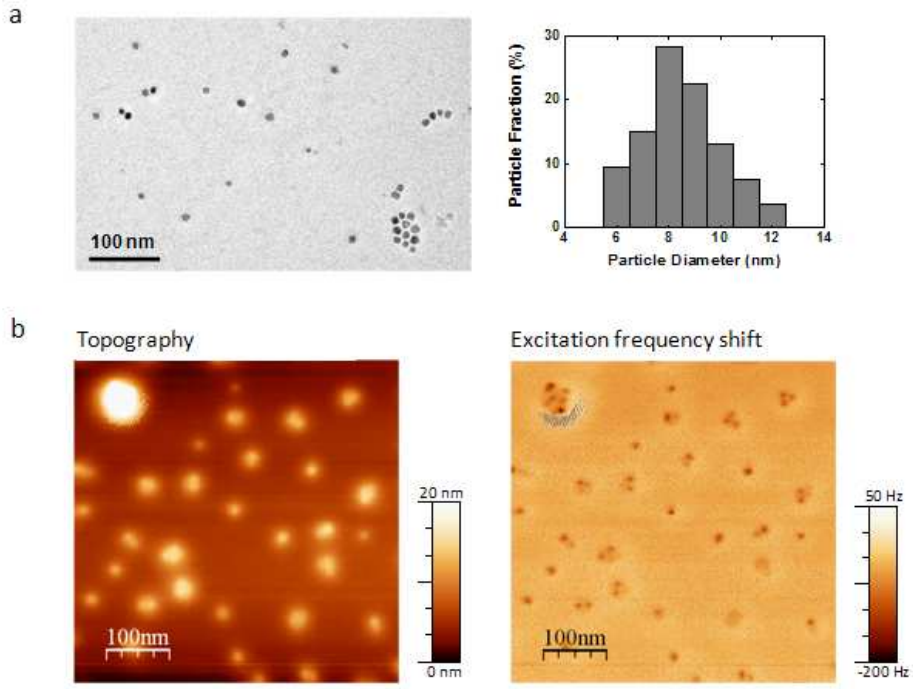

Figure 7.6 Characterization of nanoparticle size, shape and aggregation. (a) Typical TEM image showing both size and shape distribution of the nanoparticles' inorganic Fe_3O_4 core. Particles show no appreciable non-sphericity. The particle size distribution was determined from about 100 particles (Figure 7.11 shows a TEM image with high particle density). Images with low nanoparticle density as shown here suggest the presence of some aggregates; (b) AFM images confirm that, indeed, particle dimers, trimers and higher order aggregates are present.

property, however, makes the technique unsuitable for determining the sizes of particles suspended in serum or even embedded in dense, highly light scattering media like cell tissue, and particle diameters can only be characterized *ex situ* (for details on DLS see Section 7.5). Therefore, measurements were performed on the PMAO functionalized particles after they had diffused out of the 2% gel into buffer solution.

DLS shows (Figure 7.7) that two populations remain throughout the entire gel lane, but each population shifts to lower diameter values with increasing traversed distance. In Table 7.1 the mean hydrodynamic diameters of the two populations are listed. We attribute the two DLS populations to particle monomers ($d_{\mathrm{hyd},1}$) and aggregates ($d_{\mathrm{hyd},2}$). The presence of these two populations throughout the whole gel lane demonstrates that agarose gel electrophoresis does not yield a complete separation of nanoparticle monomers from dimers, possibly due to the dimers moving with one particle in the slip stream of the other. It should be noted that larger particles yield a higher contribution to the scattered light intensity, since the scattered light intensity depends on the particle diameter to the sixth power. Thus, although in number only few large particles are present, the scattered light intensity of these large particles is relatively high. In fact, a conversion of the size distribution by intensity (shown in Figure 7.7) to the size distribution by number shown in Figure 7.8 demonstrates that the number of aggregates is actually very low. This confirms the sensitivity of light scattering techniques to particle aggregation.

The comparison of hydrodynamic diameters determined by TMB and DLS gives the definite evidence that TMB does not detect nanoparticle monomers: Monomer nanoparticles have DLS hydrodynamic diameters <40 nm, whereas the lowest hydrodynamic particle diameter detected with TMB is 55 nm. This demonstrates that dimers and higher aggregates of spherical magnetite nanoparticles yield the main contribution to the birefringence signal, while monomers do not contribute significantly - in agreement with theoretical results which proposed the orientation of pre-existing aggregates to give the main contribution to the birefringence signal.[36,37] The particle size distribution in equation (6.9) is then actually the distribution of the aggregate size and a log-normal distribution is

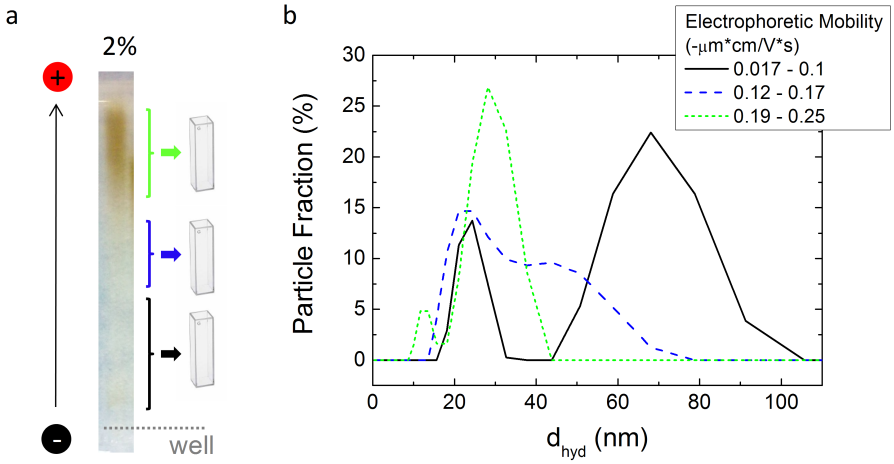

Figure 7.7 Hydrodynamic nanoparticle diameter distribution by intensity, determined *ex situ* by Dynamic Light Scattering (DLS). (a) Photograph of the 2% w/v agarose gel after applying 5 Vcm^{-1} during 110 min (NPs functionalized with PMAO). The ranges of the gel from which particles were collected for the DLS measurements are indicated. (b) Hydrodynamic diameter distribution (by intensity) of the particles after separation through gel electrophoresis, obtained by DLS after particle diffusion out of the gel.

Mobility (-μm cm $V^{-1}s^{-1}$)	$d_{hyd,1}$ (nm)	$d_{hyd,2}$ (nm)
0.017-0.1	22	70
0.12-0.17	22	45
0.19-0.25	13	30

Table 7.1 Mean hydrodynamic diameters of the two populations detected by DLS after nanoparticles functionalized with PMAO had diffused out of the 2% agarose gel into buffer solution. Throughout the entire gel lane two populations remain (associated to particle monomers ($d_{hyd,1}$) and particle aggregates ($d_{hyd,2}$)), but each population does shift to lower diameter values with increasing traversed distance.

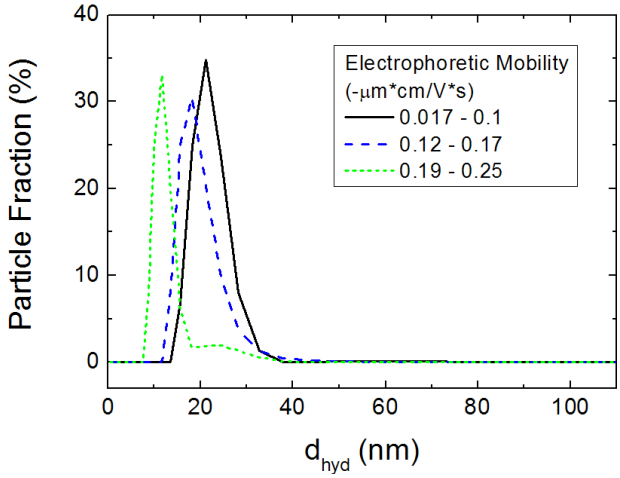

Figure 7.8 Hydrodynamic diameter distribution by number of the PMAO functionalized Fe_3O_4 nanoparticles obtained by DLS after particle diffusion out of the 2% gel into buffer solution. Although the number of particles with $d_{\mathrm{hyd}} > 50$ nm is extremely low, the scattered light intensity of these large particles is very high (compare to Figure 7.7).

justified. The inter-particle distance is approximately 1.5 times the particle diameter, since the polymer is covering each particle (see TEM and AFM micrographs in Figure 7.6). Due to this low inter-particle distance dipolar interactions are important and capable of giving rise to an effective torque to the aggregate in the external pulsed magnetic field. On the other hand, magnetic field induced aggregation of our superparamagnetic nanoparticles has not been observed, as expected.

By comparing TMB and DLS measurements we can also deduce that TMB does not detect aggregates of small nanoparticles: Particles that were extracted far from the well (with high mobility) present a second peak (due to aggregates) in DLS with diameters < 45 nm, which were not detected with TMB. This might be due to the weak magnetic

dipolar interaction of small particles (the magnetic moment of the iron oxide NPs decreases when the NP diameter drops below 10 nm, and this significantly when the diameter falls below 5 nm)[149] which impedes the alignment of these aggregates with the magnetic field. In consequence, in the case of spherical NPs, the birefringence does not depend on the total NP concentration, measured through the optical absorption, but only on the dimers' and anisometric aggregates' contribution of not too small nanoparticles (see Figure 7.9).

Generally, differences in the hydrodynamic diameters determined by DLS and TMB are expected since different techniques are sensitive to different particle properties and none of the results are inherently correct or absolute. While for TMB the rotational component of the Brownian motion is decisive, in DLS it is the translational component. Depending on the shape of the objects this may lead to significant variations in the determined hydrodynamic diameter. In this case Depolarized Dynamic Light Scattering would be more appropriate for comparison studies. Nonetheless, studies comparing effective particle sizes obtained with different techniques have shown that variations are especially pronounced when particles are functionalized with long and complex surfactant molecules or polymer layers[169] as it is the case here. Then the approximation that the hydrodynamic diameter is the inorganic core diameter plus two times the thickness of the organic layer breaks down and both the steric conformation of the organic molecules and the hydration influence the hydrodynamic diameter significantly. Nevertheless, always when using one method consistently, relative changes in hydrodynamic diameters are meaningful.

Since TMB only detects not too small MNPs with shape anisotropy, it is not an appropriate method for the hydrodynamic particle size determination in general as is DLS. The strength of the technique lies

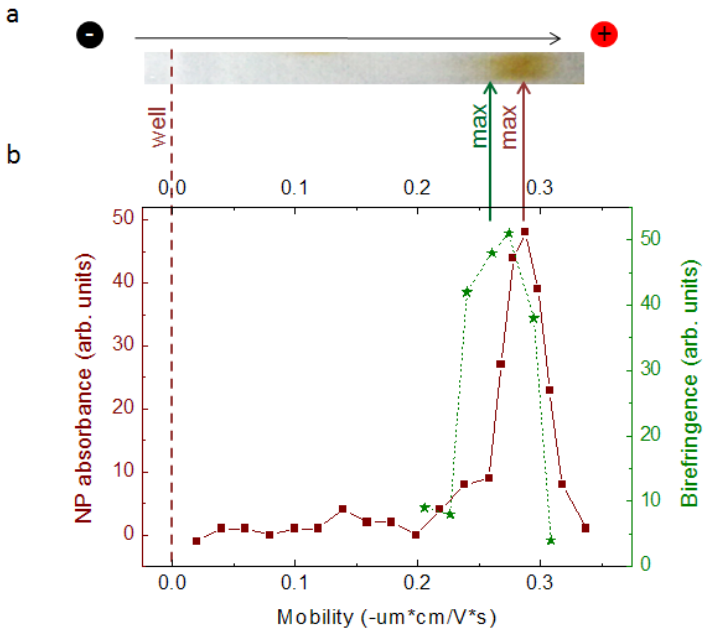

Figure 7.9 Birefringence depends on the concentration of dimers and anisometric aggregates. a) Brightness enhanced true color photograph of a 0.5% agarose gel containing Fe_3O_4 nanoparticles functionalized with PMAO+Gal, after 5 Vcm^{-1} had been applied for 105 min b) The comparison of nanoparticle absorbance and birefringence illustrates that birefringence does not depend on the total NP concentration, measured through the NP absorbance, but only on the dimers' and anisometric aggregates' contribution (the birefringence maximum is shifted to lower mobilities with respect to the maximum of the NP absorbance). NP absorbance was determined by comparing the yellow component of the photograph at the gel lane center and border.

rather in taking advantage of distinguishing particle features like their magnetic properties and shape anisotropy which allow for monitoring the particles' hydrodynamic diameter and detecting molecular recognition in highly dispersive media in situ, for example in biological tissue where proteins or other present molecules may adsorb and particles may aggregate, thus altering the performance of the particles through changes

in their functionality and size. Standard Dynamic Light Scattering, however, can only be used in very dilute nanoparticle suspensions and not for nanoparticles suspended in serum or even embedded in complex scattering media like cell tissue. For these applications TMB presents an inexpensive and easy to build solution.

7.4 Conclusions

Transient Magnetic Birefringence (TMB) is a sensitive tool for monitoring the hydrodynamic diameters of anisometric magnetic nanoparticles in dense media with strong background light scattering (as schematically illustrated in Figure 7.10). The technique was applied to the *in situ* measurement of hydrodynamic diameters of spherical Fe_3O_4 nanoparticles after their electrophoretic separation in agarose gels. Although multiple light scattering in dense media diminishes the polarization of the transmitted light, in this work it is shown that with TMB reliable results are obtained even for dense, highly light scattering media such as an agarose gel. This presents a proof of concept in a model system that scatters light in a similar way as a more complex biological medium but where particle-matrix interactions are low. In fact, no significant effect of gel-particle interactions on the rotational particle diffusion was observed. In this systematic study, comparing the hydrodynamic diameter values obtained *in situ* by TMB with those obtained *ex situ* by Dynamic Light Scattering (DLS), and correlating both to observations made in microscopy studies (TEM and AFM), it is demonstrated that the main contribution to the birefringence signal comes from dimers and small optically anisotropic aggregates of spherical Fe_3O_4 nanoparticles. Indeed, monomers do not yield any appreciable birefringence signal. Therefore, magnetically induced birefringence can

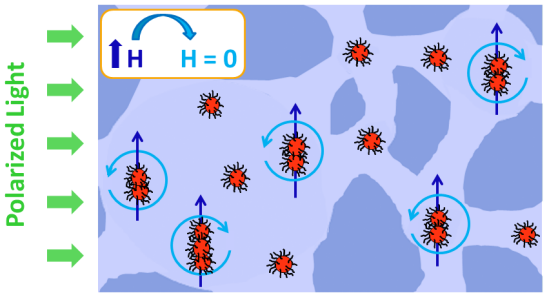

Figure 7.10 Illustration: TMB of magnetic nanoparticles in the agarose gel

be used in sensitive molecular recognition applications, where specific and controlled dimerization of functionalized magnetite particles can be detected through a significant rise in birefringence. These results pave the way to use magnetically induced birefringence for studying possible interactions of the nanoparticles with their biological media like living cells and tissue.

7.5 Materials and Methods

Synthesis of 8 nm iron oxide nanoparticles

Monodisperse iron oxide nanoparticles of 8 nm in diameter were synthesized following the seed-mediated growth method described by Sun.[161] Several studies performed earlier have shown that the iron oxide of these NPs is Fe_3O_4.[138] First, 6 nm Fe_3O_4 nanoparticle seeds were synthesized by mixing and stirring under a flow of argon, $Fe(acac)_3$ (0.71 g), 1,2-hexadecanediol (2.58 g), oleic acid (2 mL) and oleylamine (2 mL), solubilized in phenyl ether (20 mL). The mixture was heated to 200 °C for 2 h and afterwards heated to reflux (265 °C) under argon atmosphere for 1 h. The mixture was allowed to cool to room temperature

and the nanoparticles were washed by adding ethanol and collecting them with a magnet and redispersed in hexane three times. NPs were redispersed in 10 mL hexane containing 50 µL of oleic acid and 50 µL of oleylamine. In order to obtain 8 nm nanoparticles, 80 mg of the 5-6 nm Fe_3O_4 seeds in hexane were added to a mixture containing $Fe(acac)_3$ (0.71 g), 1,2-hexadecanediol (2.58 g), oleic acid (0.5 mL), oleylamine (0.5 mL) and 20 mL of phenyl ether. The mixture was heated to 100 °C for 30 min to remove the hexane and then to 200 °C for 1 h. Under argon atmosphere the mixture was further heated to reflux (265 °C) for another hour. The mixture was allowed to cool at room temperature by removing the heat source and as described for the 6 nm nanoparticles, they were precipitated with ethanol and resuspended in hexane. NPs of 8 nm were precipitated with ethanol and weighted once completely dry.

Water solubilisation of hydrophobic magnetic nanoparticles

In order to achieve water solubility the synthesized nanoparticles were coated with an amphiphilic polymer shell, namely a poly(maleic anhydride-alt-1-octadecene) (PMAO) shell.[162] 250 mg of poly(maleic anhydride-alt-1-octadecene) (PMAO) was added to a flask containing 200 mL of chloroform. After the polymer was dissolved under magnetic stirring, 20 mg of the nanoparticles were added and the mixture was gently stirred for one hour at 25 °C. Afterwards, the solvent was removed under vacuum and few millilitres of chloroform were added. Nanoparticles were then resuspended in 20 mL of NaOH 0.05 M and the sample was shaken at 60 °C in order to speed up the complete evaporation of chloroform. At this point the solution became clear as NPs were completely transferred into water. NPs were then filtered on syringe filters of 0.22 µm. The NP solution was centrifuged three times at 25,000 rpm for 2 h to remove the excess unbound polymer molecules. The nanoparticles at the bottom

were recovered and redispersed in water. Thus, finally, the nanoparticles present a magnetite core of 8 nm in diameter and a shell of PMAO of about 3 nm.

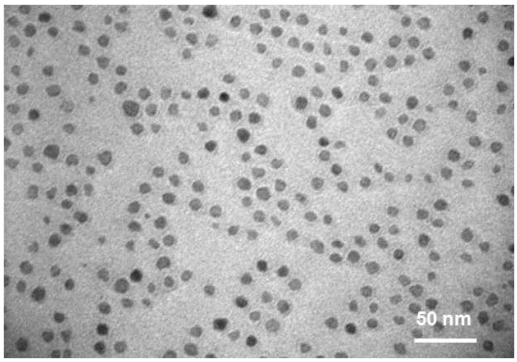

Figure 7.11 Typical TEM image at high NP density showing both size and shape distribution of the NPs' inorganic Fe_3O_4 core

NPs surface functionalization with galactose and PEG

A fraction of these particles was modified with Gal and another fraction with PEG. To this end, 1 mg of PMAO modified NPs were incubated with 5 mg of N-(3-dimethylaminopropyl)-N'-ethylcarbodiimide hydrochloride (EDC) and and 25 μmol of 4-aminophenyl β-D-galactopyranoside or α-methoxy-ω-amino polyethylene glycol (PEG-MW 750 Dalton) in 250 μL of buffer containing 50 mM boric acid and 50 mmol/d^3m sodium borate (SSB) pH 9. After 2 h of reaction at room temperature, the NPs were purified of the ligand excess by washing the sample with phosphate buffered saline (PBS) buffer of pH 7.4 in a centrifugal filter with a 50,000 Da molecular weight cut off membrane (Millipore). The functionalization of the particles is shown schematically in Figure 7.3a.

Phase Analysis Light Scattering (PALS) measurements

Zeta potential measurements were performed on the nanoparticles suspended in deionized water at 25 °C and pH 7.4 on a Zeta PALS instrument (Brookhaven, USA). The given zeta potential values are averages over three measurements (whereat each measurement already forms the average over 10 measurements).

TEM conditions

A single drop (10 µL) of aqueous NP solution (0.1 mg mL^{-1}) was deposited on a copper grid coated with a thin carbon film and let air-dry for several hours at room temperature. TEM analysis was carried out in a JEM-1200EX electron microscope working at 80 kV. The particle size distribution was evaluated from several micrographs using an automatic image analyzer. In order to obtain stable size distribution statistics about 100 particles were taken into consideration for this procedure.

AFM measurements

A drop (2 µL) of aqueous NP solution (0.1 mg mL^{-1}) was deposited on a cleaved mica substrate and let air-dry. Measurements were performed with a commercial AFM (Nanotec Electronica Cervantes FullMode AFM System, http://www.nanotec.es/) operated in the amplitude modulation mode at room temperature and ambient humidity. A second feedback loop was turned on which maintains the phase constant to 90° ("phase-locked loop") by varying the excitation frequency. A monocrystalline silicon cantilever with a force constant of 2.8 Nm^{-1} and a resonance frequency of 75 kHz was used (Nanosensors, Germany).

Agarose gel electrophoresis

0.5% and 2% w/v agarose gels were prepared by mixing 0.5 g and 2 g, respectively, of agarose (A5093, Sigma) with 100 mL of 0.5 x Tris-Borate-EDTA (TBE) buffer (pH 8.7), obtained from diluting 10x TBE buffer which was prepared by mixing 108 g Tris base (93350, Fluka), 55 g boric acid (B7901, Sigma) and 9.3 g EDTA (E6635, Sigma) with H_2O (MiliQ, 18 MΩ) until 1 L was filled. The mixture was heated and let gel in a mold, leaving wells for depositing the suspended NPs. In order to allow for heat dissipation the gel was submerged in the buffer solution with which the horizontal electrophoresis system (Mini-Sub Cell GT, Bio-Rad (electrode spacing of 15 cm)) was filled. Glycerol (1/5 in volume) was added to the aqueous nanoparticle solution of 0.16% w/v (2140 μM Fe_3O_4) and the mixture was loaded in the wells. An electric field of 5 Vcm^{-1} was applied for 105 min (0.5% agarose gel) and 110 min (2% agarose gel).

Dynamic Light Scattering experiments

DLS, also called Photon Correlation Spectroscopy (PCS) or Quasi-Elastic Light Scattering, is a widely used method for measuring the hydrodynamic diameter distribution of suspended particles and their aggregates. In DLS the scattered light intensity fluctuations due to diffusing particles is measured, and the diffusion coefficient of the particles is determined. Knowing solvent viscosity and temperature, the translational diffusion constant is related to the hydrodynamic particle diameter as given by the Stokes-Einstein equation (5.1). The particle size distribution is obtained in terms of light intensity, and can be converted into a volume distribution by applying Mie theory.

Standard DLS only yields correct results if photons are scattered only once in the sample. However, in many systems of biologic relevance multiple scattering occurs. Then, an accurate interpretation with DLS becomes extremely difficult. Variants of DLS have been developed to overcome this problem. Nonetheless, DLS does not allow to distinguish a particular particle fraction in a mixture when the diffusion properties are similar. Here, standard DLS was performed with a commercial instrument, for which the NPs had to be extracted from the gel.

To this end, the gel lane was cut into three pieces and submerged in TBE 0.5x buffer solution. After about one week the majority of the particles had diffused out of the gel into the buffer solution. Measurements were performed with a Zetasizer Nano ZS (Malvern Instruments Ltd, United Kingdom) on a series of dilutions of the diffused particles in deionized water ($T = 25\,^{\circ}\mathrm{C}$). The hydrodynamic particle diameter distribution is given in terms of intensity (Figure 7.7) and number (Figure 7.8).

Author contributions

The essential parts of this chapter have been published as *Transient magnetic birefringence for determining magnetic nanoparticle diameters in dense, highly light scattering media* by Mariana Köber, María Moros, Valeria Grazú, Jesus M. de la Fuente, Mónica Luna and Fernando Briones in Nanotechnology **23** 155501 (2012). Synthesis and functionalizations of the Fe_3O_4 nanoparticles, as well as TEM and zeta potential measurements, have been carried out by María Moros, under the supervision of Valeria Grazú and Jesús M. de la Fuente (Biofunctional Nanoparticles and Surfaces group, Instituto de Nanociencia de Aragón). Gel electrophoresis, *in situ* and *ex situ* TMB experiments, as well as AFM and DLS

measurements were performed by myself, under the supervision of Mónica Luna and Fernando Briones. All authors participated in the discussions as well as in the writing of the manuscript.

Chapter 8

Application to the Detection of Molecular Recognition

In this chapter the application of Transient Magnetic Birefringence (TMB) to the detecion of molecular recognition will be demonstrated on a model system for a lectin-carbohydrate recognition, using glucose (Glc) functionalized magnetite NPs to detect the lectin Concanavalin A (ConA), which is by far the most studied lectin.

8.1 Lectin-carbohydrate recognition

Lectins are proteins which possess at least one domain with a carbohydrate binding site, through which they interact specifically and reversibly with different carbohydrates and glycoconjugates such as glycoproteins (proteins that contain oligosaccharide chains) and glycolipids (lipids with a carbohydrate attached).[170] The binding is non-covalent and may be mediated either through hydrogen bonds, van der Waals forces or ionic bonds. Although lectins were originally identified in plants almost two centuries ago, today we know that they are present in animals, plants,

fungi, bacteria and viruses. Lectins are present in soluble form as well as associated to cells, and their functions are diverse. Animal lectins participate in a series of cellular processes including the intracellular traffic of glycoconjugates, immunologic functions, the regulation of cellular growth and the mediation of endocitosis, amongst others. The principal function of microbial lectins, in turn, is to facilitate the anchorage in the host cell during the tissue colonization and invasion. The biological function of plant lectins is not clear, but diverse functions have been proposed, these being the functions of a storage protein, the participation in the dormancy of the seeds, the defense of pathogens, symbiosis, carbohydrate transport and the elongation of cell walls, amongst others.

Lectin-carbohydrate interactions[171–173] play a predominant role in the initial infection cycles of many pathogenic viruses and bacteria which target carbohydrate molecules on the surface of mammalian cells (the surface of mammalian cells is covered by a dense coating of carbohydrates named *glycocalyx*). For instance, influenza or E. coli use multivalent interactions for tight binding and specific recognition of the cells, which is then followed by the infection of the host cells (Figure 8.1a and b). But not only pathogenic organisms use these kind of interactions, as, for instance, leukocytes going to an inflammation site need to establish simultaneous interactions (Figure 8.1c). Furthermore, carbohydrate-protein interactions, together with protein-protein interactions, are responsible for cellular adhesion. A characteristic feature of the biological interactions where carbohydrates are involved is their extreme low affinity which in most cases is compensated by multivalent presentation of the ligands.

Glyconanoparticles (GNPs) (nanoparticles functionalized with carbohydrates) are excellent sensor probes that allow for a sensitive detection of lectins and the characterization of their affinity to different carbohydrates. They are adecuate both for *in vitro* and *in vivo* studies for an early

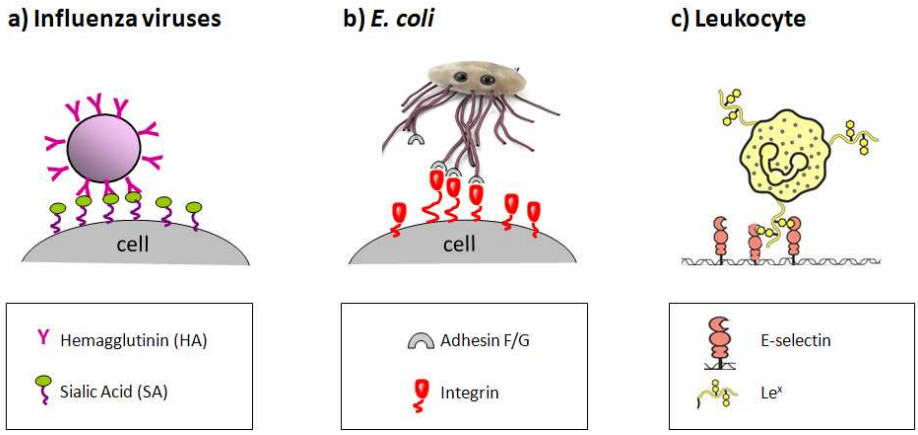

Figure 8.1 Multivalent protein-carbohydrate interactions. Carbohydrate molecules on the surface of mammalian cells are the targets of many pathogenic viruses and bacteria in their initial infection cycles. For instance, influenza or E. coli use multivalent interactions for tight binding and specific recognition of the cells, which is then followed by infection of the host cells. But not only pathogenic organisms use these kind of interactions: leukocytes going to an inflammation site, for instance, need to establish simultaneous interactions. (Figure reprinted with the kind permission of Dr. J. M. de la Fuente)

diagnosis of diseases.[174] By using oligosaccharides commonly found on the plama membrane of animal cells, the interactions with lectins which play an important role in cell-cell recognition can be studied.[175]

8.1.1 Model system: Concanavalin A and glucose functionalized nanoparticles

The lectin used in our studies is Concanavalin A (ConA), a lectin originally extracted from jack-bean seeds, *Canavalia ensiformis* (Figure 8.2). By far, ConA is the most studied lectin, which is why it presents an adequate model system for our studies. Its structure has been described in detail. ConA presents a pH-dependent dimer-tetramer equilibrium: In

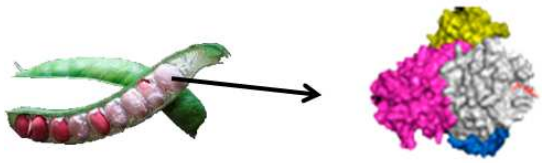

Figure 8.2 Concanavalin A (ConA) is extracted from the jack bean. Right: Tetramer of ConA. The monomers are colored magenta, white, yellow, and blue, respectively.

moderately acidic solutions (pH 4.5 - 5.6), the lectin exists as a dimer with a molecular weight of approximately 52 kDa (in the temperature range of 4 to 31 °C). At pH 7 the quaternary structure is temperature dependent: at 4 °C ConA is present as a dimer, but at 25 °C and above it is primarily a tetramer with a molecular weight of 104 kDa (Figure 8.2).[176]

Concanavalin A selectively binds to certain structures found in various sugars, like α-mannopyranosyl, α-glucopyranosyl and β-glucopyranosyl residues, with descending affinity.[177,178] The affinity to galactose is extremely weak,[177] even though glucose and galactose only differ in the position of a hydroxyl (OH) group (Figure 8.3). ConA is a metalloprotein that requires one Ca^{2+} and one Mn^{2+} cation per subunit for carbohydrate binding;[170] whereby manganese can be substituted by magnesium.[179]

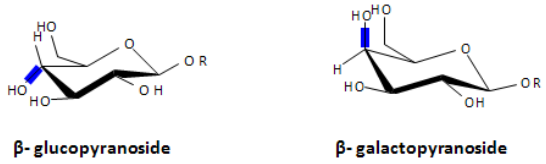

Figure 8.3 Structure of glucose and galactose. Concanavalin A has high affinity to glucose but not to galactose, although glucose and galactose only differ in the position of a hydroxyl group. This demonstrates the high specificity of the lectin-carbohydrate recognition.

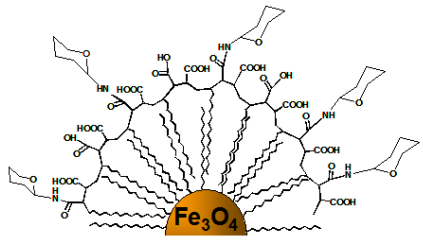

Figure 8.4 Glyconanoparticles (GNPs) used for lectin-carbohydrate recogniton studies. Water solubility is achieved by covering the inorganic core with an amphiphilic polymer shell (PMAO). Particles are rendered biochemically functional with the subsequent modification with galactose (Gal) or glucose (Glc).

The glyconanoparticles (GNPs) used here are water soluble due to the amphiphilic polymer shell (PMAO) covering the inorganic Fe_3O_4 core. Subsequent modification with galactose or glucose determines the recognition of ConA. In Figure 8.4 the magnetic GNPs used here for the lectin-carbohydrate recogniton studies are schematically illustrated.

When ConA is added to a solution containing Glc functionalized NPs, the protein will bind to the NPs (see scheme in Figure 8.5). Here, the binding of ConA to the NP surface is monitored through the aggregate size increase determined by TMB. Since ConA is present either as dimer or tetramer (depending on pH, temperature and buffer), cross-linking between particles may occur. The degree of clustering will mainly depend on the amount of ConA added. On the other hand, with galactose functionalized NPs no recognition is expected.

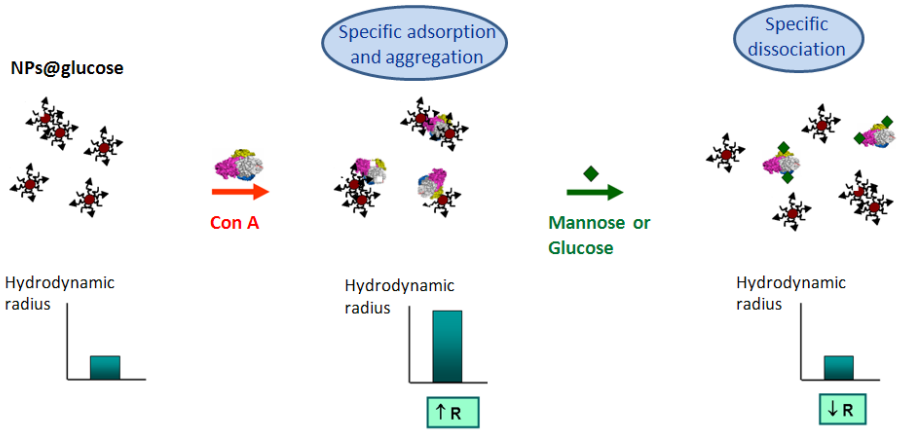

Figure 8.5 Schematic of the performed molecular recognition studies. Upon the addition of ConA to a suspension of Glc functionalized NPs, the specific binding of ConA molecules to the NPs and possible cross-linking of GNPs leads to an increase in the hydrodynamic particle radius. The subsequent addition of an excess of soluble glucose or mannose, which act as inhibitors competing for the union to the ConA, results in the dissociation of the ConA molecules from the NPs, and the hydrodynamic radius decreases to its initial value.

8.2 Interaction strength and cooperativity

The interaction strength is expressed through the dissociation constant K_D, which is the equilibrium constant that measures the propensity of the ConA-glucose complex to separate (dissociate) reversibly into ConA and glucose. The dissociation constant K_D, which has molar units (M), is the concentration of ligand at which the concentration of protein with ligand bound equals the concentration of protein with no ligand bound. The smaller the dissociation constant, the more tightly bound the ligand is, or the higher the affinity between ligand and protein. The dissociation constant for a particular ligand-protein interaction can change significantly with solution conditions (e.g. temperature, pH and salt concentration).

The binding cooperativity, on the other hand, describes how the affinity of ligand molecules to the receptor depends on the ligands that have already bound to this receptor, and is characterized by the Hill coefficient n. For a Hill coefficient above one, positive cooperativity prevails and the binding of one ligand increases the affinity for other ligand molecules to the receptor. On the other hand, if the binding of one ligand to the receptor hinders the binding of further ligands (sterically), cooperativity is negative.

- $n > 1$: Positive cooperativity - the binding of one ligand increases the affinity for other ligand molecules to the receptor
- $n = 1$: Noncooperative binding - the affinity is independent of any ligands that have already bound to the receptor
- $n < 1$: Negative cooperativity - the binding of one ligand decreases the affinity for other ligand molecules to the receptor

When molecules are not freely moving in the solvent but rather attached to NPs, the resulting apparent dissociation constant may differ dramatically from the dissociation constant of the free ligand in solution.[180–184] Cooperative interaction and the accessibility of the binding sites may play a fundamental role, so that, when ligands are fixed on NPs, the apparent dissociation constant depends on the ligand density, length and flexibility of the spacer linking the ligand to the NP, and on NP size.[180,185–187] For ConA and Glc functionalized NPs the apparent dissociation constant K_D has been found to be several orders of magnitude lower (in the order of few tens of nanomolar) than when both are free in solution (for which K_D is 1786 μM).[180,181]

8.3 Molecular recognition experiments

Experiments were performed with the spherical Fe_3O_4 NPs presented before (Chapter 7). For these recognition experiments, however, particles were functionalized with glucose (Glc) and galactose (Gal). Spherical Fe_3O_4 NPs of 6 nm and 8 nm mean diameter (see TEM micrographs in Figure 8.6) were employed. As before, the synthesized NPs were coated with an amphiphilic poly(maleic anhydride-alt-1-octadecene) polymer shell to achieve water solubility. PMAO functionalized Fe_3O_4 NPs are stable in aqueous solutions - currently available data demonstrate stability for over two years.[163] A fraction of these particles was modified subsequently with Gal and another fraction with Glc, as shown schematically in Figure 8.4. The synthesis is described in the Materials and Methods Section 8.7. The area density of Glc molecules on the 6 nm NPs is roughly estimated to 4 molecules per nm^2, and on the 8 nm NPs to 6 molecules per nm^2. ConA was purified as indicated in the Materials and Methods Section 8.7. Since Ca^{2+} and Mg^{2+} (magnesium is a natural substitute for manganese in ConA and other lectins)[179] need to be present for the binding of ConA to the carbohydrates, all measurements were performed in a 10 mM sodium phosphate buffer containing 100 mM of sodium chloride, 1 mM of magnesium chloride and 1 mM of calcium chloride (pH 7).

A first set of experiments was performed with the NPs of 6 nm magnetite core diameter, for which a sufficiently high birefringence signal of approximately 15 mV was achieved with NP suspensions containing 670 μM Fe_3O_4. For the spherical Fe_3O_4 NPs used here it was shown earlier that the birefringence signal mainly comes from anisometric particle aggregates which are detected with high sensitivity (Section 7.2 and Section 7.3). With TMB the mean hydrodynamic radius of the NP

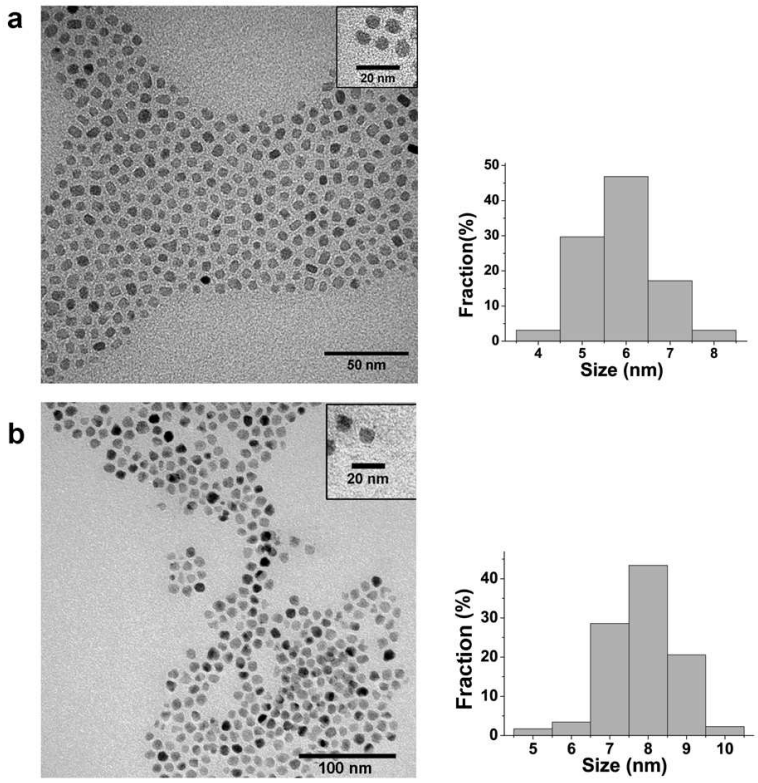

Figure 8.6 Typical TEM image of 6 nm (a) and 8 nm (b) NPs showing both size and shape distribution of the nanoparticles' inorganic Fe_3O_4 core. The particle size distribution shown on the right was determined from about 100 particles.

aggregates is determined to 38.5 nm (Glc functionalized) and 36.5 nm (Gal functionalized).

8.3.1 Aggregation and inhibition dynamics

The reaction dynamics was determined for different ConA concentrations by monitoring the radius increase with time after adding ConA to the nanoparticle suspension (Figure 8.7). Measurements were performed at

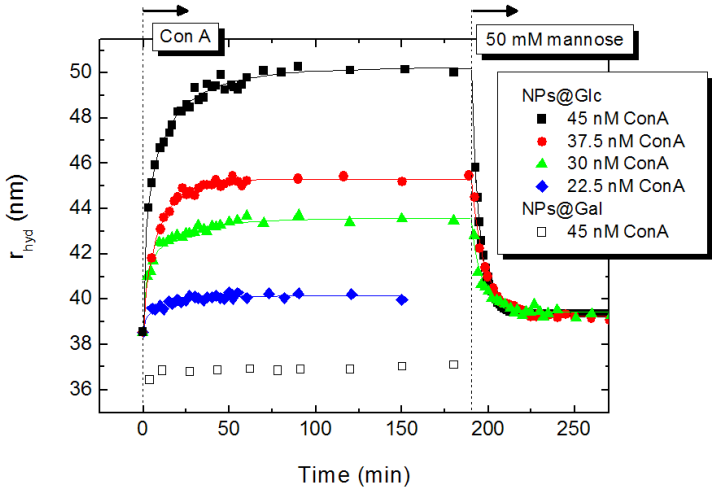

Figure 8.7 Kinetic studies of ConA binding to glucose functionalized Fe_3O_4 NPs. The hydrodynamic radius increase for different ConA concentrations is fitted with a stretched exponential. The subsequent addition of an excess of soluble mannose leads to a practically complete dissociation of the ConA molecules from the NPs, and the hydrodynamic diameter recovers its initial value.

pH 7 and 25 °C, at which ConA is mainly present as a tetramer,[176] presenting four binding sites, one per sub-unit. ConA concentrations in the nanomolar range (22.5 to 45 nM) lead to a significant radius increase of the NPs functionalized with glucose. The size increase is exponential (stretched exponentials have been fitted to the data in Figure 8.7), and equilibrium is reached after two hours (from then on the radius stays constant over time). It should be stressed here that the binding occurred in the presence of Mg^{2+}, which is much slower than in the presence of Mn^{2+}.[179] As expected, the radius of NPs functionalized with galactose remains practically unaffected, due to the ConA specificity.

To determine whether aggregation is reversible and glucose-selective, an excess of soluble glucose or mannose was added to act as inhibitors

and compete for the union to the ConA that had bound to the GNPs. To this end, 50 mM of glucose or mannose were added to the ConA-gluc@NP aggregates and the decrease of the hydrodynamic radius with time was monitored (Figure 8.7 and Figure 8.8). The ConA dissociates practically completely from the NPs: the hydrodynamic radius recovers to 39.2 nm after the addition of 50 mM mannose, and to 40.2 nm after the addition of 50 mM glucose, which is only slightly higher than its initial value of 38.5 nm (a 2% increase in the case of mannose and 4% increase in the case of glucose). By adjusting the exponential decay $r_{\mathrm{hyd}} = r_0 + A\exp(-k_{\mathrm{d}}t)$ to the data points (fit curves are shown in Figure 8.8), the dissociation rate constant k_{d} is obtained. As expected, the dissociation is faster when soluble mannose is added than when the same amount of soluble glucose is added, due to the higher affinity of ConA with mannose than with glucose. Dissociation rate constants differed by a factor three, being $2.7{*}10^{-3}$ s^{-1} under the addition of mannose, and $9.2{*}10^{-4}$ s^{-1} under the addition of glucose (in other words: the average residence times are 6.1 min and 18.0 min, respectively). This threefold increase in dissociation velocity relates well to the four times higher affinity of ConA with mannose than with glucose (the dissociation constants of the free ligand in solution are $K_{\mathrm{D}} = 470$ µM for mannose, and 1786 µM for glucose)[180].

8.3.2 Influence of the measurement in the binding process

For determining the binding dynamics (Figure 8.7), a TMB measurement was performed every 2–3 min. In these measurements, an external pulsed magnetic field is applied during the incubation, which provokes particle rotation and might provoke dipolar interactions. Consequently, TMB measurements during incubation might influence the ConA-NP interaction and NP cross-linking. In order to determine if the measurement influences the binding of ConA to the NPs, a parallel measurement set was

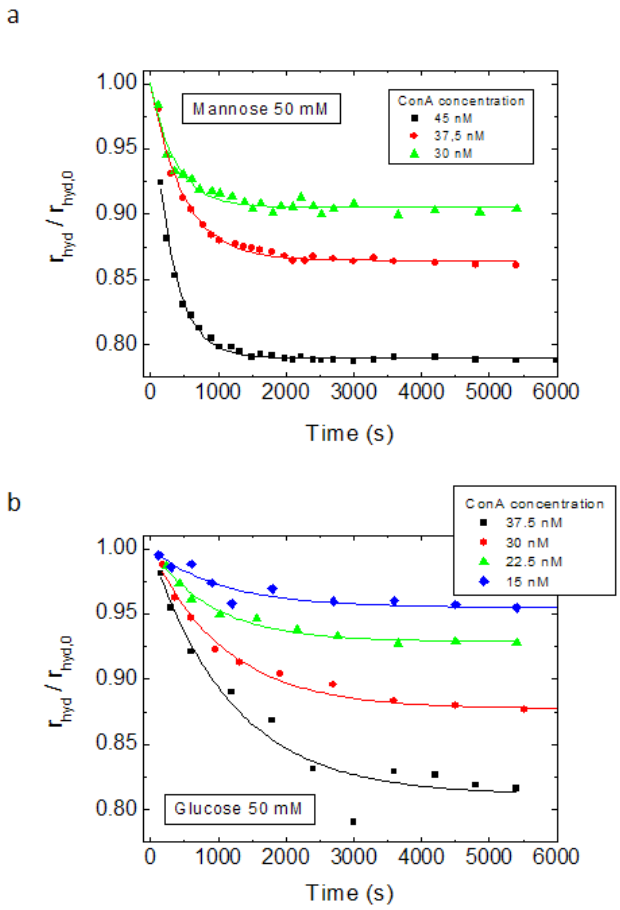

Figure 8.8 Kinetic studies of ConA dissociation from the glucose functionalized Fe_3O_4 NPs, adding (a) 50 mM mannose and (b) 50 mM glucose to samples containing different amounts of ConA. By fitting the exponential decay $r_{\mathrm{hyd}} = r_0 + Ae^{-k_{\mathrm{d}}t}$ (fit curves are shown) the dissociation rate constant k_{d} is obtained. When adding soluble mannose the ConA dissociates three times faster from the NPs than when the same amount of soluble glucose is added.

performed in which the incubation took place at rest. In this case, the first measurement was taken only after equilibrium was reached - two hours after adding ConA (according to Figure 8.7). After two hours of incubation at rest the hydrodynamic radius had effectively reached its equilibrium value, as a few subsequent measurements in the following hour assured. It was found that in this case, when the incubation took place at rest, equilibrium radii were slightly (about 4 nm) higher than when measurements were performed during the incubation period (Figure 8.9). Consequently, the binding of ConA to the NPs is affected by the measurement. Both the binding site at a non-spherical NP aggregate and the orientation of the asymmetric ConA tetramer (with dimensions of 6.7 nm x 11.3 nm x 12.2 nm)[188] influence the aggregate's rotational frictional drag. The application of a pulsed magnetic field leads to the permanent rotation of the particles in solution which favors the binding of ConA molecules on the NPs in a way that minimizes the rotational frictional drag the aggregate experiences. As a consequence, sensitivity is slightly affected by this effect: While the addition of 15 nM ConA (0.75 pmol in a volume of 50 μL) leads to a significant radius increase when the reaction takes place at rest, the same radius increase is only achieved through the addition of about 25 nM ConA when TMB measurements are performed during incubation.

8.3.3 Varying the nanoparticle size

Birefringence that is induced magnetically through the alignment of magnetic particle aggregates is very sensitive to the strength of the magnetic dipolar interaction. This, in turn, depends strongly on the magnetic moments of the particles which for iron oxide NPs decrease significantly with particle size when the particle size falls below 10 nm.[149] A strong dependence of birefringence on the particle size is the consequence.

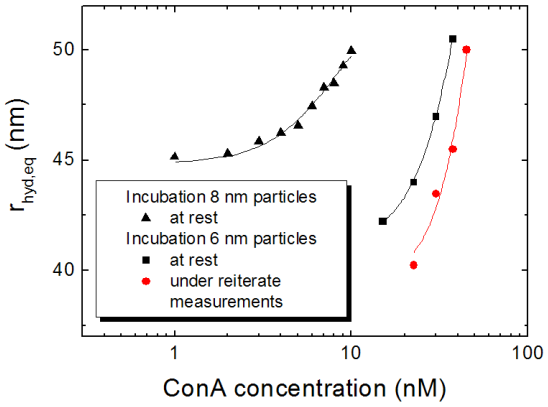

Figure 8.9 Dependence of the equilibrium hydrodynamic radius $r_{\mathrm{hyd,eq}}$ on the ConA concentration. Equilibrium radii are about 4 nm smaller when the incubation is carried out under reiterate measurement and not at rest, probably due to the optimization of both the binding site at a non-spherical NP aggregate and the ConA orientation to reduce the aggregate's rotational frictional drag. A comparison of the results for NPs of 8 nm and 6 nm iron oxide diameter shows that higher sensitivity is achieved with particles of larger diameter, attributed to higher magnetic moments that larger particles present, resulting in a stronger magnetic dipolar interaction and a higher torque to align the particles with the magnetic field.

This effect has been observed in the experiments: When the NPs presented a magnetite nucleus of 8 nm instead of 6 nm, birefringence was five times higher (note that a different degree of aggregation may also contribute to the differences in birefringence, since only the fraction of anisometric aggregates contributes to the birefringence signal). Consequently, the NPs with magnetite nucleus of 8 nm were used at five times lower NP concentrations (130 µM Fe_3O_4), which directly traduced into a reduction of the detection limit from 15 nM to only 3 nM for ConA (see Figure 8.9). This is the experimental proof that the detection limit depends sensitively on the size of the magnetite NPs. Particle shape and aggregation state

also play a key role for this technique (see Chapter 7 and Reference [37]). Thus, by designing the NPs adequately (using anisometric NPs or assuring dimer formation of all NPs), sensitivity can be further increased significantly. Nonetheless, even without further improvements on the NP design, the detection limit is comparable to that of the popular analytic biochemistry assay ELISA[189,190] and lower than that obtained with colorimetric assays based on the aggregation of Au and Ag GNPs (detection limit > 9 nM).[191–194] Comparable detection limits have also been observed with a nanostructured impedimetric sensor.[195] Only with more complex methodologies significantly lower detection limits are obtained.[196–198]

8.4 Binding model

The way the particle radius increases with ConA concentration (Figure 8.9) gives us information on strength and cooperativity of the interaction. To this end, the particle size increase has to be related to the binding of ConA molecules. Let N_{ConA} be the number of ConA molecules that, in equilibrium, is bound in average to a NP cluster at a certain ConA concentration [ConA], and $N_{\mathrm{ConA,max}}$ the maximum number of ConA molecules that can bind on an average NP cluster. The increase of N_{ConA} with [ConA] is described by the Hill equation[199]

$$\frac{N_{\mathrm{ConA}}}{N_{\mathrm{ConA,max}}} = \frac{1}{1 + \left(\frac{K_{\mathrm{D}}}{[\mathrm{ConA}]}\right)^{n}}, \tag{8.1}$$

where K_{D} is the apparent dissociation constant, and n the Hill coefficient. At pH 7 and 25 °C ConA is mainly present as a tetramer,[176]

so that the binding of a ConA molecule to a NP can result in cross-linking of several NPs. At low ConA concentrations, however, cross-linking is not significant. Then, the aggregate volume V_{aggreg} is related to the binding of N_{ConA} ConA molecules by[159]

$$V_{\mathrm{aggreg}}\left(N_{\mathrm{ConA}}\right) = V_{\mathrm{NP}} + N_{\mathrm{ConA}} V_{\mathrm{ConA}}, \tag{8.2}$$

where V_{NP} is the NP volume before adding ConA and V_{ConA} the volume of a ConA molecule. Calculating the effective radius r of a hypothetic sphere $r = (\frac{3}{4\pi}V)^{1/3}$ and substituting equation (8.1) into equation (8.2) yields the dependence of the hydrodynamic radius increase on the ConA concentration,

$$r_{\mathrm{aggreg}}\left([\mathrm{ConA}]\right) = r_{\mathrm{NP}} \left(1 + \left(\frac{V_{\mathrm{ConA}}}{V_{\mathrm{NP}}} \right) \frac{N_{\mathrm{ConA,max}}}{1 + \left(\frac{K_{\mathrm{D}}}{[\mathrm{ConA}]} \right)^{n}} \right)^{1/3}. \tag{8.3}$$

The experimental data is described well with this model (fit curves are shown in Figure 8.9), and values for V_{NP} , N_{ConA} and V_{ConA} were close to measured and calculated ones. On the other hand, a model assuming cross-linking, where the number of NPs incorporated into the aggregates increases linearly with the number of bound ConA molecules, $V_{\mathrm{aggreg}}\left(N_{\mathrm{ConA}}\right) = V_{\mathrm{NP}} + N_{\mathrm{ConA}}(N_{\mathrm{NP}} V_{\mathrm{NP}} + V_{\mathrm{ConA}})$, only adjusted well to the data when the number of cross-linked particles N_{NP} was practically zero. For the 8 nm particles an apparent dissociation constant K_{D} of 14 nM was determined and a Hill coefficient n of 2.0. The maximum number of ConA molecules that can bind (N_{max}) was determined to 234 (the calculated upper value is 276). Interestingly, for the 6 nm particles

the apparent dissociation constant is eight times higher, approximately 80 nM, independently of whether measurements are performed during incubation or not. Consequently, the interaction strength is lower for the 6 nm particles, which - taking into account the importance of multivalency in carbohydrate-protein interactions - might be related to the lower density of glucose molecules on the NP surface (4 molecules per nm^2 on the 6 nm NPs vs 6 molecules per nm^2 on the 8 nm NPs). The Hill coefficient is higher for the 6 nm NPs, and shows some variation depending on whether measurements are performed during incubation ($n = 3.5$) or not ($n = 2.7$). Recognition experiments based on water proton relaxation times performed with the same 6 nm particles resulted in similar values, with an apparent dissociation constant of 78 nM and a Hill coefficient of 3.4.[200] Other research groups have also obtained apparent dissociation constants in the order of few tens of nanomolar with colorimetric techniques,[180,181] and for mannose functionalized NPs (40 nm in diameter) the Hill coefficient was determined to 2.[190]

8.5 Suitability for biosensing

Depending on the particular application, a biosensor must meet specific demands on sensitivity, selectivity, cost, detection speed, portability of the device and parallel detection of several analytes. In the following, a brief evaluation of TMB regarding these aspects is given.

Sensitivity Here, experiments were performed on a model system to test the technique, since ConA represents a lectin that is well characterized. However, the detection of ConA does not have an application in biomedicine. Therefore, the detection limit of 3 nM of ConA (0.15 pmol in 50 µl) cannot be set into relation with the required sensitivity. As

a next step, the method could be tested for detecting Erythropoietin (EPO), a glycoprotein hormone that controls red blood cell production ("erythropoiesis"). Then, the sensitivity can be evaluated as to the quantity of EPO that is detectable in human plasma.

Detection speed The time to perform one measurement can be computed with a few minutes (once the analyte has been prepared, if necessary). The analyte is added to the cuvette containing nanoparticle solution and the cuvette is inserted into the device. The measurement as such is performed in a few seconds and the result is obtained immediately (the evaluation can be automatized), since no extra washing steps or further processes for signal enhancement are necessary. The detection speed is rather limited by the reaction dynamics.

Portability At the moment, the TMB setup is mounted on a table without considerations for saving space (Figure 6.6). However, dimensions can be reduced significantly. Using a laser diode and a compact arrangement of the components, the TMB setup can be a portable table-top device.

8.6 Conclusions

On the basis of the model system ConA-Glc the benefits and drawbacks to use TMB for biosensing were explored, using Glc functionalized magnetite NPs of different sizes (6 nm and 8 nm). TMB results to be a sensitive technique to detect molecular recognition and measure both binding and inhibition dynamics. The detection limit was found to be in the nanomolar range and depended sensitively on the size of the magnetite NPs: it

was only 3 nM (0.15 pmol in 50 µl) for the 8 nm particles, but 15 nM (0.75 pmol in 50 µl) for the 6 nm particles. A further increase in sensitivity through tailoring NP size, shape and/or aggregation state is expected. In addition to the high sensitivity in the nanomolar range, the technique offers advantages such as ease of operation (detection in suspension and no labeling of the analyte), low costs and high measurement speed. By modeling how the aggregate diameter increases with ConA concentration the apparent dissociation constant and Hill coefficient of the reaction could be determined. The apparent dissociation constant was 10 nM (for the 8 nm particles) and 80 nM (for the 6 nm particles), and the Hill coefficient was 2 and 2.8, respectively. Consequently, the binding is cooperative. The results are in agreement with values that have been determined using established techniques. Measurements performed during the incubation period influence the binding - final aggregate sizes are smaller. This effect is possibly due to an optimization of the site at the non-spherical NP (aggregate) at which the ConA binds and the orientation of the asymmetric ConA molecules, to reduce rotational frictional drag. However, the apparent dissociation constant has not been affected by this effect. As expected, nanomolar concentrations of ConA do not produce a significant diameter increase when NPs are functionalized with galactose.

8.7 Materials and Methods

NP synthesis and ConA purification have been performed by collaborating groups, and shall be briefly described here for completeness.

Nanoparticle synthesis and functionalization

NP synthesis and functionalization was performed by María Moros (group of Dr. J. M. de la Fuente, Instituto de Nanociencia de Aragón).

Synthesis of 6 nm and 8 nm iron oxide nanoparticles Monodisperse iron oxide nanoparticles of 6 nm in diameter were synthesized following the seed-mediated growth method described by Sun.[161] Several studies performed earlier have shown that the iron oxide of these NPs is Fe_3O_4.[138] First, 4 nm Fe_3O_4 NP seeds were synthesized by mixing and stirring under a flow of argon, $Fe(acac)_3$ (0.71 g), 1,2-hexadecanediol (2.58 g), oleic acid (2 mL) and oleylamine (2 mL), solubilized in phenyl ether (20 mL). Unless otherwise stated, all reagents were purchased from Sigma Aldrich. The mixture was heated to 200 for 2 h and afterwards heated to reflux (265 °C) under argon atmosphere for 1 h. The mixture was allowed to cool to room temperature and the NPs were washed by adding ethanol and collecting them with a magnet and redispersed in hexane three times. NPs were redispersed in 10 mL hexane containing 50 μL of oleic acid and 50 μL of oleylamine. In order to obtain 6 nm NPs, 80 mg of the 4 nm Fe_3O_4 seeds in hexane were added to a mixture containing $Fe(acac)_3$ (0.71 g), 1,2-hexadecanediol (2.58 g), oleic acid (0.5 mL), oleylamine (0.5 mL) and 20 mL of phenyl ether. The mixture was heated to 100 °C for 30 min to remove the hexane and then to 200 °C for 1 h. Under argon atmosphere the mixture was further heated to reflux (265 °C) for another hour. The mixture was allowed to cool at room temperature by removing the heat source and as after the first growth step, they were precipitated with ethanol and resuspended in hexane. NPs of 6 nm were precipitated with ethanol and weighed once completely dry.

The synthesis of 8 nm particles is analog, but the solvent phenyl ether was substituted by benzyl ether which has a higher boiling point. Therefore, the mixture was heated to reflux at 298 °C instead of 265 °C. In this case, the seeds are of 6 nm, and the repetition of the growth process yields 8 nm particles.

It should be noted that particles employed in Chapter 7 were synthesized by the same procedure, using phenyl ether, but in a different laboratory. In this case, the particles resulted to be 8 nm in diameter instead of 6 nm as reported here and in the literature.[161] The reason for this difference could not be clearly determined, but the use of different laboratory equipment such as fume hoods, vacuum lines and heating mantles may lead to changes in various parameters like the velocity of the temperature rise, the agitation velocity and argon flux velocity, which in turn give rise to these differences.

Water solubilisation of hydrophobic magnetic nanoparticles 250 mg of poly(maleic anhydride-alt-1-octadecene) (PMAO) was added to a flask containing 200 mL of chloroform. After the polymer was dissolved under magnetic stirring, 20 mg of the NPs were added and the mixture was gently stirred for two hours at 25 °C. Afterwards, the solvent was removed under vacuum and few millilitres of chloroform were added. NPs were then resuspended in 20 mL of NaOH 0.05 M and the sample was shaken at 60 °C in order to speed up the complete evaporation of chloroform. At this point the solution became clear as NPs were completely transferred into water. NPs were then filtered on syringe filters of 0.22 µm. The NP solution was centrifuged two times at 25 000 rpm for 2 h to remove the excess unbound polymer molecules. The NPs at the bottom were recovered and redispersed in water.

NPs surface functionalization with carbohydrates Glucose and galactose NPs were obtained by incubating 1 mg of NPs with 3 mg of N-(3-dimethylaminopropyl)-N'-ethylcarbodiimide hydrochloride (EDC) and 25 μmol of 4-aminophenyl β-D-glucopyranoside or 4-aminophenyl β-D-galactopyranoside in 250 μL of SSB buffer pH 9 (50 mM of boric acid and 50 mM of sodium borate). After 2 h of incubation the ligand excess was removed by washing the NPs with phosphate buffered saline (PBS) pH 7.4 in a centrifugal filter with a 100,000 Da molecular weight cut off membrane (Millipore).

Concanavalin A purification

ConA purification was carried out by Prof. L. Franco Fraguas (Universidad de Uruguay).

The purification of the lectin was done as described in Reference [201]. Essentially, the jack bean extract was prepared as followed: the commercial jack bean meal (Sigma) was extracted with 0.5 M NaCl (1 mM $CaCl_2$, 1 mM $MnCl_2$) during 4 h under magnetic stirring. The pH was determined and adjusted to 4.5 with acetic acid and the extract was centrifuged during 15 min at 13 000 rpm at 4 °C. The pH of the extract was adjusted back to the original value and ammonium sulfate 75% saturation was added to the clear supernatant. The mixture was kept overnight at 4 °C and was then centrifuged as above. The pellet was dissolved in a minimal volume of 0.1 M sodium acetate buffer (1 M NaCl, 1 mM $CaCl_2$, 1 mM $MnCl_2$) pH 6.0 (adsorption buffer) and used for the purification of ConA by affinity chromatography using a column packed with mannosyl-Sepharose. This adsorbent was prepared as described in Reference [201].

The purification of the lectin was performed as follows: the mannosyl-Sepharose gel was placed into a column (6.0 ml packed gel) and equilibrated with the adsorption buffer. A volume of 13 ml of the jack bean meal extract was applied to the column at a flow rate of 20 ml h^{-1}. The column was extensively washed with adsorption buffer and elution was performed with 0.1 M methyl mannoside in adsorption buffer. The eluted lectin was extensively dialyzed against distilled water and lyophilized. Finally, the ConA concentration was determined spectrophotometrically at 280 nm, using an extinction coefficient of 11.4.[202]

Author contributions

Nanoparticles have been synthesized and functionalized by María Moros, under the supervision of Valeria Grazú and Jesús M. de la Fuente (Biofunctional Nanoparticles and Surfaces group, Instituto de Nanociencia de Aragón). Laura Franco Fraguas (Cátedra de Bioquímica, Universidad de la República de Uruguay) has purified the ConA lectin. I have performed the molecular recognition experiments using TMB, under the supervision of Mónica Luna and Fernando Briones.

Conclusions and Perspectives

The general field of intermolecular, hydrodynamic and capillary interactions at the nanoscale is a present hot topic, due to its relevance in biological and biomedical applications. The two aspects that we have approached in this thesis, apparently unconnected, have contributed with interesting results in the understanding of such interactions.

- Our studies have shown that capillary adhesion between two nanometric bodies with hydrophilic surfaces depends strongly on the objects' geometry at the contact point. Particularly surprising is the experimental observation that capillary adhesion may even decrease with relative humidity. In concordance with theoretical results, this counterintuitive behavior is found at sharp truncated objects with a narrow contact region.

- The dissipation due to adhesion hysteresis in dynamic Atomic Force Microscopy has been studied. Results suggest that the experimentally accessible power dissipation cannot always be directly related to physicochemical sample properties. Rather the cantilever dynamics has to be taken into account, since contacts involving adhesion hysteresis may occur only occasionally.

- Our final objective to develop a nanoparticle based molecular recognition biosensor has led us to the implementation of an original experimental setup to detect Transient Magnetic Birefringence (TMB).

Our setup has been successfully used to determine hydrodynamic diameter distributions of colloidal magnetic nanoparticles. Instrument development involved the design and optimization of specific electronics to generate sufficiently intense magnetic field pulses in small coils and a very small sample volume of the order of 50 µl.

- First proof-of-principle experiments demonstrate that TMB is capable of selectively detecting the presence or formation of particle dimers, distinguishing it from a background due to monomers, isotropic aggregates and large optical scattering from the surrounding media. This capability complements other techniques such as gel electrophoresis. What is more, the technique can be applied *in situ* to particles drifting in an electrophoresis gel. This shows that it is possible, in principle, to determine the hydrodynamic mobility of magnetic nanoparticles optically even in a dense gel which mimics the internal medium of a living cell. As originally proposed, molecular recognition can be detected through the formation of nanoparticle dimers, if unspecific nanoparticle aggregation can be practically excluded.

- Moreover, the usefulness of this development has been tested in a practical case in the biochemistry field: the binding and subsequent inhibition of Concanavalin A to glucose functionalized nanoparticles. Interaction strength and binding cooperativity were determined, applying a simple model of biomolecule binding to the nanoparticles.

The continuation of this work includes the following aspects:

- To explore its potential, Transient Magnetic Birefringence can be applied to further biomedical applications. For example, interactions of nanoparticles with live cells could be studied by means of the rotational particle mobility. Further experiments are planned to

detect biomolecules of current interest, such as *erythropoietin* (EPO) (a glycoprotein hormone that controls red blood cell production) and DNA of the adenovirus.

- Further instrument development can be carried out, such as the miniaturization of the setup to obtain a portable device and its integration into a confocal optical microscope.

Conclusiones y Perspectivas

El amplio campo de las interacciones intermoleculares, hidrodinámicas y capilares en la nanoescala está de actualidad debido a su relevancia en aplicaciones biológicas y biomédicas. Los dos aspectos que hemos abordado en esta tesis han contribuido con resultados interesantes a la comprensión de tales interacciones.

- Nuestros estudios han demostrado que la adhesión capilar entre dos objetos nanométricos con superficies hidrófilas depende en gran medida de la geometría de los objetos en el punto de contacto. Especialmente sorprendente es la observación experimental de que la adhesión capilar puede incluso decrecer con la humedad relativa. En concordancia con resultados teóricos, este comportamiento, aparentemente contrario al sentido común, ocurre para objetos afilados truncados con un área de contacto estrecho.

- Los resultados del estudio de la disipación debida a la histéresis de adhesión en el modo dinámico de la Microscopía de Fuerzas Atómicas sugieren que la potencia disipada, experimentalmente accesible, no está siempre directamente relacionada con las propiedades fisicoquímicas de la muestra. Para ciertas condiciones de operación del microscopio, es fundamental tener en cuenta la dinámica del cantiléver dado que los contactos que implican histéresis de adhesión pueden ocurrir sólo ocasionalmente.

- El objetivo final de desarrollar un biosensor de reconocimiento molecular basado en nanopartículas nos ha llevado a implementar un montaje experimental original para detectar la birrefringencia magnética transitoria (TMB). Nuestro montaje se ha utilizado con éxito para determinar distribuciones de diámetro hidrodinámico de nanopartículas magnéticas coloidales. El desarrollo instrumental ha incluido el diseño y la optimización de electrónica específica para generar pulsos de campos magnéticos suficientemente intensos en bobinas pequeñas y un volumen de muestra muy reducido del orden de 50 µl.

- Los experimentos demuestran la capacidad de TMB para detectar selectivamente la presencia o formación de dímeros de partículas, distinguiéndola de un fondo formado por monómeros, agregados isótropos y una alta dispersión óptica del medio. Esa capacidad complementa otras técnicas como electroforesis en gel. Además, la técnica puede ser aplicada *in situ* a partículas que flotan en las cavidades de un gel de electroforesis. Esto demuestra que es posible, en principio, determinar ópticamente la movilidad hidrodinámica de nanopartículas magnéticas incluso en un gel denso que mimetiza el medio interno de una célula viva. Hemos podido confirmar la hipótesis propuesta desde el principio: el reconocimiento molecular puede ser detectado a través de la formación de dímeros de nanopartículas, siempre y cuando una agregación inespecífica de nanopartículas pueda ser prácticamente excluida.

- Además, la utilidad de este desarrollo ha sido demostrada en un caso práctico en el campo de la bioquímica: la unión y subsecuente inhibición de la Concanavalina A a nanopartículas funcionalizadas con glucosa. Se ha determinado la fuerza de interacción y la

cooperatividad en la unión aplicando un modelo simple para la unión de las biomoléculas a las nanopartículas.

La continuación del trabajo incluye los siguientes aspectos:

- La birrefringencia magnética transitoria puede ser interesante para otras aplicaciones biomédicas. Por ejemplo, las interacciones entre nanopartículas y células vivas podrían ser estudiadas a través de la movilidad rotacional de las partículas. En nuestro plan de trabajo se encuentra además la detección de biomoléculas de interés actual, como la eritropoyetina (EPO) (hormona glicoproteína que controla la producción de glóbulos rojos) y el ADN del adenovirus.
- Sería interesante continuar el desarrollo de esta técnica mediante su miniaturización para obtener un dispositivo portátil, y posiblemente incluso integrándolo en un microscopio óptico confocal.

Colophon

This manuscript was typesetted using the LaTeX 2_ε "hepthesis" class.[203]

Bibliography

[1] J. A. Dagata, J. Schneir, H. H. Harary, C. J. Evans, M. T. Postek, and J. Bennett, *Modification of hydrogen-passivated silicon by a scanning tunneling microscope operating in air*, Applied Physics Letters **56**, 2001 (1990).

[2] R. D. Piner, J. Zhu, F. Xu, S. Hong, and C. A. Mirkin, *"Dip-Pen" Nanolithography*, Science **283**, 661 (1999).

[3] P. Eaton *et al.*, *Glyconanoparticle - DNA Interactions: An Atomic Force Microscopy Study*, IEEE Transactions on NanoBioscience **6**, 309 (2007).

[4] M. Luna, J. Colchero, and A. M. Baró, *Intermittent contact scanning force microscopy: The role of the liquid necks*, Applied Physics Letters **72**, 3461 (1998).

[5] L. Zitzler, S. Herminghaus, and F. Mugele, *Capillary forces in tapping mode atomic force microscopy*, Physical Review B **66**, 155436 (2002).

[6] E. Sahagún, P. García-Mochales, G. M. Sacha, and J. J. Sáenz, *Energy dissipation due to capillary interactions: Hydrophobicity maps in force microscopy*, Physical Review Letters **98**, 176106 (2007).

[7] U. Landman, W. D. Luedtke, N. A. Burnham, and R. J. Colton, *Atomistic Mechanisms and Dynamics of Adhesion, Nanoindentation, and Fracture*, Science **248**, 454 (1990).

[8] R. Garcia, C. J. C. J. Gómez, N. F. Martinez, S. Patil, C. Dietz, and R. Magerle, *Identification of Nanoscale Dissipation Processes by Dynamic Atomic Force Microscopy*, Physical Review Letters **97**, 016103 (2006).

[9] H.-J. Butt and M. Kappl, *Normal capillary forces*, Advances in Colloid and Interface Science **146**, 48 (2009).

[10] J. Israelachvili, *Intermolecular and Surface Forces* (Academic, San Diego, 1991).

[11] B. Bhushan, *Nanotribology and nanomechanics in nano/biotechnology*, Philosophical Transactions of the Royal Society A: Mathematical, Physical & Engineering Sciences **366**, 1499 (2008).

[12] T. Thundat, X. Y. Zheng, G. Y. Chen, S. L. Sharp, R. J. Warmack, and L. J. Schowalter, *Characterization of atomic force microscope tips by adhesion force measurements*, Applied Physics Letters **63**, 2150 (1993).

[13] M. Binggeli and C. M. Mate, *Influence of capillary condensation of water on nanotribology studied by force microscopy*, Applied Physics Letters **65**, 415 (1994).

[14] C. Gao, *Theory of menisci and its applications*, Applied Physics Letters **71**, 1801 (1997).

[15] X. D. Xiao and L. M. Qian, *Investigation of humidity-dependent capillary force*, Langmuir **16**, 8153 (2000).

[16] M. Y. He, A. S. Blum, D. E. Aston, C. Buenviaje, R. M.

Overney, and R. Luginbuhl, *Critical phenomena of water bridges in nanoasperity contacts*, Journal of Chemical Physics **114**, 1355 (2001).

[17] O. H. Pakarinen *et al.*, *Towards an accurate description of the capillary force in nanoparticle-surface interactions*, Modelling and Simulation in Materials Science and Engineering **13**, 1175 (2005).

[18] D. B. Asay and S. H. Kim, *Effects of adsorbed water layer structure on adhesion force of silicon oxide nanoasperity contact in humid ambient*, Journal of Chemical Physics **124**, 174712 (2006).

[19] A. Fukunishi and Y. Mori, *Adhesion force between particles and substrate in a humid atmosphere studied by atomic force microscopy*, Advanced Powder Technology **17**, 567 (2006).

[20] M. Paajanen, J. Katainen, O. H. Pakarinen, A. S. Foster, and J. Lahtinen, *Experimental humidity dependency of small particle adhesion on silica and titania*, Journal of Colloid and Interface Science **304**, 518 (2006).

[21] A. A. Feiler, J. Stiernstedt, K. Theander, P. Jenkins, and M. W. Rutland, *Effect of capillary condensation on friction force and adhesion*, Langmuir **23**, 517 (2007).

[22] M. Farshchi-Tabrizi, M. Kappl, and H.-J. Butt, *Influence of humidity on adhesion: An atomic force microscope study*, Journal of Adhesion Science and Technology **22**, 181 (2008).

[23] Q. A. Pankhurst, N. K. T. Thanh, S. K. Jones, and J. Dobson, *Progress in applications of magnetic nanoparticles in biomedicine*, Journal of Physics D-Applied Physics **42**, 15 (2009).

[24] A. K. Gupta and M. Gupta, *Synthesis and surface engineering of*

iron oxide nanoparticles for biomedical applications, Biomaterials **26**, 3995 (2005).

[25] T. Vo-Dinh and B. Cullum, *Biosensors and biochips: advances in biological and medical diagnostics*, Fresenius' Journal of Analytical Chemistry **366**, 540 (2000).

[26] X. Zhang, Q. Guo, and D. Cui, *Recent Advances in Nanotechnology Applied to Biosensors*, Sensors **9**, 1033 (2009).

[27] A. Ranzoni, J. J. H. B. Schleipen, L. J. van Ijzendoorn, and M. W. J. Prins, *Frequency-Selective Rotation of Two-Particle Nanoactuators for Rapid and Sensitive Detection of Biomolecules*, Nano Letters **11**, 2017 (2011).

[28] C. F. Hayes and S. R. Hwang, *Observation of magnetically induced polarization in a ferrofluid*, Journal of Colloid and Interface Science **60**, 443 (1977).

[29] H. W. Davies and J. P. Llewellyn, *Magnetic birefringence of ferrofluids. II. Pulsed field measurements*, Journal of Physics D-Applied Physics **12**, 1357 (1979).

[30] J. C. Bacri, R. Perzynski, D. Salin, and J. Servais, *Magnetic transient birefringence of ferrofluids: particle size determination*, Journal De Physique **48**, 1385 (1987).

[31] P. Goldberg, J. Hansford, and P. J. van Heerden, *Polarization of Light in Suspensions of Small Ferrite Particles in a Magnetic Field*, Journal of Applied Physics **42**, 3874 (1971).

[32] C. Wilhelm *et al.*, *Binding of biological effectors on magnetic nanoparticles measured by a magnetically induced transient birefringence experiment*, Physical Review E **65**, 9 (2002).

[33] E. Romanus, C. Groß, G. Glöckl, P. Weber, and W. Weitschies, *Determination of biological binding reactions by field-induced birefringence measurements*, Journal of Magnetism and Magnetic Materials **252**, 384 (2002).

[34] K. Aurich, S. Nagel, E. Heister, and W. Weitschies, *Affinity analysis for biomolecular interactions based on magneto-optical relaxation measurements*, Nanotechnology **19**, 505102 (2008).

[35] L. Lartigue *et al.*, *Nanomagnetic Sensing of Blood Plasma Protein Interactions with Iron Oxide Nanoparticles: Impact on Macrophage Uptake*, ACS Nano **6**, 2665 (2012).

[36] P. C. Scholten, *The origin of magnetic birefringence and dichroism in magnetic fluids*, Ieee Transactions on Magnetics **16**, 221 (1980).

[37] M. Xu and P. J. Ridler, *Linear dichroism and birefringence effects in magnetic fluids*, Journal of Applied Physics **82**, 326 (1997).

[38] A. Verma and F. Stellacci, *Effect of Surface Properties on Nanoparticle-Cell Interactions*, Small **6**, 12 (2010).

[39] L. Bergström, *Hamaker constants of inorganic materials*, Advances in Colloid and Interface Science **70**, 125 (1997).

[40] P. D. Ashby, L. Chen, and C. M. Lieber, *Probing Intermolecular Forces and Potentials with Magnetic Feedback Chemical Force Microscopy*, Journal of the American Chemical Society **122**, 9467 (2000).

[41] S. Hudlet, M. Saint Jean, B. Roulet, J. Berger, and C. Guthmann, *Electrostatic forces between metallic tip and semiconductor surfaces*, Journal of Applied Physics **77**, 3308 (1995).

[42] A. Gil, J. Colchero, J. Gómez-Herrero, and A. M. Baró, *Electrostatic*

force gradient signal: resolution enhancement in electrostatic force microscopy and improved Kelvin probe microscopy, Nanotechnology **14**, 332 (2003).

[43] S. Sadewasser, P. Carl, T. Glatzel, and M. C. Lux-Steiner, *Influence of uncompensated electrostatic force on height measurements in non-contact atomic force microscopy*, Nanotechnology **15**, S14 (2004).

[44] Y. Martin and H. K. Wickramasinghe, *Magnetic imaging by "force microscopy" with 1000 Å resolution*, Applied Physics Letters **50**, 1455 (1987).

[45] J. J. Sáenz *et al.*, *Observation of magnetic forces by the atomic force microscope*, Journal of Applied Physics **62**, 4293 (1987).

[46] S. Schreiber *et al.*, *Magnetic force microscopy of superparamagnetic nanoparticles*, Small **4**, 270 (2008).

[47] C. D. Frisbie, L. F. Rozsnyai, A. Noy, W. M. S., and C. M. Lieber, *Functional Group Imaging by Chemical Force Microscopy*, Science **265**, 2071 (2000).

[48] Y. Sugimoto *et al.*, *Chemical identification of individual surface atoms by atomic force microscopy*, Nature **446**, 64 (2007).

[49] F. J. Giessibl, *Forces and frequency shifts in atomic-resolution dynamic-force microscopy*, Physical Review B **56**, 16010 (1997).

[50] A. Buldum, S. Ciraci, C. Y. Fong, and J. S. Nelson, *Interpretation of long-range interatomic force*, Physical Review B **59**, 5120 (1999).

[51] U. Hartmann, *van der Waals interactions between sharp probes and flat sample surfaces*, Physical Review B **43**, 2404 (1991).

[52] F. Ohnesorge and G. Binnig, *True Atomic Resolution by Atomic*

Force Microscopy Through Repulsive and Attractive Forces, Science **260**, 1451 (1993).

[53] H. Hertz, *Über die Berührung fester elastischer Körper*, Journal für die reine und angewandte Mathematik **92**, 156 (1881).

[54] U. D. Schwarz, *A generalized analytical model for the elastic deformation of an adhesive contact between a sphere and a flat surface*, Journal of Colloid and Interface Science **261**, 99 (2003).

[55] K. L. Johnson, K. Kendall, and A. D. Roberts, *Surface Energy and the Contact of Elastic Solids*, Proceedings of the Royal Society A **324**, 301 (1971).

[56] B. V. Derjaguin, V. M. Muller, and Y. P. Toporov, *Effect of contact deformations on the adhesion of particles*, Journal of Colloid and Interface Science **53**, 314 (1975).

[57] E. Sahagún, *Sobre las Fuerzas Capilares en Microscopía de Fuerzas: Adhesión y Disipación*, PhD thesis, 2011.

[58] M. A. Henderson, *The interaction of water with solid surfaces: fundamental aspects revisited*, Surface Science Reports **46**, 1 (2002).

[59] J. Grobelny, N. Pradeep, D.-I. Kim, and Z. C. Ying, *Quantification of the meniscus effect in adhesion force measurements*, Applied Physics Letters **88**, 091906 (2004).

[60] T. Bouhacina, B. Desbat, and J. P. Aimé, *FTIR spectroscopy and nanotribological comparative studies: influence of the adsorbed water layers on the tribological behaviour*, Tribology Letters **9**, 111 (2000).

[61] L. Sirghi, R. Szoszkiewicz, and E. Riedo, *Volume of a nanoscale water bridge*, Langmuir **22**, 1093 (2006).

[62] T. Stifter, O. Marti, and B. Bhushan, *Theoretical investigation of the distance dependence of capillary and van der Waals forces in scanning force microscopy*, Physical Review B **62**, 13667 (2000).

[63] G. Binnig, C. F. Quate, and C. Gerber, *Atomic Force Microscope*, Physical Review Letters **56**, 930 (1986).

[64] P. E. West, Introduction to atomic force microscopy: Theory, practice, applications, http://www.paulwestphd.com/chapter7.html.

[65] J. Hu, X.-D. Xiao, and M. Salmeron, *Scanning polarization force microscopy: A technique for imaging liquids and weakly adsorbed layers*, Applied Physics Letters **67**, 476 (1995).

[66] Y. Martin, C. C. Williams, and H. K. Wickramasinghe, *Atomic force microscopeforce mapping and profiling on a sub 100-Å scale*, Journal of Applied Physics **61**, 4723 (1987).

[67] W. Han, S. M. Lindsay, and T. Jing, *A magnetically driven oscillating probe microscope for operation in liquids*, Applied Physics Letters **69**, 4111 (1996).

[68] M. Penedo, I. Fernández-Martínez, J. L. Costa-Krämer, M. Luna, and F. Briones, *Magnetostriction-driven cantilevers for dynamic atomic force microscopy*, Applied Physics Letters **95**, 143505 (2009).

[69] J. Tamayo and R. García, *Deformation, Contact Time, and Phase Contrast in Tapping Mode Scanning Force Microscopy*, Langmuir **12**, 4430 (1996).

[70] B. Gotsmann, C. Seidel, B. Anczykowski, and H. Fuchs, *Conservative and dissipative tip-sample interaction forces probed with dynamic AFM*, Physical Review B **60**, 11051 (1999).

[71] R. García and A. San Paulo, *Attractive and repulsive tip-*

sample interaction regimes in tapping-mode atomic force microscopy, Physical Review B **60**, 4961 (1999).

[72] J. Preiner, J. Tang, V. Pastushenko, and P. Hinterdorfer, *Higher harmonic atomic force microscopy: imaging of biological membranes in liquid*, Physical Review Letters **99**, 046102 (2007).

[73] R. García and R. Pérez, *Dynamic atomic force microscopy methods*, Surface Science Reports **47**, 197 (2002).

[74] T. R. Albrecht, P. Grütter, D. Horne, and D. Rugar, *Frequency modulation detection using high-Q cantilevers for enhanced force microscope sensitivity*, Journal of Applied Physics **69**, 668 (1991).

[75] F. J. Giessibl, *Atomic Resolution of the Silicon (111)-(7x7) Surface by Atomic Force Microscopy*, Science **267**, 68 (1995).

[76] Y. Sugawara, M. Ohta, H. Ueyama, and S. Morita, *Defect Motion on an InP(110) Surface Observed with Noncontact Atomic Force Microscopy*, Science **270**, 1646 (1995).

[77] P. K. Hansma *et al.*, *Tapping mode atomic force microscopy in liquids*, Applied Physics Letters **64**, 1738 (1994).

[78] A. Raman, J. Melcher, and R. Tung, *Cantilever dynamics in atomic force microscopy*, Nano Today **3**, 20 (2008).

[79] E. Palacios-Lidón, C. Munuera, C. Ocal, and J. Colchero, *Contrast inversion in non-contact Dynamic Scanning Force Microscopy: What is high and what is low?*, Ultramicroscopy **110**, 789 (2010).

[80] J. Tamayo and R. García, *Effects of elastic and inelastic interactions on phase contrast images in tapping-mode scanning force microscopy*, Applied Physics Letters **71**, 2394 (1997).

[81] J. P. Cleveland, B. Anczykowski, A. E. Schmid, and V. B. Elings, *Energy dissipation in tapping-mode atomic force microscopy*, Applied Physics Letters **72**, 2613 (1998).

[82] A. Noy, C. H. Sanders, D. V. Vezenov, S. S. Wong, and C. M. Lieber, *Chemically-Sensitive Imaging in Tapping Mode by Chemical Force Microscopy: Relationship between Phase Lag and Adhesion*, Langmuir **14**, 1508 (1998).

[83] G. Bar, R. Brandsch, and M.-H. Whangbo, *Effect of Viscoelastic Properties of Polymers on the Phase Shift in Tapping Mode Atomic Force Microscopy*, Langmuir **14**, 7343 (1998).

[84] A. San Paulo Hernando, *Dinámica de la Microscopía de Fuerzas con modulación de amplitud: descripción teórica e implicaciones experimentales*, PhD thesis, 2002.

[85] N. Kobayashi, Y. J. Li, Y. Naitoh, M. Kageshima, and Y. Sugawara, *High-Sensitivity Force Detection by Phase-Modulation Atomic Force Microscopy*, Japenese Journal of Applied Physics **45**, L793 (2006).

[86] D. Martínez Martín, *Nuevas técnicas basadas en microscopía de fuerza atómica: del vacío a los líquidos*, PhD thesis, 2011.

[87] M. Jaafar, D. Martínez-Martín, M. Cuenca, J. Melcher, A. Raman, and J. Gómez-Herrero, *Drive-amplitude-modulation atomic force microscopy: From vacuum to liquids*, Beilstein Journal of Nanotechnology **3**, 336 (2012).

[88] T. R. Rodríguez and R. García, *Compositional mapping of surfaces in atomic force microscopy by excitation of the second normal mode of the microcantilever*, Applied Physics Letters **84**, 449 (2004).

[89] R. Proksch, *Multifrequency, repulsive-mode amplitude-modulated*

atomic force microscopy, Applied Physics Letters **89**, 113121 (2006).

[90] N. F. Martínez, S. Patil, J. R. Lozano, and R. García, *Enhanced compositional sensitivity in atomic force microscopy by the excitation of the first two flexural modes*, Applied Physics Letters **89**, 153115 (2006).

[91] D. Kiracofe, J. Melcher, and A. Raman, *Gaining insight into the physics of dynamic atomic force microscopy in complex environments using the VEDA simulator*, Review of Scientific Instruments **83**, 013702 (2012).

[92] B. Cappella and G. Dietler, *Force-distance curves by atomic force microscopy*, Surface Science Reports **34**, 1 (1999).

[93] H.-J. Butt, B. Cappella, and M. Kappl, *Force measurements with the atomic force microscope: Technique, interpretation and applications*, Surface Science Reports **59**, 1 (2005).

[94] P. Hinterdorfer and Y. F. Dufrêne, *Detection and localization of single molecular recognition events using atomic force microscopy*, Nature Methods **3**, 347 (2006).

[95] M. C. Fuss, E. Sahagún, M. Köber, F. Briones, M. Luna, and J. J. Sáenz, *Phase contrast in Simultaneous Topography and Recognition imaging*, Ultramicroscopy **109**, 1189 (2009).

[96] K. O. van der Werf, C. A. J. Putman, B. G. de Grooth, and J. Greve, *Adhesion force imaging in air and liquid by adhesion mode atomic force microscopy*, Applied Physics Letters **65**, 1195 (1994).

[97] P. J. de Pablo, J. Colchero, J. Gomez-Herrero, and A. M. Baro, *Jumping mode scanning force microscopy*, Applied Physics Letters **73**, 3300 (1998).

[98] E. Dague *et al.*, *Chemical force microscopy of single live cells*, Nano Letters **7**, 3026 (2007).

[99] Y. Gan, *Atomic and subnanometer resolution in ambient conditions by atomic force microscopy*, Surface Science Reports **64**, 99 (2009).

[100] L. D. Landau and E. M. Lifschitz, *Theory of Elasticity* (Pergamon, Oxford, 1970).

[101] M. J. Higgins *et al.*, *Noninvasive determination of optical lever sensitivity in atomic force microscopy*, Review of Scientific Instruments **77**, 013701 (2006).

[102] P. Attard, T. Pettersson, and M. W. Rutland, *Thermal calibration of photodiode sensitivity for atomic force microscopy*, Review of Scientific Instruments **77**, 116110 (2006).

[103] J. E. Sader, J. W. M. Chon, and P. Mulvaney, *Calibration of rectangular atomic force microscope cantilevers*, Review of Scientific Instruments **70**, 3967 (1999).

[104] L. Bocquet, E. Charlaix, S. Ciliberto, and J. Crassous, *Moisture-induced ageing in granular media and the kinetics of capillary condensation*, Nature **396**, 735 (1998).

[105] I. L. Singer and H. M. Pollock, *Fundamentals of Friction: Macroscopic and Microscopic Processes* (Kluwer, Dordrecht, 1991).

[106] C. M. Mate, *Tribology on the Small Scale: a Bottom Up Approach to Friction, Lubrication, and Wear* (Oxford University Press, Oxford, 2008).

[107] K. Autumn *et al.*, *Adhesive force of a single gecko foot-hair*, Nature **405**, 681 (2000).

[108] K. Autumn *et al.*, *Evidence for van der Waals adhesion in gecko setae*, PNAS **99**, 12252 (2002).

[109] G. Huber *et al.*, *Evidence for capillarity contributions to gecko adhesion from single spatula nanomechanical measurements*, PNAS **102**, 16293 (2005).

[110] T. W. Kim and B. Bhushan, *The adhesion model considering capillarity for gecko attachment system*, Journal of the Royal Society Interface **5**, 319 (2008).

[111] L. F. Boesel, C. Greiner, E. Arzt, and A. del Campo, *Gecko-inspired surfaces: a path to strong and reversible dry adhesives*, Advanced Materials **22**, 2125 (2010).

[112] J. S. Kwaki and T. W. Kim, *A Review of Adhesion and Friction Models for Gecko Feet*, International Journal of Precision Engineering and Manufacturing **11**, 171 (2010).

[113] W. R. Hansen and K. Autumn, *Evidence for self-cleaning in gecko setae*, PNAS **102**, 385 (2005).

[114] D. B. Asay and S. H. Kim, *Molar volume and adsorption isotherm dependence of capillary forces in nanoasperity contacts*, Langmuir **23**, 12174 (2007).

[115] A. L. Weisenhorn, P. K. Hansma, T. R. Albrecht, and C. F. Quate, *Forces in atomic force microscopy in air and water*, Applied Physics Letters **54**, 2651 (1989).

[116] H. Klauk, M. Halik, U. Zschieschang, G. Schmid, W. Radlik, and W. Weber, *High-mobility polymer gate dielectric pentacene thin film transistors*, Journal of Applied Physics **92**, 5259 (2002).

[117] J. Bauer, G. Drescher, and M. Illig, *Surface tension, adhesion*

and wetting of materials for photolithographic process, Journal of Vacuum Science & Technology B **14**, 2485 (1996).

[118] L. Xu, A. Lio, J. Hu, D. F. Ogletree, and M. Salmeron, *Wetting and capillary phenomena of water on mica*, Journal of Physical Chemistry B **102**, 540 (1998).

[119] E. S. Yoon, S. H. Yang, H. G. Han, and H. Kong, *An experimental study on the adhesion at a nano-contact*, Wear **254**, 974 (2003).

[120] A. O. Parry, C. Rascón, N. B. Wilding, and R. Evans, *Condensation in a capped capillary is a continuous critical phenomenon*, Physical Review Letters **98**, 226101 (2007).

[121] E. J. W. Wensink, A. C. Hoffmann, M. E. F. Apol, and H. J. C. Berendsen, *Properties of adsorbed water layers and the effect of adsorbed layers on interparticle forces by liquid bridging*, Langmuir **16**, 7392 (2000).

[122] D. Seveno and J. De Coninck, *Possibility of different time scales in the capillary rise around a fiber*, Langmuir **20**, 737 (2004).

[123] J. Jang, M. Yang, and G. Schatz, *Microscopic origin of the humidity dependence of the adhesion force in atomic force microscopy*, Journal of Chemical Physics **126**, 174705 (2007).

[124] J. Jang, G. C. Schatz, and M. A. Ratner, *Capillary force in atomic force microscopy*, Journal of Chemical Physics **120**, 1157 (2004).

[125] F. Restagno, L. Bocquet, and T. Biben, *Metastability and nucleation in capillary condensation*, Physical Review Letters **84**, 2433 (2000).

[126] R. Evans, *Liquids and Interfaces* (Elsevier, New York, 1989).

[127] K. H. Chung, Y. H. Lee, and D. E. Kim, *Characteristics of fracture*

during the approach process and wear mechanism of a silicon AFM tip, Ultramicroscopy **102**, 161 (2005).

[128] C. Jai, J. P. Aimé, D. Mariolle, R. Boisgard, and F. Bertin, *Wetting an oscillating nanoneedle to image an air–liquid interface at the nanometer scale: dynamical behavior of a nanomeniscus*, Nano Letters **6**, 2554 (2006).

[129] J. Tamayo and R. García, *Relationship between phase shift and energy dissipation in tapping-mode scanning force microscopy*, Applied Physics Letters **73**, 2926 (1998).

[130] P. D. Ashby and C. M. Lieber, *Ultra-sensitive imaging and interfacial analysis of patterned hydrophilic SAM surfaces using energy dissipation chemical force microscopy*, Journal of the American Chemical Society **127**, 6814 (2005).

[131] R. García, R. Magerle, and R. Perez, *Nanoscale compositional mapping with gentle forces*, Nature Materials **6**, 405 (2007).

[132] P. Gleyzes, P. K. Kuo, and A. C. Boccara, *Bistable behavior of a vibrating tip near a solid surface*, Applied Physics Letters **58**, 2989 (1991).

[133] B. Anczykowski, D. Krüger, and H. Fuchs, *Cantilever dynamics in quasinoncontact force microscopy: Spectroscopic aspects*, Physical Review B **53**, 15485 (1996).

[134] U. Dürig, *Interaction sensing in dynamic force microscopy*, New Journal of Physics **2**, 1 (2000).

[135] S. J. T. van Noort, K. O. van der Werf, B. G. de Grooth, N. F. van Hulst, and J. Greve, *Height anomalies in tapping mode atomic force microscopy in air caused by adhesion*, Ultramicroscopy **69**, 117

(1997).

[136] J. Hu, X.-D. Xiao, D. F. Ogletree, and M. Salmeron, *The structure of molecularly thin films of water on mica in humid environments*, Surface Science **344**, 221 (1995).

[137] M. Luna, J. Colchero, and A. M. Baró, *Study of Water Droplets and Films on Graphite by Noncontact Scanning Force Microscopy*, Journal of Physical Chemistry B **103**, 9576 (1999).

[138] A. Gómez Roca, *Preparación de nanopartículas magnéticas uniformes y de alta cristalinidad para biomedicina*, PhD thesis, 2009.

[139] H. G. Bagaria, G. C. Kini, and M. S. Wong, *Electrolyte Solutions Improve Nanoparticle Transfer from Oil to Water*, Journal of Physical Chemistry C **114**, 19901 (2010).

[140] R. Brown, *A brief account of microscopical observations made in the months of June, July and August, 1827, on the particles contained in the pollen of plants; and on the general existence of active molecules in organic and inorganic bodies*, Philosophical Magazine **4**, 161 (1828).

[141] A. Einstein, *Über die von der molekularkinetischen Theorie der Wärme geforderte Bewegung von in ruhenden Flüssigkeiten suspendierten Teilchen*, Annalen der Physik **17**, 549 (1905).

[142] M. Smoluchowski, *Zur kinetischen Theorie der Brownschen Molekularbewegung und der Suspensionen*, Annalen der Physik **21**, 756 (1906).

[143] J. Perrin, *Mouvement brownien et réalité moléculaire*, Annales de Chimie et de Physique **18**, 5 (1909).

[144] T. Pons, H. T. Uyeda, I. L. Medintz, and H. Mattoussi,

Hydrodynamic dimensions, electrophoretic mobility, and stability of hydrophilic quantum dots, Journal of Physical Chemistry B **110**, 20308 (2006).

[145] W. J. Parak, T. Pellegrino, C. M. Micheel, D. Gerion, S. C. Williams, and A. P. Alivisatos, *Conformation of oligonucleotides attached to gold nanocrystals probed by gel electrophoresis*, Nano Letters **3**, 33 (2003).

[146] J. Israelachvili and H. Wennerström, *Role of hydration and water structure in biological and colloidal interactions*, Nature **379**, 219 (1996).

[147] J. H. Seinfeld and S. N. Pandis, *Atmospheric Chemistry and Physics: From Air Pollution to Climate Change*, 2nd ed. (John Wiley and Sons, New Jersey, 2006), Chapter 15.1.1.

[148] H. C. van de Hulst, *Light Scattering by Small Particles* (Dover, New York, 1981).

[149] A. F. Rebolledo, A. B. Fuertes, T. Gonzalez-Carreño, M. Sevilla, T. Valdes-Solis, and P. Tartaj, *Signatures of clustering in superparamagnetic colloidal nanocomposites of an inorganic and hybrid nature*, Small **4**, 254 (2008).

[150] K. Enpuku *et al.*, *Properties of magnetic nanoparticles in the Brownian relaxation range for liquid phase immunoassays*, Journal of Applied Physics **102**, 054901 (2007).

[151] H. Benoit, *Contribution a l'étude de l'effet kerr présenté par les solutions diluées de macromolécules rigides*, Annales de Physique **6**, 561 (1951).

[152] J. García de la Torre, G. del Rio Echenique, and A. Ortega, *Improved*

calculation of rotational diffusion and intrinsic viscosity of bead models for macromolecules and nanoparticles, Journal of Physical Chemistry B **111**, 955 (2007).

[153] J. Badoz, *Mesures photoélectriques de faibles biréfringences et de très petits pouvoirs rotatoires*, Journal De Physique Et Le Radium **17**, A143 (1956).

[154] H. G. Jerrard, *Optical compensators for measurement of elliptical polarization*, Journal of the Optical Society of America **38**, 35 (1948).

[155] J. O. Ellis and J. P. Llewellyn, *Measurement of the AC Kerr effect in conducting liquids*, Journal of Physics E: Scientific Instruments **10**, 1249 (1977).

[156] L. B. Kiss, J. Söderlund, G. A. Niklasson, and C. G. Granqvist, *New approach to the origin of lognormal size distributions of nanoparticles*, Nanotechnology **10**, 25 (1999).

[157] E. Limpert, W. A. Stahel, and M. Abbt, *Log-normal distributions across the sciences: Keys and clues*, Bioscience **51**, 341 (2001).

[158] T. A. Salaoru and J. R. Woodward, *Rapid rise time pulsed magnetic field circuit for pump-probe field effect studies*, Review of Scientific Instruments **78**, 036104 (2007).

[159] C. Röcker, M. Pötzl, F. Zhang, W. J. Parak, and G. U. Nienhaus, *A quantitative fluorescence study of protein monolayer formation on colloidal nanoparticles*, Nature Nanotechnology **4**, 577 (2009).

[160] M. Moros, B. Pelaz, P. López-Larrubia, M. L. García-Martin, V. Grazú, and J. M. de la Fuente, *Engineering biofunctional magnetic nanoparticles for biotechnological applications*, Nanoscale **2**, 1746 (2010).

[161] S. H. Sun *et al.*, *Monodisperse MFe_2O_4 (M = Fe, Co, Mn) nanoparticles*, Journal of the American Chemical Society **126**, 273 (2004).

[162] T. Pellegrino *et al.*, *Hydrophobic nanocrystals coated with an amphiphilic polymer shell: A general route to water soluble nanocrystals*, Nano Letters **4**, 703 (2004).

[163] W. W. Yu, E. Chang, C. M. Sayes, R. Drezek, and V. L. Colvin, *Aqueous dispersion of monodisperse magnetic iron oxide nanocrystals through phase transfer*, Nanotechnology **17**, 4483 (2006).

[164] U. Pyell, *Characterization of nanoparticles by capillary electromigration separation techniques*, Electrophoresis **31**, 814 (2010).

[165] M. Hanauer, S. Pierrat, I. Zins, A. Lotz, and C. Sönnichsen, *Separation of nanoparticles by gel electrophoresis according to size and shape*, Nano Letters **7**, 2881 (2007).

[166] D. Zanchet, C. M. Micheel, W. J. Parak, D. Gerion, S. C. Williams, and A. P. Alivisatos, *Electrophoretic and structural studies of DNA-directed Au nanoparticle groupings*, Journal of Physical Chemistry B **106**, 11758 (2002).

[167] R. A. Sperling, T. Pellegrino, J. K. Li, W. H. Chang, and W. J. Parak, *Electrophoretic separation of nanoparticles with a discrete number of functional groups*, Advanced Functional Materials **16**, 943 (2006).

[168] M. Djabourov, A. H. Clark, D. W. Rowlands, and S. B. Ross-Murphy, *Small-angle x-ray scattering characterization of agarose sols and gels*, Macromolecules **22**, 180 (1989).

[169] R. A. Sperling *et al.*, *Size determination of (Bio)conjugated water–soluble colloidal nanoparticles: A comparison of different techniques*, Journal of Physical Chemistry C **111**, 11552 (2007).

[170] N. Sharon and H. Lis, *Lectins*, 2nd ed. (Springer, 2007).

[171] R. A. Dwek, *Glycobiology: Toward Understanding the Function of Sugars*, Chemical Reviews **96**, 683 (1996).

[172] Y. C. Lee and R. T. Lee, *Carbohydrate-Protein Interactions: Basis of Glycobiology*, Accounts of Chemical Research **28**, 321327 (1995).

[173] Y. Bourne, H. van Tilbeurgh, and C. Cambillau, *Protein-carbohydrate interactions*, Current Opinion in Structural Biology **3**, 681 (1993).

[174] S. I. van Kasteren, S. J. Campbell, S. Serres, D. C. Anthony, N. R. Sibson, and B. G. Davis, *Glyconanoparticles allow pre-symptomatic in vivo imaging of brain disease*, PNAS **106**, 18 (2009).

[175] J. Martínez de la Fuente, *La interacción carbohidrato-carbohidrato: Aplicación de gliconanopartículas metálicas al estudio de la interacción homofílica del antígeno Le^x*, PhD thesis, 2003.

[176] M. Huet, *Factors Affecting the Molecular Structure and the Agglutinating Ability of Concanavalin A and Other Lectins*, European Journal of Biochemistry **59**, 627 (1975).

[177] I. J. Goldstein, C. E. Hollerman, and E. E. Smith, *Protein-Carbohydrate Interaction. II. Inhibition Studies on the Interaction of Concanavalin A with Polysaccharides*, Biochemistry **4**, 876 (1965).

[178] C. F. Brewer, H. Sternlicht, D. M. Marcus, and A. P. Grollmann, *Interactions of Saccharides with Concanavalin A. Mechanism of Binding of α and β–Methyl D–Glucopyranoside to Concanavalin A*

as Determined by ^{13}C Nuclear Magnetic Resonance, Biochemistry **12**, 4448 (1973).

[179] N. M. Young, *Magnesium as a natural substitute for manganese in concanavalin A and other lectins*, FEBS Letters **161**, 247250 (1983).

[180] X. Wang, O. Ramstrom, and M. Yan, *Quantitative Analysis of Multivalent Ligand Presentation on Gold Glyconanoparticles and the Impact on Lectin Binding*, Analytical Chemistry **82**, 9082 (2010).

[181] Y. J. Chuang, X. C. Zhou, Z. W. Pan, and C. Turchi, *A convenient method for synthesis of glyconanoparticles for colorimetric measuring carbohydrate–protein interactions*, Biochemical and Biophysical Research Communications **389**, 22 (2009).

[182] P.-H. Liang, S.-K. Wang, and C.-H. Wong, *Quantitative analysis of carbohydrate-protein interactions using glycan microarrays: Determination of surface and solution dissociation constants*, Journal of the American Chemical Society **129**, 11177 (2007).

[183] E. A. Smith, W. D. Thomas, L. L. Kiessling, and R. M. Corn, *Surface plasmon resonance imaging studies of protein-carbohydrate interactions*, Journal of the American Chemical Society **125**, 6140 (2003).

[184] C. H. Liang, C. C. Wang, Y. C. Lin, C. H. Chen, C. H. Wong, and C. Y. Wu, *Iron Oxide/Gold Core/Shell Nanoparticles for Ultrasensitive Detection of Carbohydrate-Protein Interactions*, Analytical Chemistry **81**, 7750 (2009).

[185] A. G. Barrientos *et al.*, *Modulating glycosidase degradation and lectin recognition of gold glyconanoparticles*, Carbohydrate Research **344**, 1474 (2009).

[186] M. Kanai, K. H. Mortell, and L. L. Kiessling, *Varying the size of multivalent ligands: The dependence of concanavalin a binding on neoglycopolymer length*, Journal of the American Chemical Society **119**, 9931 (1997).

[187] C. W. Cairo, J. E. Gestwicki, M. Kanai, and L. L. Kiessling, *Control of multivalent interactions by binding epitope density*, Journal of the American Chemical Society **124**, 1615 (2002).

[188] J. Bouckaert, F. Poortmans, L. Wyns, and R. Loris, *Sequential structural changes upon zinc and calcium binding to metal-free concanavalin A*, Journal of Biological Chemistry **271**, 16144 (1996).

[189] H. Otsuka, Y. Akiyama, Y. Nagasaki, and K. Kataoka, *Quantitative and reversible lectin-induced association of gold nanoparticles modified with alpha-lactosyl-omega-mercapto-poly(ethylene glycol)*, Journal of the American Chemical Society **123**, 8226 (2001).

[190] S. Watanabe, K. Yoshida, K. Shinkawa, D. Kumagawa, and H. Seguchi, *Thioglucose-stabilized gold nanoparticles as a novel platform for colorimetric bioassay based on nanoparticle aggregation*, Colloids and Surfaces B-Biointerfaces **81**, 570 (2010).

[191] Y. Sato, T. Murakami, K. Yoshioka, and O. Niwa, *12-Mercaptododecyl beta-maltoside-modified gold nanoparticles: specific ligands for concanavalin A having long flexible hydrocarbon chains*, Analytical and Bioanalytical Chemistry **391**, 2527 (2008).

[192] C. L. Schofield, B. Mukhopadhyay, S. M. Hardy, M. B. McDonnell, R. A. Field, and D. A. Russell, *Colorimetric detection of Ricinus communis Agglutinin 120 using optimally presented carbohydrate-stabilised gold nanoparticles*, Analyst **133**, 626 (2008).

[193] C. L. Schofield, A. H. Haines, R. A. Field, and D. A. Russell, *Silver*

and gold glyconanoparticles for colorimetric bioassays, Langmuir **22**, 6707 (2006).

[194] D. C. Hone, A. H. Haines, and D. A. Russell, *Rapid, quantitative colorimetric detection of a lectin using mannose-stabilized gold nanoparticles*, Langmuir **19**, 7141 (2003).

[195] O. A. Loaiza *et al.*, *Nanostructured Disposable Impedimetric Sensors as Tools for Specific Biomolecular Interactions: Sensitive Recognition of Concanavalin A*, Analytical Chemistry **83**, 2987 (2011).

[196] J. Q. Gao, D. J. Liu, and Z. X. Wang, *Microarray-Based Study of Carbohydrate-Protein Binding by Gold Nanoparticle Probes*, Analytical Chemistry **80**, 8822 (2008).

[197] Y.-K. Lyu, K.-R. Lim, B. Y. Lee, K. S. Kim, and W.-Y. Lee, *Microgravimetric lectin biosensor based on signal amplification using carbohydrate-stabilized gold nanoparticles*, Chemical Communications **39**, 4771 (2008).

[198] I.-H. Min *et al.*, *Electrochemical determination of carbohydrate-binding proteins using carbohydrate-stabilized gold nanoparticles and silver enhancement*, Biosensors & Bioelectronics **26**, 1326 (2010).

[199] A. V. Hill, *The possible effects of the aggregation of the molecules of hæmoglobin on its dissociation curves*, Journal of Physiology **40**, iv (1910).

[200] M. Moros, *Síntesis de gliconanopartículas magnéticas para aplicaciones biomédicas*, PhD thesis, completion expected in 2012.

[201] L. Franco-Fraguas, A. Plá, F. Ferreira, H. Massaldi, N. Suárez, and F. Batista-Viera, *Preparative purification of soybean agglutinin by*

affinity chromatography and its immobilization for polysaccharide isolation, Journal of Chromatography B **790**, 365 (2003).

[202] B. B. L. Agrawal and I. J. Goldstein, *Protein-Carbohydrate interaction: VII. Physical and chemical studies on concanavalin A, the hemagglutinin of the jack bean*, Archives of Biochemistry and Biophysics **124**, 218 (1968).

[203] A. Buckley, The hepthesis LaTeX class.

List of Figures

List of Tables

List of Acronyms

AFM Atomic Force Microscopy 1
AM-AFM Amplitude Modulation Atomic Force Microscopy 37
AR attractive regime 39
ConA Concanavalin A 13
DLS Dynamic Light Scattering 138
DNA deoxyribonucleic acid 3
FM-AFM Frequency Modulation Atomic Force Microscopy 37
Gal galactose 99
Glc glucose 99
GNP glyconanoparticle 99
MNP magnetic nanoparticle 2
NP nanoparticle 7
PBS phosphate buffered saline 158
PEG polyethylene glycol 139
PMAO poly(maleic anhydride-alt-1-octadecene) 139
RH relative humidity 60
RR repulsive regime 39
SEM Scanning Electron Microscopy 62
TBE Tris-Borate-EDTA 140
TEM Transmission Electron Microscopy 71
TMB Transient Magnetic Birefringence 1

List of Publications

Publications related to this work

Application of Transient Magnetic Birefringence to Molecular Recognition Studies
by M. Köber, M. Moros, L. Franco Fraguas, V. Grazú, J. M. de la Fuente, M. Luna and F. Briones
in preparation

Transient magnetic birefringence for determining magnetic nanoparticle diameters in dense, highly light scattering media
by M. Köber, M. Moros, V. Grazú, J. M. de la Fuente, M. Luna and F. Briones
in Nanotechnology **23** 155501 (2012)

Nanogeometry Matters: Unexpected Decrease of Capillary Adhesion Forces with Increasing Relative Humidity
by M. Köber, E. Sahagún, P. García-Mochales, F. Briones, M. Luna and J. J. Sáenz
in Small **6** 2725 (2010)

Adhesion hysteresis in dynamic atomic force microscopy
by M. Köber, E. Sahagún, M. Fuss, F. Briones, M. Luna and J. J. Sáenz
in physica status solidi (RRL) **2** 138 (2008)

Further publications

Oxidized Single-Walled Carbon Nanotubes as Anisotropic Probes for Magnetic Resonance Imaging
by A. Cerpa, M. Köber, D. Calle, V. Negri, J. M. Gavira, A. Hernanz, F. Briones, S. Cerdán and P. Ballesteros
submitted

Room-Temperature Reaction of Oxygen with Gold: An In-situ Ambient-Pressure X-ray Photoelectron Spectroscopy Investigation
by P. Jiang, S. Porsgaard, F. Borondics, M. Köber, A. Caballero, H. Bluhm, F. Besenbacher and M. Salmeron
in Journal of the American Chemical Society **132** 2858 (2010)

Phase contrast in Simultaneous Topography and Recognition imaging
by M. C. Fuss, E. Sahagún, M. Köber, F. Briones, M. Luna and J. J. Sáenz
in Ultramicroscopy **109** 1189 (2009)

Comparison of luminescence imaging and illuminated lock-in thermography on silicon solar cells
by M. Kasemann, M. C. Schubert, M. The, M. Köber, M. Hermle and W. Warta
in Applied Physics Letters **89** 224102 (2006)